INAUGURAL–DISSERTATION

zur

Erlangung der Doktorwürde

der

Naturwissentschaftlich–Mathematischen

Gesamtfakultät

der

Ruprecht–Karls–Universität

Heidelberg

vorgelegt von

Dipl.–Phys. Agnès D.F. Metanomski
aus Paris

Tag der mündl. Prüfung: 22. April 1998

Optical study of F, G and K stars
in the ROSAT All-Sky Survey

Gutachter: Herr Prof. Dr. Joachim Krautter

Herr Prof. Dr. Reiner Wehrse

Zusammenfassung

Ich untersuche eine Stichprobe von 107 Südhimmels-Sternen von Spektraltyp A bis K. Diese Sterne sind als die optischen Gegenstücke zu Röntgen-Quellen, die der ROSAT Satellit während seines All-Sky Survey (RASS) entdeckte, identifiziert wurden. Die Untersuchung wird mit Hilfe optischen Beobachtungen, sowohl photometrischer als auch spektroskopischer, durchgeführt. Verschiedene Parameter werden für die untersuchten Objekte bestimmt, wie z.B. Spektraltyp und Leuchtkraftklasse, absolute Helligkeit, Entfernung, Radialgeschwindigkeit, projezierte Rotationsgeschwindigkeit, Effektivtemperatur, Lithium Häufigkeit.

Ich vergleiche die Röntgen-Parameter meiner Stichproben-Sterne mit denen aus einer ähnlichen Stichprobe von Sternen, die vom *Einstein Observatory* während dessen Medium Sensitivity Survey (EMSS) entdeckt wurden. Ich suche auch nach Korrelationen zwischen verschiedenen Parametern, die für meine Stichproben-Sterne bestimmt wurden und vergleiche die Ergebnisse mit denen, die für die EMSS Stichprobe erhalten wurden, sowie mit den Ergebnissne anderer, früherer Studien.

Abstract

I analyze a sample of 107 southern stars of spectral types A to K, which were identified as the optical counterparts of X-ray sources detected by ROSAT during its All-Sky Survey. The study is conducted using optical observations, photometric as well as spectroscopic (high-resolution). Various parameters are determined for the sample objects, mainly spectral types and luminosity classes, absolute magnitudes, distances, radial velocities, projected rotational velocities, effective temperatures, Lithium abundances.

I compare the X-ray parameters of my sample stars with those of a similar sample, detected by the *Einstein Observatory* during its Medium Sensitivity Survey (EMSS). I also look for correlations between the different stellar parameters determined for my sample, and compare those results to those obtained for the EMSS sample, and also to some results obtained from other, earlier studies.

Contents

List of Figures

List of Tables

1 Introduction

1.1 Stellar X-ray emission

From observations of the Sun during solar eclipses, it was known that the atmosphere extends itself well beyond the normally visible solar "surface", into regions that only have a thin, but very hot plasma. Through models and observations the atmosphere was divided into three zones: the photosphere, where most absorption lines are created, the chromosphere and the corona. The chromosphere appears were the temperature inversion occurs, ie. after the point at which the temperature of the atmospheric plasma starts rising again.

The corona has a very low density but high temperatures, of the order 10^6-10^7 K. At such temperatures the plasma emits the most in the higher energy bands. If the plasma can be approximated to a black body, then the maximum of the emission lies in the range around 0.1 keV, that is in the soft X-ray range.

Studies made of the solar corona have shown that its luminosity varies strongly over time. The X-ray luminosity of the Sun has a minimal value of $\sim 10^{25} erg\ s^{-1}$ and a maximum around $10^{27} erg\ s^{-1}$.

As a matter of fact, the Sun shows variations in many different features, the most visible being the variation of the number and position of solar spots. The variations extend over a period of 11 years, which is considered now as the activity cycle of the Sun. The variations of the corona could be linked to this cycle.

The Sun, being so near, is the easiest star to study, especially in the high energy ranges of the X-ray emission. But without comparisons to other, similar stars, it is impossible to determine how far the solar activity is typical for stellar activity, and the models developed for the Sun can be applied to other stars. This requires the study of stellar coronae and activity for as broad a range of spectral types as possible. This is the central goal of my work, for which I have made use of X-ray observations obtained for a relatively large sample of late-type stars.

1.1.1 Pre-Einstein Era

X-ray astronomy is said to have started with a successful rocket flight on June 19th 1962 (see Giaconni et al. 1962). This flight detected the first non-solar X-ray sources. It was followed by a series of rocket and satellites flights, and the launch of the first satellites dedicated to X-ray observations, the UHURU (1970) and HEAO-1 (1977-1979) satellites, in the course of the sixties and seventies. A review on these and all the following X-ray satellites has been given by Bradt et al. (1992).

These experiments allowed the detection and first study of a wide variety of X-ray sources, as well as the study of the diffuse X-ray background. Among the types of sources detected were X-ray binaries, cataclysmic variables, supernova

remnants, quasars, and galaxies. But only very few "normal" stars could be detected. This was mainly due to the lack of sensitivity of the instruments used, and to the energy ranges (2-20 keV) in which the observations were carried out. In the harder X-ray energy range the emission from stellar sources drops strongly, making their detection with low-sensitivity instruments very difficult. Some stars were detected (Capella being the first, observed in 1975), but not enough to allow the conclusion that X-ray emission is a normal phenomenon for stars. The only type of stars that were observed sufficiently to allow their classification as an X-ray emitting class were the RS CVn binaries.

The results obtained during that period of time are summarized by Mewe (1979).

1.1.2 Einstein Era

With the launch of the *Einstein Observatory* on November 3, 1978, stellar X-ray astronomy really started. The *Einstein Observatory* was the first satellite bearing an X-ray telescope together with an imaging device, the Imaging Proportional Counter (IPC). The IPC allowed the imaging of the sky in the X-ray, making the spatial resolution of sources, and the observation of multiple sources with one exposure. The choice of the instrument made the use of a softer X-ray energy range necessary, making the satellite particularly efficient for the detection of stellar X-ray sources.

This is the reason why among the sources detected by the Einstein Satellite during its Medium Sensitivity Survey (EMSS), a, at the time surprisingly, high number of stellar sources were present. About 26% of the total sample of serendipitously discovered sources studied by Stocke et al. (1991) were stellar sources. Various studies of the stellar sources discovered in the EMSS were carried out. A sample of stars (including 129 objects of spectral type A to K) was studied in detail by Fleming (Fleming, 1988, Fleming et al. 1989). Other, more or less specialized, subsets were studied by various groups (for example Golub et al. 1983, Maggio et al. 1987, Pallavicini et al. 1981, Schmitt et al. 1990). A list of specialized studies is given in Linsky (1990).

1.2 Results from the Einstein Observatory

One of the major results obtained by the *Einstein Observatory* was the detection of X-ray emission from nearly all types of stars, as can be recognized from Fig. 1.1. The shaded areas in the Hertzsprung-Russell diagram of Fig. 1.1 show the location of detection of X-ray emission in stars.

The main exceptions, for which no X-ray emission could be detected, are A-stars (B9-A7, to be precise), and giants/supergiants beyond the so-called Coronal Dividing Line, more precisely all giants later than K2 and all supergiants later than G0.

The mechanisms responsible for the X-ray emission have not been positively
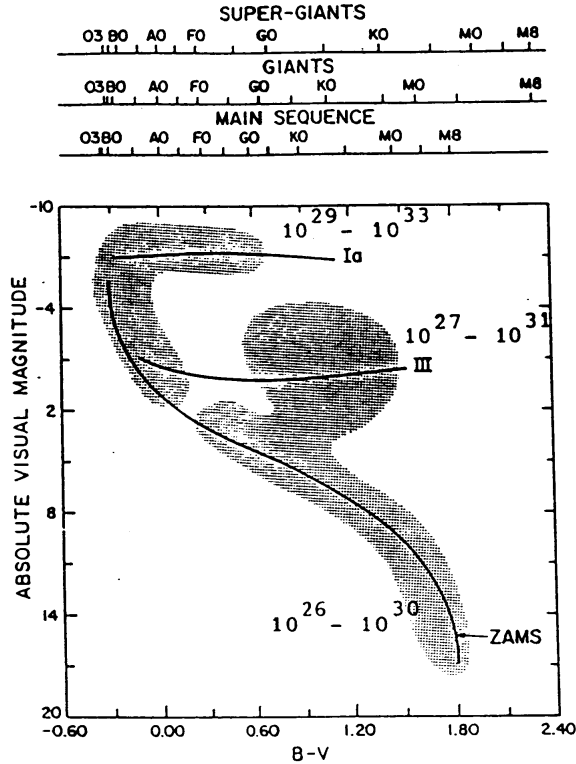
Figure 1.1: Representation of X-ray activity on the Hertzsprung-Russell diagram. The shaded areas indicate the classes of stars detected as X-ray emitters, as well as the X-ray luminosity ranges found for them. Figure taken from Rosner, Golub and Vaiana (1985).

identified. The assumption is that different mechanisms are at the source of the emission for different types of stars.

For early-type stars of spectral types O and B, the X-ray luminosity has been found to correlate with the bolometric luminosity (Pallavicini, 1989). Among all the models proposed to explain the X-ray emission in such stars the most successfull so far has been the model of shocks. This model assumes instabilities in the stellar winds, which lead to the formation of shock fronts in the outflow, which produce the X-ray emission.

Figure 1.2 shows a best fit model to the observed spectrum of ϵ Ori (a B0Iae star). The model reproduces the observations very well, if strong and infrequent shocks are assumed.

Still, the model awaits complete confirmation.

Late-type stars, including main-sequence F to M stars, giants earlier than K2 and supergiants earlier than G0, show a clear correlation between rotation and X-ray luminosity. Noteworthy is the fact that the sample studied by Pallavicini et al. (1981) displays a different correlation to the one found by Fleming for his EMSS sample (Fleming 1988, Fleming et al. 1989). Pallavicini et al. (1981) find

3
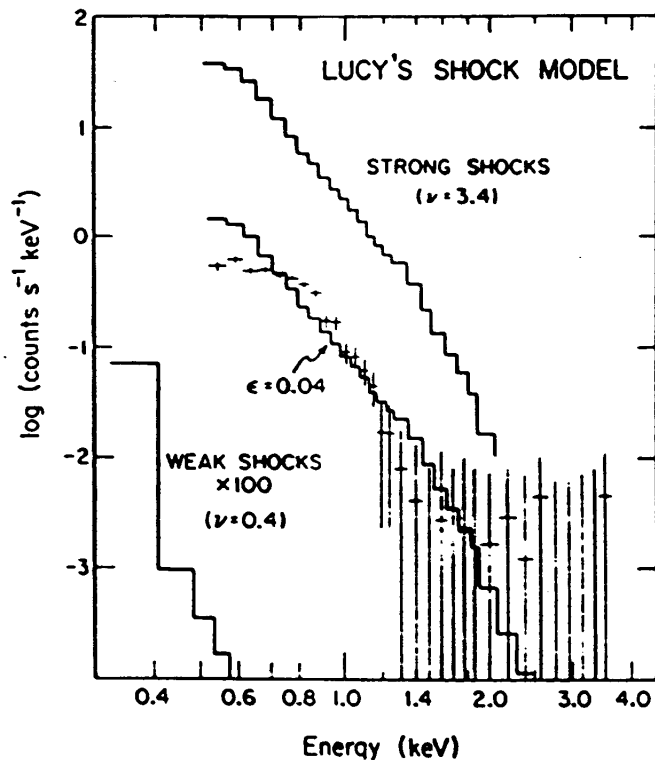
Figure 1.2: Comparison of the Einstein spectrum of ϵ Ori with the shock model of Lucy (1982). The best fit to the observations requires strong, but infrequent shocks (image taken from Cassinelli and Swank 1983).

a correlation of the X-ray luminosity with the square of the projected rotation rate: $L_X \propto (v \sin i)^2$, as can be seen on Fig. 1.3, while Fleming finds a correlation with the projected rotation rate: $L_X \propto v \sin i$. The observed continuum for late-type stars suggests thermal bremsstrahlung emission from hot ($T \sim 7-20 \cdot 10^6 \mathrm{K}$) plasma.

The most commonly used model to explain the X-ray emission as well as the correlation of the X-ray luminosity with rotation is a model based on magnetic heating of the corona, and a magnetic ($\mathbf{B}$) field generated by a dynamo mechanism (Parker 1979). Differential rotation at the base of the convection zone leads to the generation of toroidal $\mathbf{B}$ fields from the primordial poloidal $\mathbf{B}$ field (the so-called Ω effect). These new fields rise through the convection zone due to magnetic buoyancy. The turbulent motions in the convection zone lead to the production of new poloidal $\mathbf{B}$ fields from the toroidal field (the α effect), which in their turn produce new toroidal fields, "feeding" the dynamo. The toroidal field, when reaching the stellar surface, is still embedded in the stellar material, and thus affected by the turbulent surface motions. This causes the plasma enclosed in the field lines to be heated. The corona formed that way is highly inhomogeneous, and

4
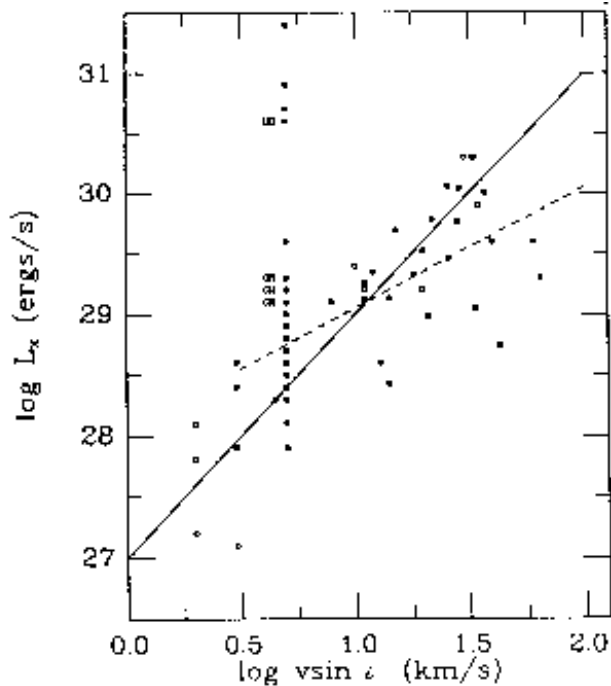
Figure 1.3: The relation between X-ray luminosity and projected rotation rate for the EMSS sample (filled squares) of Fleming (1988) and the sample studied by Pallavicini et al. (1981). The lines show the correlations found by Pallavicini et al. (1981, continuous line) and Fleming (1988, broken line). Image taken from Fleming (1988).

has a strength dependent on the stellar rotation and the depth of the convection zone.

Active binaries of the RS CVn, W UMa or Algol types, which are situated in the same area of the Hertzsprung-Russell Diagram as single late-type stars are believed to have the same basic mechanism for X-ray emission as the single stars, but enhanced through the interaction between the binary system components.

1.3   Dissertation project

Our knowledge of stellar X-ray emission has grown with the study of the stars detected serendipitously by the *Einstein Observatory* and EXOSAT, that allowed the construction of the first X-ray selected star samples.

The amount of knowledge that could be gained to date was limited by the relatively small spatial coverage and the therefore limited number of sources detected (Einstein: about 10% of the sky observed, and 129 stellar sources of spectral types

A to K, see Stocke et al. 1991; EXOSAT: ~ 100 stellar sources, see Giommi et al. 1991).

The ROSAT satellite, with its All-Sky Survey (RASS), has changed this situation. Larger X-ray selected samples can be now constructed. But since the energy range used in the RASS (0.2-2.4 keV) is different to the energy ranges used in the observations of the *Einstein Observatory* (0.1-3.5 keV) and *EXOSAT* (1-50 keV), it is important first to compare the samples obtained, to see if the samples can be considered representative of the stellar X-ray population in the solar neighborhood. This is important in view of the potential of the RASS, which can contain in the order of 15.000 stars, should the percentage of stellar sources be similar to the one obtained in the EMSS. With such a large number of sources, many of the models and assumptions made to explain previous observations can be checked.

I have limited my thesis work to the study of a sample of 107 stars in the southern hemisphere, though a similar sample of 193 stars in the northern hemisphere was also available. Both samples are X-ray selected and composed of all the stars of spectral type A to K located in high-galactic latitude fields. The samples are described in more detail in Chapter 2. The reasons for the limitation to one of the samples is the amount of work involved in getting complete sets of observations for a sample of more than 100 stars. Managing two samples in the course of one thesis work would be quite impossible.

I also concentrated on a certain number of observations, to allow a determination of the most important stellar parameters. With the results from these observations, described in Chapters 3 and 4, the sample can be compared to the EMSS (Fleming 1988, Fleming et al. 1995) and EXOSAT (Tagliaferri et al 1994, Cutispoto et al. 1996) samples. Also, correlations between different parameters can be looked for, in particular the correlation between projected rotation rate $v \sin i$ and X-ray luminosity L_X, to verify the assumptions of current models. The properties of my sample, compared to those of the EMSS and EXOSAT samples, as well as the results of the correlation search, will be discussed in Chapter 5.

2 The ROSAT All-Sky Survey

The major drawback of the Einstein Survey was its spatial limitation. The observations carried out were only pointed ones, and the total area covered only made up $\sim 10\%$ of the sky. Thus the construction of very large samples of stellar X-ray sources was strongly restricted. The total number of available stars in the EMSS is of ~ 215, all spectral types included (Stocke et al. 1991).

This problem was addressed with the construction and launch of a new X-ray satellite, the ROSAT satellite.

2.1 The survey

The ROSAT satellite was successfully launched on June 1st, 1990. It was placed on a circular orbit, with an inclination of 53°, at an altitude of 580 km.

During the following six months, from July 1990 to January 1991 it surveyed the entire sky both in the soft X-ray and in the UV. Some additional observations were carried out in the course of February and August 1991.

The X-ray observations were made in range 0.1 to 2.4 keV. The instrument used was the X-ray Telescope (XRT) and a Position Sensitive Proportional Counter (PSPC) placed in the focal plane of the telescope. The mean sensitivity limit for the survey was at an observed flux of $f_X \sim 2 \cdot 10^{-13} erg\ s^{-1}\ cm^{-2}$. At the ecliptic poles, the sensitivity was higher, with a limiting flux of down to $2 \cdot 10^{-14} erg\ s^{-1}\ cm^{-2}$ and total exposure times of up to 50.000s. At the ecliptic equator, the mean exposure time lay around 400s, and the limiting flux was of $5 \cdot 10^{-13} erg\ s^{-1}\ cm^{-2}$. The survey contains $\sim$60.000 X-ray sources (Voges 1993).

The survey and instruments are described with more detail for example by Trümper at al. (1991). Figure 2.1 shows a sketch of the satellite.

The sources were detected in the images by using a maximum-likelihood algorithm that is described by Cruddace, Hasinger and Schmitt (1988).

2.2 The sample

In order to study the characteristics of X-ray sources detected by ROSAT during its All-Sky Survey, various projects were started. Among these programs were two that consisted of the complete identification of all the X-ray sources within a number of high-galactic latitude fields with optical counterparts.

One of the programs consisted of the study of four fields in the southern hemisphere. This project was granted time at the European Southern Observatory at La Silla as an ESO Key Project (Danziger et al. 1990). The fields comprised a total area of ~ 575 square degrees, and ~ 600 X-ray sources.

The other program, carried out as a collaboration between the Landessternwarte Heidelberg, the INAOE in Mexico and the MPIE in Garching, studied the
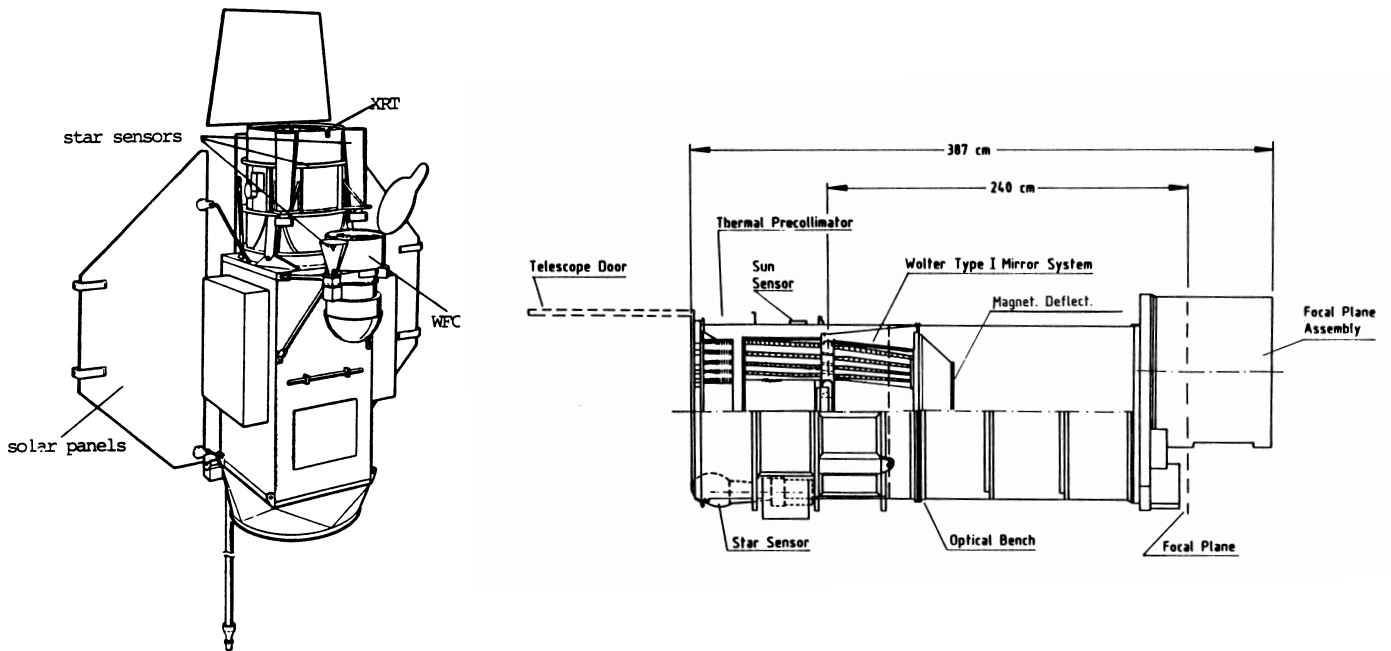
Figure 2.1: Schematic view of the ROSAT satellite and X-ray telescope.

X-ray sources (down to a limiting countrate of 0.03 counts/s, or 0.01 counts/s in one field) of six fields in the northern hemisphere, covering ~ 684 square degrees and some 674 X-ray sources (Appenzeller et al. 1997, Zickgraf et al. 1997).

The position of these ten fields is shown in image 2.2.

In order to identify the X-ray sources with optical counterparts, low-resolution spectra of all sources within the error circle of the ROSAT position ($\sim 30''$) were taken.

For the southern hemisphere sample, the optical candidates were observed with the Boller & Chivens spectrograph at the 1.52 m ESO telescope, and with the EFOSC1 spectrograph at the 3.6 m telescope at the La Silla. The resolutions used were of 7Å and 16Å. In addition to that, intermediate resolution (2Å) spectra of the Hα line were obtained for some of the late-type stars. This was done to confirm whether these objects could be coronal sources, by checking out the presence of enhanced chromospheric activity showed through partial/complete filling-in or emission in the Hα line.

The northern hemisphere sample was studied using mainly the 2.15 m telescope equipped with the *Landessternwarte Faint Object Spectrograph* (LFOSC) at the Guillermo Haro Observatory in Mexico. But some observations were done using the 72 cm Waltz telescope and a Boller & Chivens spectrograph at the Landessternwarte Heidelberg (Ziegler, 1993), and the 2.2 m telescope with EFOSC2

8

at La Silla. The resolution used was of 13Å and 18 Åfor LFOSC, 2 Å for the Boller & Chivens, and 24 Å for EFOSC2. For more details on the identification methods and a list of identifications for the northern sample, see Zickgraf et al. (1997), Appenzeller et al. (1997).
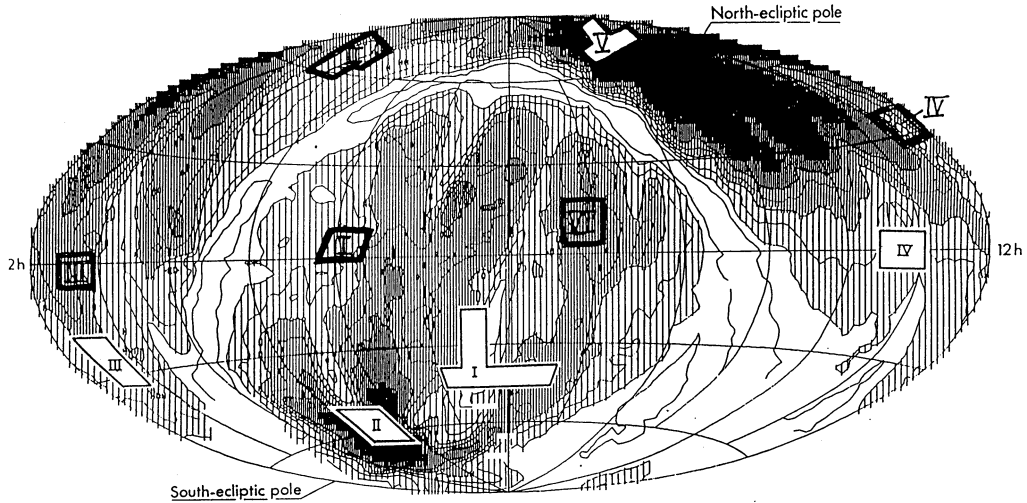
Figure 2.2: Location of the fields studied in the southern and northern identification programs.

The low-resolution spectra obtained were used for a first spectral classification of the stellar sources. In cases of bright stars, the classification from the SIMBAD database was used. The optical identifications are listed in Table B.1, Appendix B for the southern sample and E.1, Appendix E, for the northern one.

Of these two samples, only the southern one could be studied in some detail due to time restrictions. The study of three out of the six northern fields could only be started, and will therefore not be included in most of this work.

3   Observations

To study the properties of the stars in the sample, two types of observations were used: photometric and high-resolution spectroscopic observations. The spectroscopic observations were done mostly in two wavelength ranges, the first around the Li I 6708 Å doublet, and the second around the Ca II H and K lines. For the early F stars, for which very weak Ca II lines could be expected, the observation of the H and K lines were replaced by observations of the He I D_3 5876 Å triplet.

For the southern hemisphere sample, the observations were carried out mostly at the European Southern Observatory, with some stars also observed at the Mount Stromlo Observatory. Some data was gathered, for a limited number of stars in the northern sample, spectroscopic observations at the Observatoire de Haute Provence and Calar Alto Observatory, and photometric observations at the Skinakas and Wise Observatories. For more details on the observing runs, see Tables 3.1 and 3.4.

3.1   Photometry

The photometric observations carried out for the southern sample were all done at the ESO 50 cm telescope, using a photon-counting photomultiplier tube.

Two different tubes were used, a red sensitive dry-ice cooled EMI 9658R and a Peltier cooled Hamamatsu GaAs. The red EMI tube was preferred in the first runs, as it is less sensitive than the Hamamatsu, and allowed therefore the photometry of the brighter stars in the sample, up to V=5.5. For the fainter stars (V≤12) the more sensitive Hamamatsu tube was preferred. The ESO standard $UBV(RI)_C$ filters were used (see Table 3.2).

Four objects had magnitudes above V=5.5 and could therefore not be observed. For these objects data from the literature was gathered. The objects in question are listed in Table 3.3 with the literature references used.

Each measurement consisted normally of three 10s integrations in each filter, except for the U filter, which needed for all but the brightest stars longer integration times (15s-30s). For the faintest stars, longer integration times of 20s-30s were used also in the $BV(RI)_C$ filters. To obtain the transformation coefficients, standard stars from the Cousin's E-regions were observed, and the atmospheric extinction coefficients were obtained by observing two E-region standards of very different spectral types. These standards are listed in the Table D.1 in Appendix D.

The intention was to obtain also light curves for as many sources as possible, to determine the periods of binaries and rotation period of active stars, but the weather condition at La Silla (only 50% photometric weather), the number of sources and the reduced knowledge about binarity available in the early phases

Southern Sample				
Dates	Observatory	Telescope	Detector	Prog. ID
22 Apr. ÷ 02 May 1994	La Silla	50cm ESO	EMI 9658R	53.7-0132
01 Oct. ÷ 10 Oct. 1994	La Silla	50cm ESO	EMI 9658R	54.E-0382
02 Nov. ÷ 12 Nov. 1995	La Silla	50cm ESO	Hamamatsu	56.E-0117
06 May ÷ 16 May 1996	La Silla	50cm ESO	Hamamatsu	57.E-0382
Northern Sample				
Dates	Observatory	Telescope	Detector	Prog. ID
17 Nov. ÷ 27 Nov. 1995	Skinakas	1.3m	CCD camera	
30 Nov. ÷ 11 Dec. 1995	Wise	1m	CCD camera	

Table 3.1: Observing periods, for photometry.

Filter	central λ	$\Delta\lambda$	Transmission
U	3703	485	55.8
B	4424	980	54.8
V	5227	1040	78.4
R	5965	1212	71.1
I	7519	3002	94.0

Table 3.2: The ESO Cousins filters.

of the thesis unfortunately did not allow a successful execution of this part of the observing plan.

The data reduction was done using the PEPSYS package in MIDAS. The error resulting is of the order of 0.01 mag for the stars with V$\leq$10 in all filters, for stars with V$\geq$10 the error is of the order 0.02 mag in the U filter, and 0.01 mag in the other filters, for stars with V$\geq$12, the error is of the order 0.05 mag in the U filter, 0.04 mag in the B filter and 0.03 mag in the remaining filters.

Source	m_v	References
RXJ 0505.6-5728	4.70	Bessel, 1990
RXJ 1132.9-3151	3.54	Eggen, 1977
RXJ 1428.2-0213	4.89	Bessel, 1990
RXJ 1446.3+0153	3.72	Cousins, 1964 Andrillat et al., 1995

Table 3.3: The references used for the brightest sources in the sample.

Southern Sample				
Dates	Observatory	Telescope	Instrument	Prog. ID
22 Apr. ÷ 02 May 1994	La Silla	1.4m CAT	CES	53.E-0132
11 Oct. ÷ 21 Oct. 1994	La Silla	1.4m CAT	CES	54.E-0382
14 July ÷ 17 July 1995	La Silla	3.6m	CASPEC	55.E-0437
13 Mar. ÷ 18 Mar. 1996	Mount Stromlo	74'	Echelle Spectr.	
23 Sep. ÷ 29 Sep. 1996	La Silla	1.4m CAT	CES	00.0-0000
11 Oct. ÷ 16 Oct. 1996	La Silla	1.4m CAT	CES	58.E-0615
18 Feb. ÷ 21 Feb. 1997	La Silla	3.6m	CASPEC	58.E-0615
12 Mar. ÷ 14 Mar. 1997	La Silla	1.4m CAT	CES	58.E-0615
27 June ÷ 29 June 1997	La Silla	3.6m	CASPEC	59.E-0128
Northern Sample				
Dates	Observatory	Telescope	Detector	Prog. ID
06 Dec. ÷ 17 Dec. 1994	OHP	1.53m	AURELIE	
20 Dec. ÷ 27 Dec. 1994	Calar Alto	2.2m	Coude Spectr.	

Table 3.4: Observing periods, for spectroscopy. The observing period between Sept. 23d abd 29th corresponds to reserved time for the 1.4 m CAT and CES.

Some of the stars from the northern sample could be observed during the runs at the Skinakas and Wise Observatories. The observations there were done using a CCD camera and the available sets of $UBV(RI)_C$ filters, although at the Skinakas Observatory, the U filter could not be used, due to damage. To obtain the transformation coefficients as well as the atmospheric extinction coefficients, a set of open clusters with well studied photometry were also observed. The used clusters are listed in Table D.2 in the Appendix D.

These observations have not been fully reduced yet.

3.2   High-resolution spectroscopy

The spectroscopy for the southern sample was carried out at the ESO Osbervatory at two different telescopes: the 1.4 m Coudé Auxiliary Telescope (CAT) with the Coudé Echelle Spectrograph (CES) for the brighter stars ($m_V \leq 11$ in the red, and $m_V \leq 10$ in the blue), and the 3.6 m telescope with the Cassegrain Echelle Spectrograph (CASPEC) for all the other fainter sources.

The resolution used in the spectroscopic observations was dependent on the instrument used. With the CES, a resolving power of 80.000 was used in the first two runs, during which the older CCD # 34 was employed. The new CCD # 38 was used in the last two runs due to its higher sensitivity especially in the blue. Because of a diffusion effect, the resolving power was degraded and only 70.000 could be obtained.

The observations at the 3.6m telescope with CASPEC have a resolving power of 40.000, the maximum obtainable with the spectrograph, for a slit-width of 1". The Echelle Spectrograph at Mount Stromlo Observatory reached a resolution of 50.000. But the spectra obtained there were very faint, the light path of the telescope being inadequate for the spectrograph, strongly reducing its efficiency.

For the observations around the Li I 6708Å line, radial and rotational standards were also observed, to allow the determination of v_{rad} and $v \sin i$ for the sample stars. The standards used are listed in Tables D.3 and D.4, together with the references from which they were obtained. A spectrum of the Sun was taken at twilight to serve as template for the radial and rotational velocity determination.

In addition to the observations around the Ca II H & K lines, B stars were observed. The B star spectra are more adequate for the correction of the instrumental slope than flatfields, so that the corrected spectra can then be flux calibrated (Pasquini et al. 1988). The observations of the He I D$_3$ line were accompanied by the observation of A-type stars, to remove the atmospheric lines present in that spectral range.

The spectra were extracted using the noao.imred.echelle package in IRAF, after being bias subtracted and flatfield corrected. The wavelength calibration was done using ThAr spectra.

A few of the northern stars could also be observed, with the 1.53 m Telescope and AURELIE, at the Observatoire de Haute Provence, and with the 2.2 m and Coudé Spectrograph at the Calar Alto Observatory. All the Lithium spectra obtained were taken at the Observatoire de Haute Provence, with a resolution of 35.000, the Helium line was observed at the Calar Alto Observatory, and Calcium line spectra were obtained from both observatories.

In total 26% of the stars of the northern sample were observed in the Lithium range and 29% in the Ca II/He I range. The observations were reduced using the Long Slit package in MIDAS, after being bias subtracted and flatfield corrected. The wavelength calibration was done using ThAr spectra.

4 Analysis

4.1 Photometry

4.1.1 Spectral classification

From the magnitudes in the the $UBV(RI)_C$ filters obtained from the photometric observations the colour indices $(U - B)$, $(B - V)$, $(V - R)_C$ and $(V - I)_C$ were defined for all the sample stars. For the four bright stars mentioned in Sect. 3.1, the indices obtained from the literature were used. These indices were then used to verify and precise the spectral classification that had been obtained in the course of the identification program either from the low-resolution spectra or from the SIMBAD database.

For this purpose, tables containing mean values of the colour indices for stars of spectral types A to K and luminosity classes V, IV, and III were used. These tables have been compiled by Cutispoto et al. (1996).

For each star, the observed colour indices were compared with the values in the tables. The combination of spectral type and luminosity class that best matched the observed values was then selected for the star's spectral classification. In some cases, no matching set could be found. The star was then assumed to be a binary, and the combination of two stars that matched the observed data best was selected as classification. The single-star/binary assumption was checked using the high-resolution spectra around the Li I 6708 Å line. In most cases, the spectra confirmed the assumption. In a few cases, though, the classification had to be revised after such a check. Those were mostly cases in which the colour indices matched a single star but the spectrum clearly showed two line systems, or the very few cases (2) in which the object revealed itself to be a triple system.

This method is based on the assumption that the stars in the sample are normal, unreddened stars. Considering the detection limits of X-ray observatories, and the relatively low level of the X-ray emission of stars (normally $10^{25} - 10^{32} erg\ s^{-1}$), this assumption is not unreasonable. Most observed stars will be near to the Sun, and therefore have a negligible reddening through the Interstellar Medium (ISM). Nonetheless, it is not a perfect way of classifying the stars, since no tables exist for highly active or Pre-Main-Sequence (PMS) stars, for which the colour indices strongly differ from those for "normal" Main-Sequence and older stars.

4.1.2 The $(U - B)$ colour index

In the course of the classification process, it was noted that, for most stars, the observed $(U - B)$ colour index was systematically bluer than expected for the spectral types best matching the other three colour indices. Figure 4.1 shows this tendency clearly.
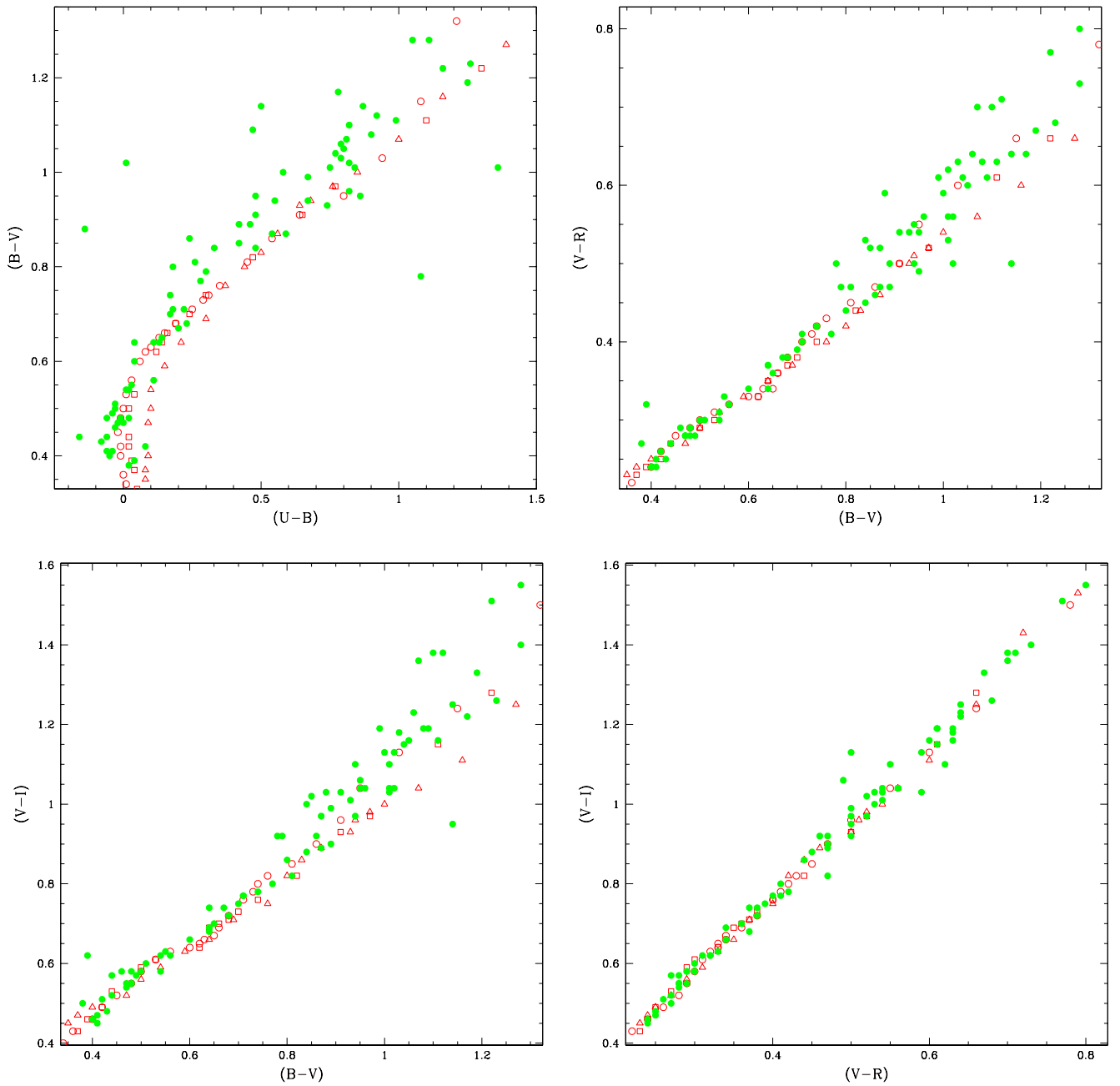
Figure 4.1: Color-Color plots. The filled green circles represent the data observed with the ESO 50 cm for the southern sample. The empty red symbols represent the mean values from the tables of Cutispoto et al. (1996), circles being the data for main-sequence stars, squares for subgiants and triangles for giants.

15

The reason for this trend is not fully understood yet. Some of the problem surely comes from the large errors in the U filter, and also in the B filter for the fainter stars. This at least is indicated by the spread observed in the three first plots of Fig. 4.1, which all include at least the $(B-V)$ colour index. The spread is rather large towards the K stars, where the fainter stars are mostly to be found, and nearly inexistent at the bluer end, where the brighter F stars are located. This is further confirmed by the lack of such a spread in the last, $(V-I)$ vs (V_R) plot, where the observations had a small error bar for all stars.

But the error in the U-filter cannot be the only explanation for the nearly always bluer value of the $(U-B)$ colour, since this is the only index for which a shift as well as a spread is observed. More data is necessary to determine the cause of the problem.

4.1.3 Effective temperature

The effective temperature T_{eff}, necessary among others to get the synthetic spectra for the lithium abundance determination of fast rotators and multiple systems, can be calculated from the $(B-V)$ index. For this I used the work of Alonso et al. (1996), in which the data from a huge sample of stars with known effective temperature and colour indices was used to derive relations between a colour index and T_{eff}.

Among the different equations derived in the work of Alonso et al. (1996), the appropriate one for my sample stars is:

$$
\begin{aligned}
\theta_{\text{eff}} &= 0.541 + 0.533(B-V) + 0.007(B-V)^2 \\
&\quad -0.019(B-V)[\text{Fe/H}] - 0.047[\text{Fe/H}] - 0.011[\text{Fe/H}]^2 \quad (4.1)
\end{aligned}
$$

$$
\sigma(\theta_{\text{eff}}) = 0.023
$$

with θ_{eff} defined as $\theta_{\text{eff}} = 5040/T_{\text{eff}}$.

For the single stars, I used directly the observed $(B-V)$ index. For the binaries and multiple systems, on the other hand, the tables of Cutispoto et al. (1996) were used to get an estimate of the $(B-V)$ colour of each component, and this index was then used to get the effective temperature.

For the metallicity, I assumed solar metallicity for all the stars. This is a reasonable assumption, since the stars are near to the Sun. It turned out to be correct, in first approximation, for most of the objects. A few, though, displayed a metallicity that was clearly not solar. For these stars, the metallicity will have to be determined using spectroscopic observations in appropriate wavelength ranges.

The error in the $(B-V)$ index is, for the single stars, of the order of 0.02 mag to 0.05 mag. For the binaries, with a possible error of one spectral type for each component, the error lies in the range of 0.02 mag to 0.10 mag. This, together

with the error of the equation itself, leads to an error in the effective temperature of up to 10%.

The results are listed in Table B.1, in Appendix B.

4.1.4 Absolute magnitude, distance and X-ray luminosity

The $(B - V)$ index was also used to get the absolute magnitude and the distance from the Sun of the sample objects. For this, as for the effective temperature, the $(B - V)$ colour from the colour tables of Cutispoto et al. (1996) was taken for the binaries and multiple systems, and the observed $(B - V)$ index was used for the single stars. The absolute magnitude was obtained from the $(B-V)$ vs. M_V tables in Gliese (1982) for the later main-sequence stars $((B - V) \geq 0.5)$. For the earlier stars, as well as the giants and subgiants, the M_V values listed in the tables of Cutispoto et al. (1996) were taken.

The error in $(B - V)$, given in the previous section, leads to an error in the absolute magnitude of 0.1 to 0.5 mag for the single stars, and 0.2 to 0.7 mag for the binaries. The corresponding error in the distance is of 5% to 23% for the single stars, and up to 30% for the binaries.

To calculate the observed X-ray flux f_X from the ROSAT countrates, a conversion factor is needed. In most cases, a constant conversion factor is used. But there is an alternative conversion factor for coronal sources, that is a function of the first hardness ratio. This conversion factor was determined by Fleming et al. (1995) and is given by the following equation:

$$CF = (8.31 + (5.30 \cdot HR1)) \cdot 10^{-12} erg \ cm^{-2} \ count^{-1} \qquad (4.2)$$

with the hardness ratio HR1, defined as:

$$\mathrm{HR1} = \frac{CR[ch52 - 201] - CR[ch11 - 41]}{CR[ch11 - 240]} \qquad (4.3)$$

$CR[chA - B]$ is the countrate in the channels "A" to "B" of the PSPC.

Since most of the sample stars are within a circle of 200pc radius, extinction could be considered negligible. The remaining stars are still reasonably near to the Sun for the extinction to be neglected too. This allowed the use of this conversion factor, which takes the slope of the X-ray continuum at least partly into account, to determine the X-ray flux.

The error in the observed flux depends thus both on the error for the countrate and the one for the hardness ratio. Since the total number of counts is small in most cases, these two errors are quite large, adding up to a large error in the flux and in the X-ray luminosity derived from it. The error for the X-ray luminosity is of up to a factor 2.

The X-ray data obtained from the ROSAT observations is listed in Table A.1 in Appendix A, the data obtained from the photometric observations, as well as

Name	Hipparcos data			Data from spectr. class.			Revised Spectral
	π (m")	Dist.	M_V	Spectral type	Dist.	M_V	classif.
2331.4−4209	10.16	98.4	3.28	F9V+G1V	77	3.83	F8/9V+F9V+G1V
2356.2−3903	45.28	22.0	6.51	K3V	21	6.60	
0005.9−4145	24.85	40.0	4.49	G1V	37	4.70	
0038.6−2335	16.01	62.5	3.12	F3/4V	58	3.30	
0053.0−3021	71.01	14.0	6.50	K2/3V	14	6.50	
0055.5−3731	12.22	81.8	4.10	G6V	46	5.35	G6V/IV
0105.4−4016	18.20	54.9	3.47	F3V	62	3.20	
0121.5−4058	11.16	89.6	3.82	F6V	90	3.80	
0135.8−3956	26.54	37.7	3.53	F4V	40	3.40	
0141.4−3808	23.87	41.9	3.07	F3V	39	3.20	
0440.3−5856	32.30	31.0	4.08	G5V	19	5.17	G5V/IV
0454.9−5832	32.38	30.9	3.66	F5V	32	3.60	
0505.5−5728	85.83	11.6	4.38	F7/8V	13	4.15	
0507.6−5459	15.05	66.4	3.23	F5/6V	50	3.80	F5/6V/IV
0527.6−6024	51.10	19.6	5.55	G9V	18	5.60	
0534.4−6006	12.48	80.1	3.88	F7V	76	4.00	
0535.0−6110	9.37	106.7	1.19	G8/9IV	44	3.10	G4/5III
0541.1−6151	4.90	204.1	3.07	F3/4V	192	3.20	
0545.3−5543	11.21	89.2	3.47	F5V+G6V	92	3.40	
0549.7−5950	7.07	141.4	3.11	F7/8V(3x)	148	2.91	
1121.5−3131	16.82	59.4	3.87	F7/8V	54	4.10	
1121.8−2411	20.82	48.0	4.71	G3V	43	4.93	
1122.0−2446	21.43	46.7	5.59	K4/5V+K7V+..	28	6.74	PMS system
1123.3−2342	5.85	170.9	1.00	G8III	187	0.80	
1132.9−3151	25.23	39.6	0.55	G8III	35	0.80	
1354.2−0157	14.03	71.3	4.05	F8V	64	4.30	
1354.9−0222	8.40	119.0	3.51	F9V+G5V	97	3.97	
1358.4−0139	7.94	125.9	4.11	G0V+G5V	123	4.16	
1401.9+0025	15.60	64.1	4.26	F8V	63	4.30	
1404.0−0021	4.31	232.0	1.67	F9V+G5V	79	3.97	F8 IV+G3IV+G3IV
1411.5+0121	21.78	45.9	3.10	F6V	33	3.80	
1413.7−0050	17.94	55.7	2.17	F6V	50	2.41	
1428.2−0213	24.15	41.4	1.73	G6IV+K5V	22	3.08	G2 III/IV+K0:V
1446.3+0153	25.35	39.4	0.74	A0V	41	0.83	
1451.9+0201	25.68	38.9	5.39	G5/6V	41	5.30	

Table 4.1: The sources of the southern sample for which Hipparcos data was found.

X-ray flux, distance and X-ray luminosity are listed in the Table B.1, in Appendix B.

4.1.5   Hipparcos data

For some of the stars in the southern sample, Hipparcos data was available, most particularly the trigonometric parallaxes determined by Hipparcos, which allowed a determination of the distance independent of the photometric "parallaxe".

The objects, 35 in total, are listed in Table 4.1. For most the distances derived from the Hipparcos parallax fell well within the error of the distances determined using the spectral classification. But for a few stars, this was not the case. For these objects, the spectral classification was revised. The results of this new classification are summarised in Table 4.1.

4.2   Spectroscopy

4.2.1   Radial and rotational velocity

The high-resolution spectra taken around the lithium I 6708 Å line could be used to determine the radial velocities and projected rotational velocities for my stars. For this, the cross-correlation method, described by Tonry & Davis (1979),

$$f(\lambda) * g(\lambda) = \int_{-\infty}^{+\infty} f(\alpha)g(\alpha - \lambda)d\alpha \qquad (4.4)$$

was chosen. $f(\lambda)$ and $g(\lambda)$ represent two here mathematical functions of a variable λ.

For this a template star with low rotation was observed, usually the Sun. The shift of the peak resulting from the cross-correlation of a star with the template represents the shift in λ and the width of the peak the relative broadening between the two sets of lines.

To allow the translation of the shifts and widths of the cross-correlation peaks to radial and rotational velocities, a set of standards for both parameters was observed during each run as well. The standards used are listed in Tables D.3 and D.4 in Appendix D.

To derive the radial velocities, the radial velocity standards were first cross-correlated with the solar template, and the shift of the peak registered. The radial velocities of the standards were corrected to include the Earth movement, and the resulting line fitted. Then the actual sample stars were cross-correlated with the template, to get the shift, and their radial velocities, uncorrected for the Earth motion, calculated using the fit obtained for the standards. The heliocentric radial velocities were then determined through the substraction of the corresponding barycentrique velocity of the Earth.

For the rotational velocities, the method was similar. First the rotation standards were cross-correlated to the solar template. The width of the peak was
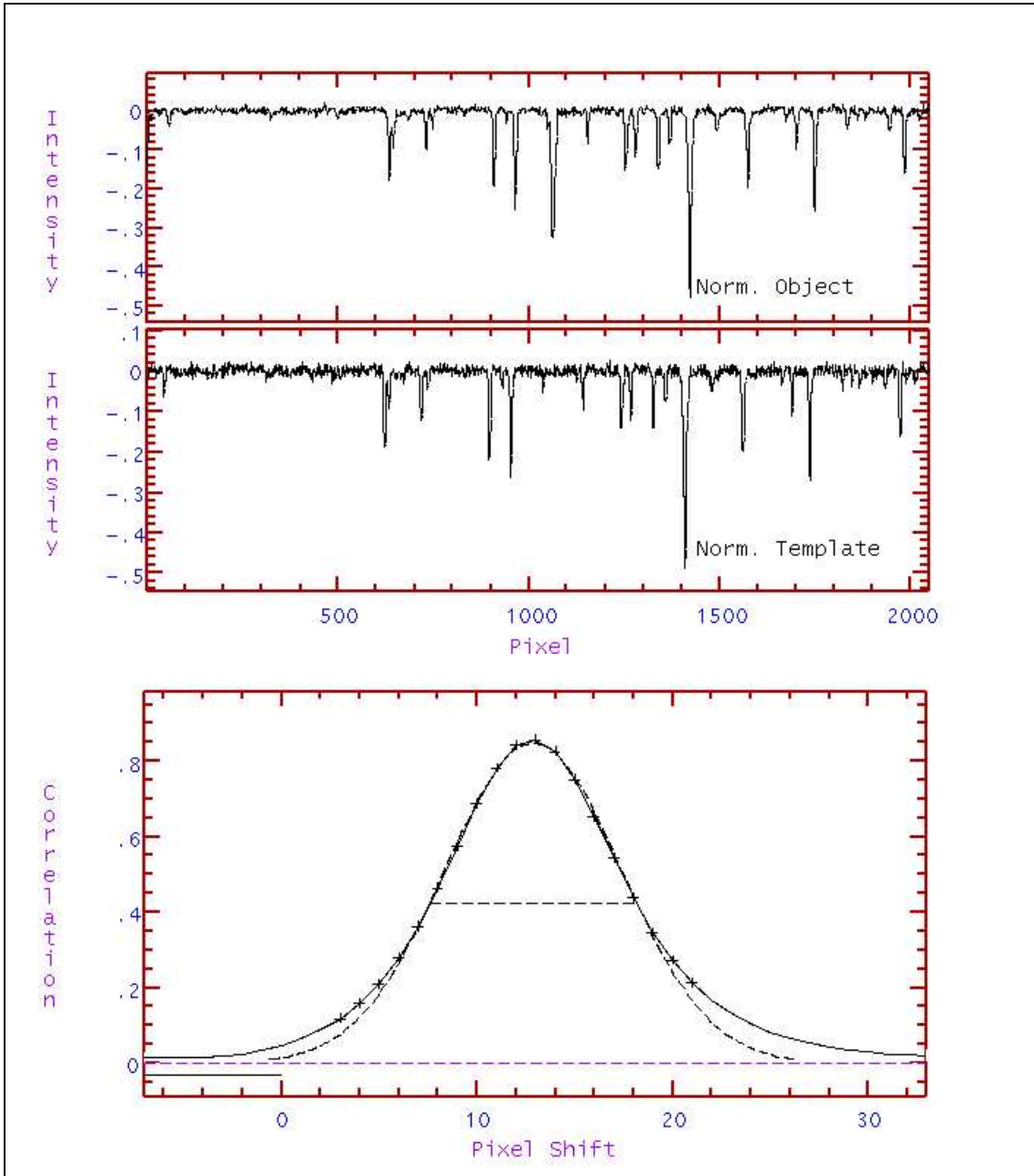
Figure 4.2: Spectrum, solar template and cross-correlation function with fit, for a slow rotating single star, RXJ 1121.8-2411, $v \sin i = 5$ km/s. .

21
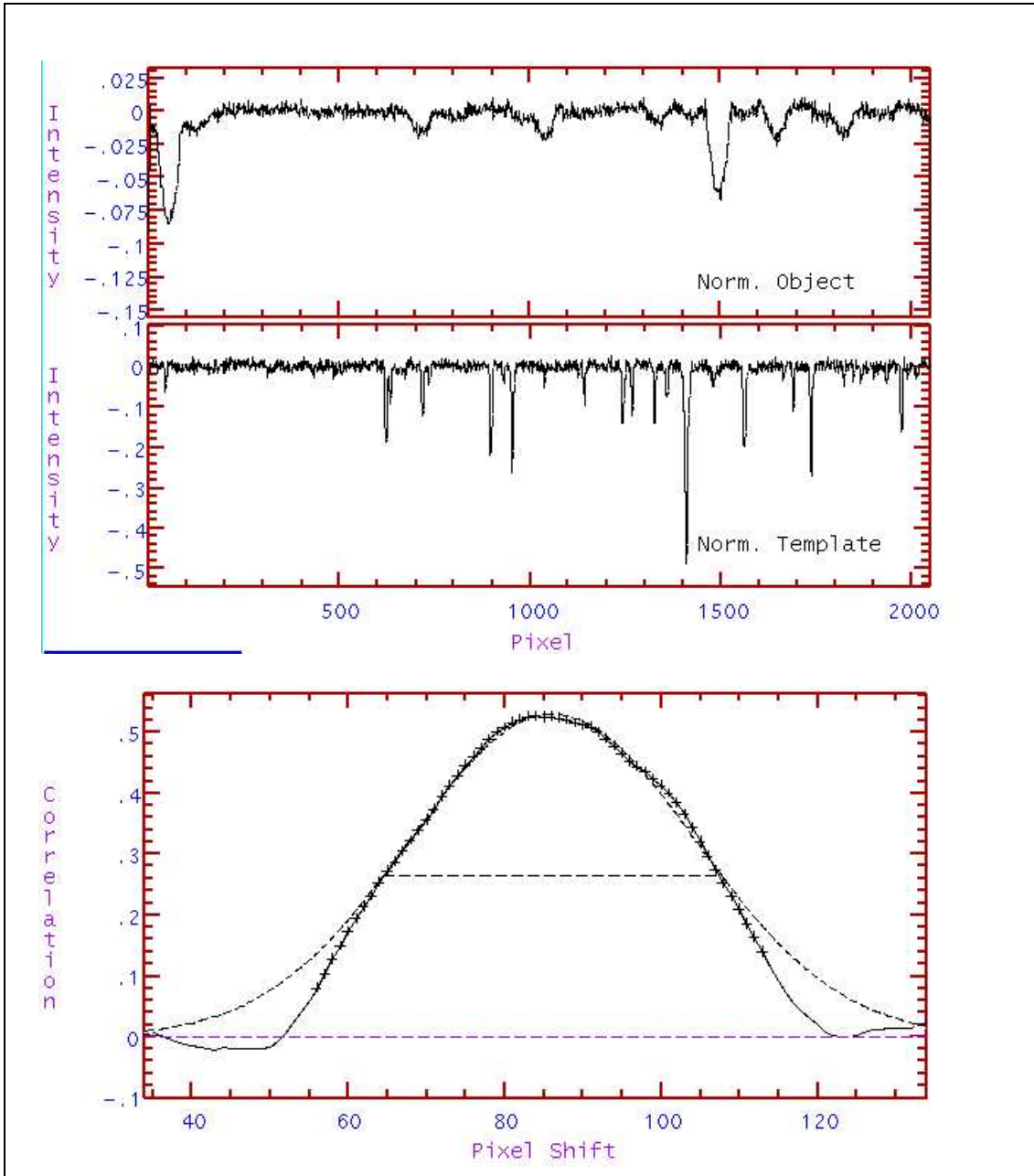
Figure 4.3: Spectrum, solar template and cross-correlation function with fit, for a single fast rotator, RXJ 0135.8-3956, $v \sin i = 33$ km/s. .
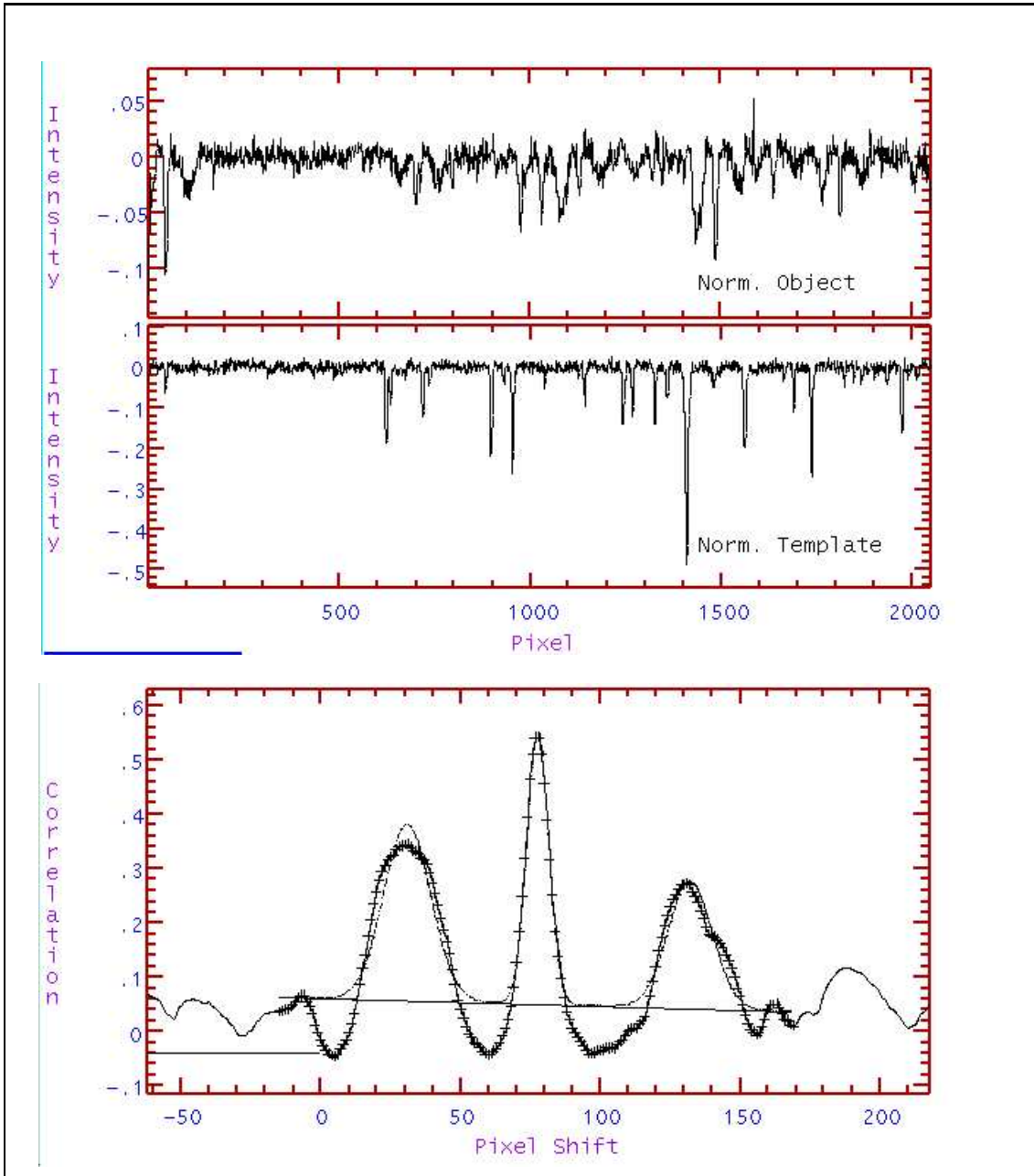
Figure 4.4: Spectrum, solar template and cross-correlation function with fit, for one of the triple systems in the sample, RXJ 2331.4-4209.
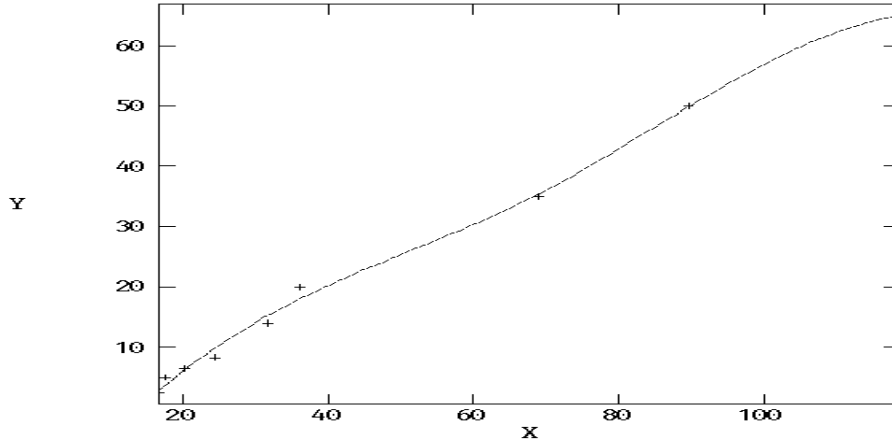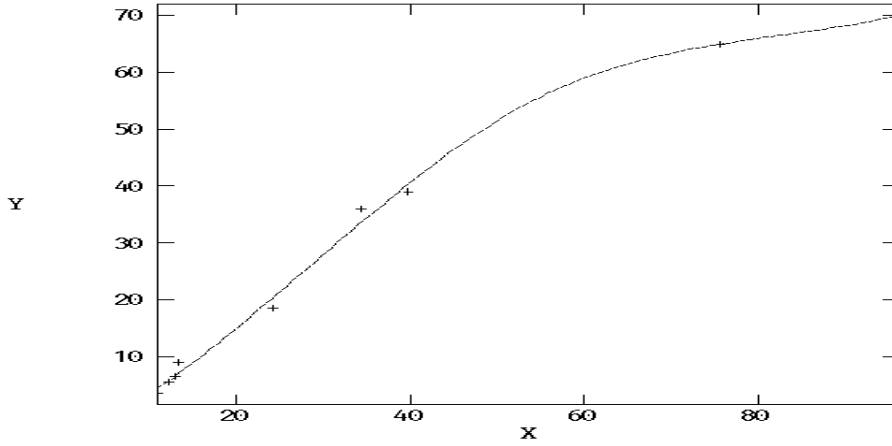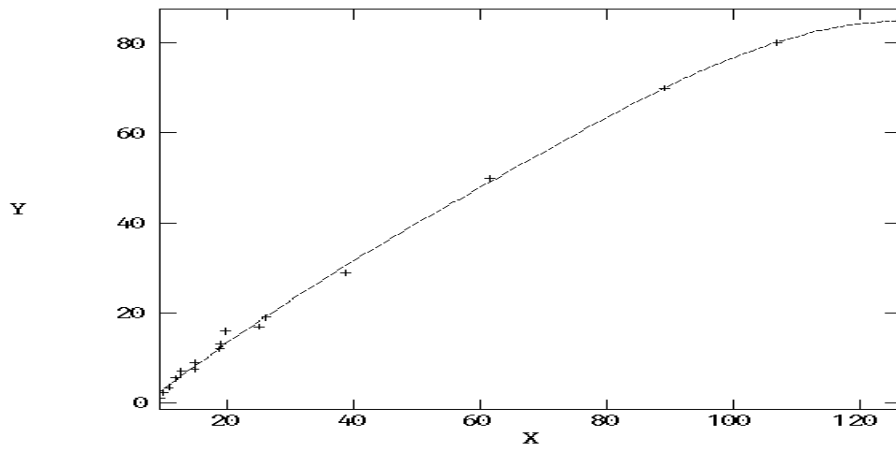
Figure 4.5: The fits obtained from the rotational velocity standards, for the determination of the projected rotational velocity of the sample stars. Top picture: the fit for the observations at the 1.4 m CAT, with the CES and CCD #34. Middle plot: the fit for the observations at the 1.4 m CAT with the CES and CCD #38. Last plot: the fit for the observations at the 3.6 m telescope with CASPEC. The width of the correlation peak (in pixels) is represented on the X axis, the vsini values in the Y axis.

determined, and the resulting $v \sin i$ vs width points were fitted with a polynomial. The cross-correlation peak width for the sample stars was then obtained, and the rotational velocity calculated using the fitted polynomial.

The cross-correlation was done using the **fxcor** routine in IRAF, the fitting with the **curfit** program. Some examples of cross-correlation peaks and gaussian curves fitted to the peaks to obtain the peak shift and width, are shown in Figures 4.2 to 4.4. The fits for the rotational velocity are shown in Fig. 4.5.

The uncertainty for $v \sin i$ depends to a large extent on the the fit. For the spectra taken with the CES, the resolution limit is of 3.5 km/s, for the CASPEC spectra the resolution limit is 7.5 km/s. I assume an error of $\sim$ 2 km/s for the fits for the low velocity end. For the higher velocities ($v/sini/ge50$), the determination of the width of the peak was more difficult, and so the error is larger, of up to 5 km/s.

For fast rotating binaries for which the lines overlap strongly, the error in $v \sin i$ is larger, due to the fact that an exact measurement of the width of the correlation peaks was not possible. The error here can be as large as 5 km/s.

4.2.2 Lithium abundance

The high-resolution spectra were also used to determine the lithium abundance of the sample stars. The lithium dublett at 6708 Å is mostly used for this, and that was the primary motivation for the choice of the wavelength range for the observations.

For the slow-rotating single stars, for which the lithium line could be easily identified and measured, the abundance was determined directly using the equivalent width (EW) of the line. The major problem for this method is the blend of the lithium line with the neighbouring Fe I 6707.44 Å line. For the contribution to the total equivalent width of this iron line, the relation given by Soderblom et al. (1993)

$$W_\lambda(6707.44) = 20(B - V) - 3 \text{ mÅ} \qquad (4.5)$$

was used. The EW obtained for the lithium line, after removal of the contribution of the iron line, was then transformed into an abundance using the curves of growth listed in Soderblom et al. (1993).

For the single stars with high rotational rate and for the binaries, the lithium abundance was determined using synthetic spectra. The synthetic spectra were calculated using the program SYNTH (Piskunov 1992) and model atmospheres from Kurucz (1993). To avoid the problems coming from errors in the excitation potential and log(gf) factor for the lines in the wavelength range considered, I used an atomic line list provided by Randich (1997). I first checked out the result by calculating a solar spectrum and comparing it to the solar spectra I had observed. To verify the validity of the result obtained with the synthetic spectra, a few low-rotating single stars were also fitted. The results from the EW method

and of the synthetic fit were identical, within an error of 0.01 dex. Fig. 4.6 shows some examples of fitted spectra.

The synthetic spectra were wavelength-shifted, to fit the radial velocity shift of the observed spectra, and broadened to the rotational velocity of the corresponding stars, then superposed on the observations. For many of the binaries, only approximate values for the lithium abundance could be determined. This was due to the noise present in the spectrum.

The lithium abundances obtained are listed in Table C.1 in Appendix C. Errors lie in the range of 0.01 dex for the slow rotating single stars to 0.05 dex for the binaries with strong blends.
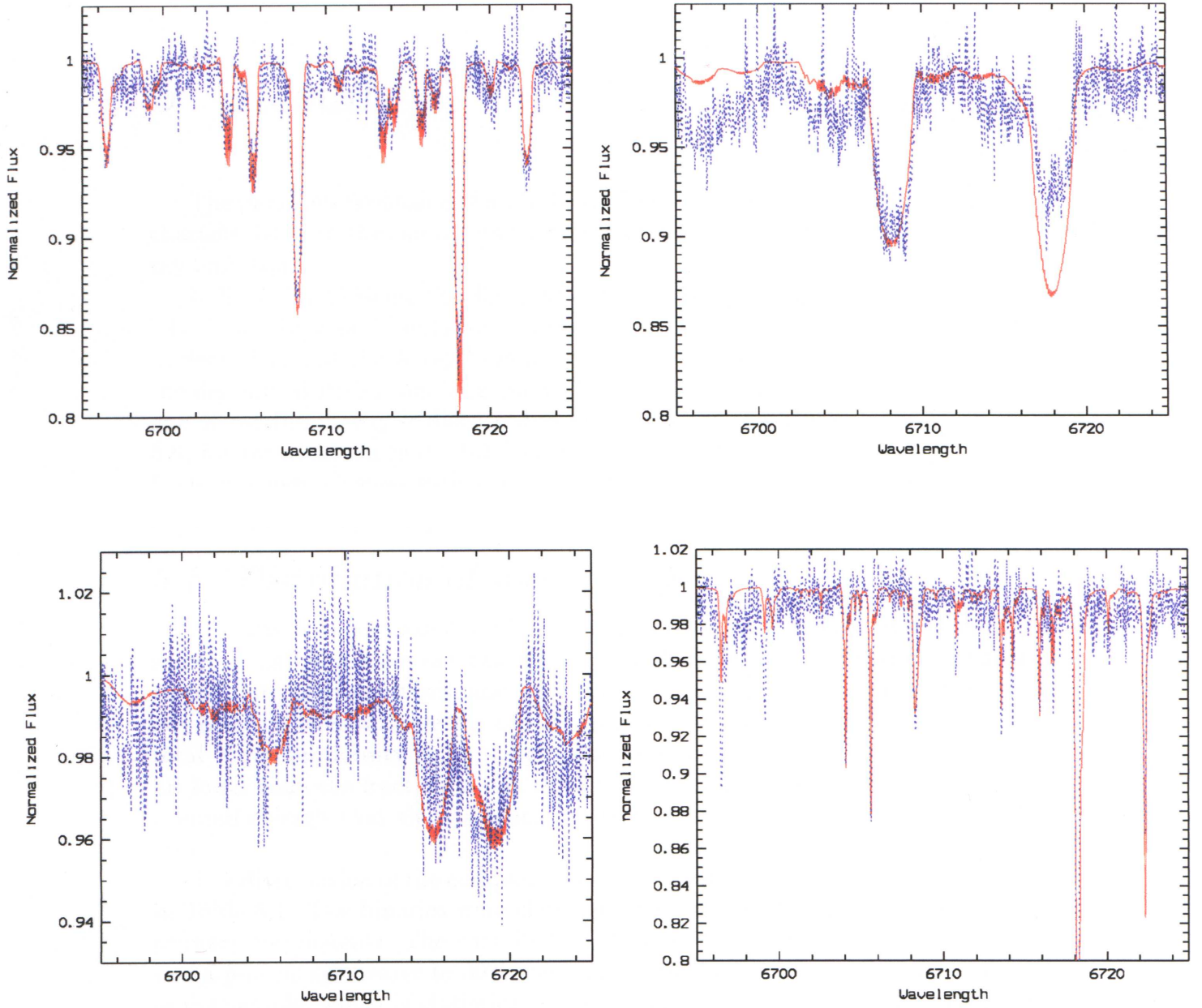
Figure 4.6: Some examples for the synthetic spectra used to determine lithium abundance in rapidly rotating stars and binaries/multiple systems. The stars shown are, from left to right and top to bottom: RXJ 0547.3-5450, RXJ 0505.6-5755, RXJ 1358.4-0139 and RXJ 2331.4-4209. RXJ 0505.6-5755 seems to have a non-solar metallicity.

5 Results

The parameters obtained for all the studied stars can now be used to determine characteristics of the sample and correlations between stellar parameters and X-ray emission.

In Sect. 5.1 I discuss the distribution of the stars among spectral type classes. The X-ray to visual luminosity ratios as function of spectral types are studied in Sect. 5.2, and the X-ray luminosity functions in Sect. 5.3. Sect. 5.4 handles the distance distribution. The search for correlations between stellar parameters and X-ray luminosity is discussed in Sects. 5.5, for the lithium abundance, and 5.6, for rotation. In Sect. 5.5 I also compare the lithium abundances to those from two open clusters with known age (the Hyades and Pleiades), to get a first estimate for the age or evolutionary status of my sample stars.

5.1 Distribution of spectral types

My sample is composed of 81 single stars (76%) and 26 binaries and multiple systems (24%). I have not taken into account which of the binaries are short-period, interactive systems, and which are wide systems at this stage, since it is not possible to determine the contribution of the individual components to the total X-ray luminosity in the long-period systems. The fraction of binaries is a bit lower than the fraction of one third of the sample expected. Still, the sample is small enough that the statistical errors can account for a large part for this also.

The distribution of the complete sample between spectral type groups is shown in Table 5.1. The binaries were classified according to the spectral type of their primary components. The contribution of the G stars seems a bit low, expected was a percentage nearer to 30%, comparable to the fraction of F stars. The size of the sample, which is statistically still rather small, is probably responsible for this effect, as is confirmed by the statistical errors.

Spectral type	my sample		EMSS sample		EXOSAT sample	
A stars	1±1	1±1%	5±2	3±1%	2±1	7±3%
F stars	34±6	32±6%	51±7	30±4%	5±2	17±7%
G stars	24±5	22±5%	45±7	27±4%	14±4	48±14%
K stars	48±7	45±6%	68±8	40±5%	8±3	28±10%

Table 5.1: Distribution of the X-ray sources among the spectral types studied, for my sample, the EMSS sample (Stocke et al. 1991) and the EXOSAT sample (Cutispoto et al. 1996)

Table 5.1 also lists the distributions for two other samples, the *Einstein Observatory* Medium Sensitivity Survey (EMSS) sample (Stocke et al. 1991) and the EXOSAT sample (Cutispoto et al. 1996).

My sample and the EMSS sample show a very similar distribution between spectral types. Since the samples are of similar size, and both X-ray selected, this result was expected. Clearly, this seems to indicate that both samples are composed of stars from similar populations. When taking into account statistical errors, the small differences become completely negligible.

The EXOSAT sample, on the other hand, differs from both my sample and the EMSS one. Here the greatest contribution to the sample comes from the G stars, the K stars being a poor second. But since the sample is a very small one, being composed only of 29 stars, it is doubtful whether this is more than a selection effect. The statistical errors are large enough that, when considered, the distribution of the EXOSAT sample can be neared to that of the other two. To confirm the possibility of the EXOSAT distribution being similar, down to statistical errors, to mine, I applied a Wilcoxon test (Zeidler, 1996) to both distributions.

Given two binned distributions X and Y, with respectively n_1 and n_2 bins. x_i is the number of events in bin i of the first distribution, y_j the number of events in bin j of the second distribution.

The Wilcoxon test consists of verifying for every pair (x_i, y_j) whether $y_j < x_i$. Every positive result of this verification is called an inversion. U is defined as the total number of inversions present, U_α is a parameter dependent on the error probability α chosen.

Two distributions are said to have a significant difference, with an error probability α, if the following condition is valid:

$$\left| U - \frac{n_1 n_2}{2} \right| > U_\alpha \tag{5.1}$$

The result for the distributions in spectral type bins for my sample and the EXOSAT sample, $|U - n_1 n_2/2| = 4 < U_\alpha = 8$ for $\alpha = 0.05$ clearly indicates that the distributions can be considered similar. The differences noted must come from statistical errors.

5.2   X-ray luminosity as a function of spectral type

From the X-ray luminosity and the visual magnitude, the ratio of the X-ray luminosity to the visual luminosity for each sample star can be obtained. The result is shown in Fig. 5.1. All the sources, single stars as well as multiple systems, are considered for this.

Also included in Fig. 5.1 are saturation levels found or calculated from previous studies. These saturation levels correspond, according to current models, to the level of activity for which the whole surface of a star is covered with active
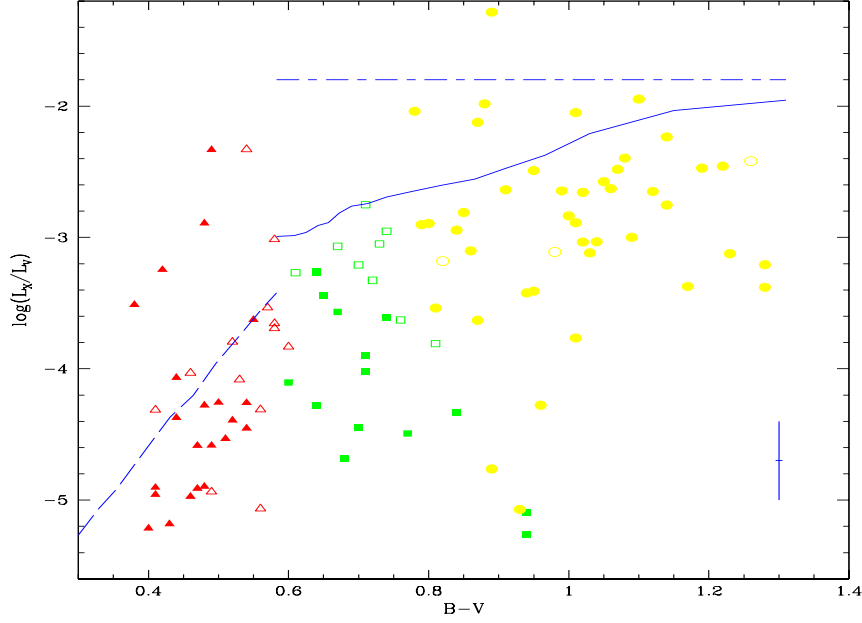
Figure 5.1: $\log(L_X/L_V)$ vs. the $(B-V)$ color index for the studied RASS sample. The red triangles represent the F stars, blue squares the G stars and green circles the K stars. Filled symbols stand for single stars, empty ones for the binaries and multiple systems. The continuous line represents the saturation level of $F_X \sim 7 \cdot 10^7 erg\ s^{-1}\ cm^{-2}$ detected by Fleming in his sample (Fleming, 1988). The dashed line is the upper limit for L_X as calculated by Vilhu and Walter (1987). The dash-dot line is a constant $\log(L_X/L_V)$ of -1.8
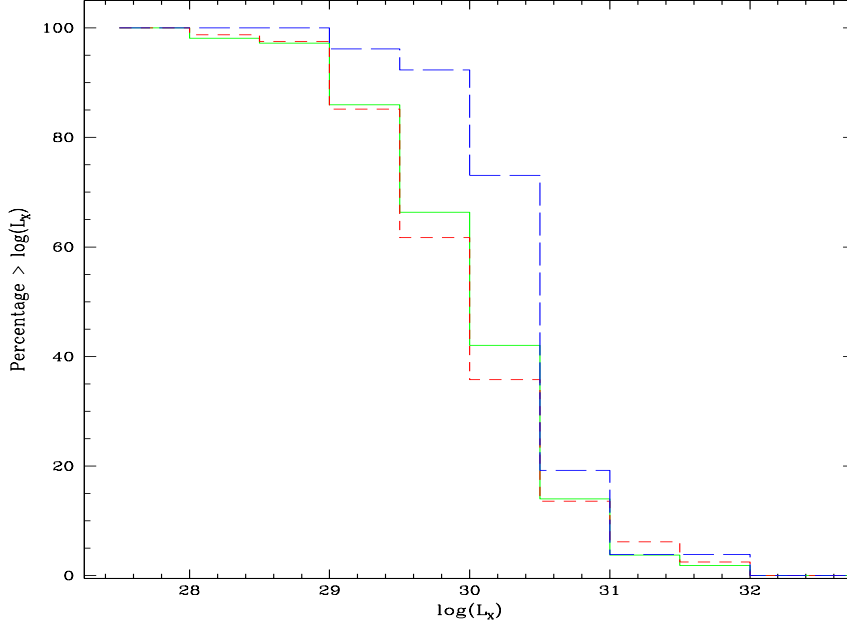
Figure 5.2: Luminosity distribution for the studied sample. Continous green line: the complete sample; red short-dashed line: the single stars; blue long-dashed line: the binaries and multiple systems.
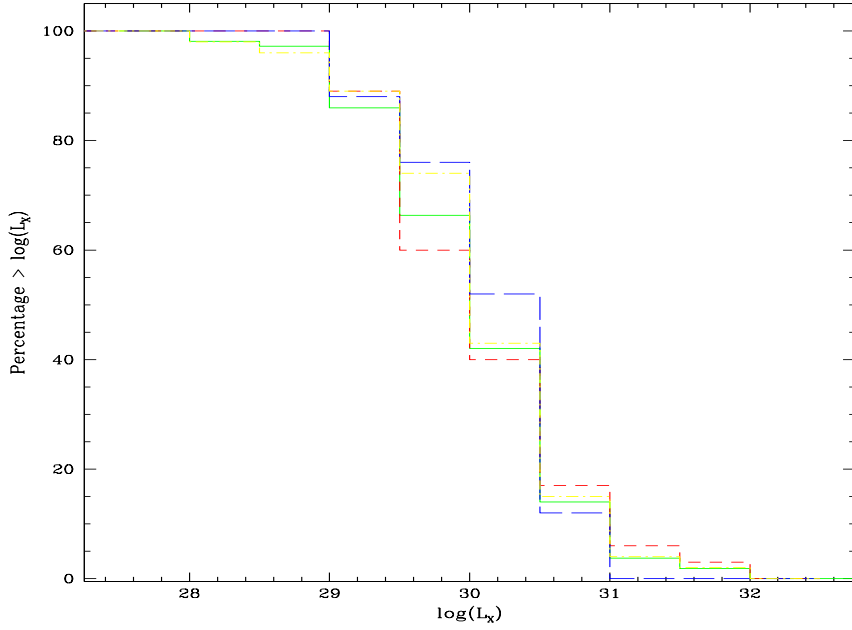
Figure 5.3: Luminosity distribution for the studied sample. Continous green line: the complete sample; red short-dashed line: the F stars; blue long-dashed line: the G stars; yellow dot-dashed line: the K stars.
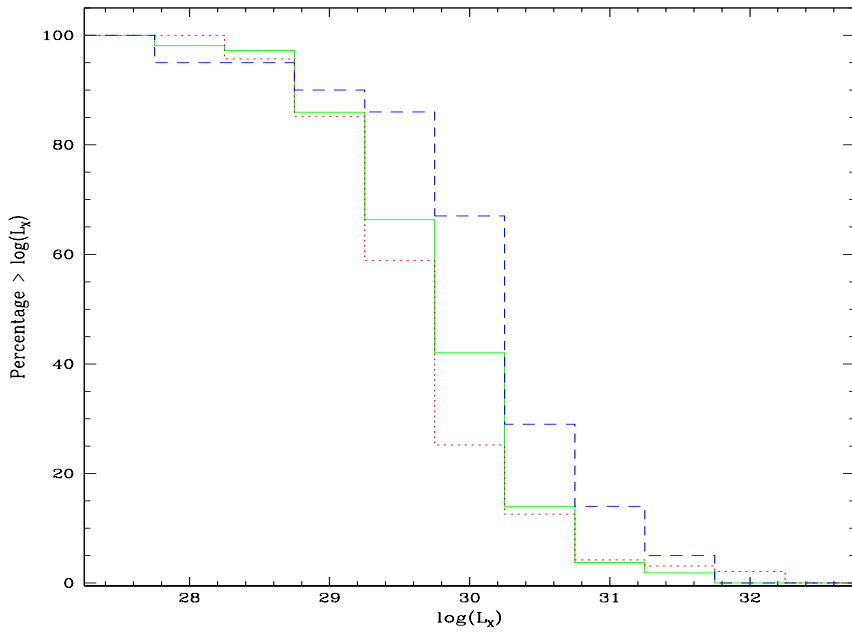
Figure 5.4: Luminosity distribution for the studied sample (continous green line), compared to the luminosity function for the EMSS sample (Fleming 1988, doted red line line) and the EXOSAT sample (Cutispoto et al. 1996, dashed blue line).

33

regions. For the earlier type stars ($(B - V) \leq 0.64$) I have included the saturation level calculated by Vilhu and Walter (1987), for the later spectral types the possible saturation surface flux found by Fleming (1988) for the EMSS sample he studied.

The first thing that can be noted in Fig. 5.1 is the large spread present for each spectral type. The spread is larger than can be accounted for by the large error from the X-ray luminosity, and is therefore real. It is an indication for the large spread in activity levels present among the stars in my sample.

Most of the stars in my sample stay bellow the upper limits obtained from previous works. The bluer stars, with $(B - V) \leq 0.64$, follow well the saturation level calculated by Vilhu and Walter (1987), while the redder stars with $(B - V) \geq 0.64$ follow the curve corresponding to the limiting surface flux of $F_X \sim 7 \cdot 10^7$ erg s^{-1} cm^{-2} found by Fleming (1988) for his EMSS sample. A few stars, though, do not follow this behavior, but have instead values for the ratio well above the saturation levels. If these stars were binaries, the excessive levels of X-ray emission could be understood, but for the most part, the over-bright objects are single stars. This is a surprising result, and still badly understood, since more data about the stars would be necessary to fully analyze it. One possible explanation would be that these objects are up to now unrecognized multiple systems.

Another notable feature in Fig. 5.1 is the lack of low X-ray luminosity objects for $(B - V)$ values above 1.0, or spectral type K4. For all earlier spectral types, the spread goes from an $\log(L_X/L_V)$ of $\sim$ -5.6 up to, and even above, the corresponding saturation limit. But for the later K stars, the lowest detected star has an X-ray to visual luminosity ratio of $10^{-3.5}$.

For those late K stars, the levels of activity $\log(L_X/L_V)$ between -4 and -5 correspond to X-ray luminosities between 28.5 and 27.5. According to the flux limit of the RASS, this means that such stars can only be detected if they lie within a radius of 36pc for the higher activity level, and 10pc for the lower one. Schmitt et al. (1995) have made a study of a complete, volume-limited sample of K stars. The sample was limited to the K stars within 7pc of the Sun. This study has shown that the X-ray luminosities corresponding to the absent activity levels are quite rare among the nearby K stars. Only 27% of the K stars in the volume-limited sample of Schmitt et al. (1995) have an X-ray luminosity of $\log(L_X) \geq 27.5$, which would make them detectable at distances of $\sim$ 10pc. My sample contains only 15 K stars of spectral type later than K4 and belonging to the Gliese catalogue. Among those stars, only 2 are within 10-11pc from the Sun, and another two lie at a distance of 12pc. According to the statistics from the sample of Schmitt et al. (1995), at the most one of these objects should have an X-ray luminosity of $\log(L_X) \sim 27.5$, making it detectable at this distance. This causes the gap observed in Fig. 5.1.

First sample	Second sample	χ^2	ν	P_{χ^2}
RASS complete sample	RASS single stars	0.997	8	0.998
RASS complete sample	RASS binaries	14.674	8	6.579e-2
RASS single stars	RASS binaries	20.947	8	7.289e-3
RASS complete sample	RASS F stars	1.342	8	0.995
RASS complete sample	RASS G stars	21.857	8	5.188e-3
RASS complete sample	RASS K stars	0.560	8	0.9998
RASS complete sample	EMSS sample	6.974	9	0.640
RASS complete sample	EXOSAT sample	20.598	8	8.296e-3

Table 5.2: Results of the χ^2 tests for the X-ray luminosity distributions.

5.3 Luminosity function

A useful characteristic of the sample is the X-ray luminosity function. The luminosity function for the whole sample can be obtained, as well as the functions for the different spectral types, since the X-ray luminosity has been determined for every star in the sample.

First, I shall consider the distribution of the X-ray luminosity for the whole sample. Fig. 5.2 shows the corresponding histogram, for the percentage of stars with $\log(L_X) \geq \log(L_X)_{\min}$. It is clear that the largest part of the sample has a luminosity between 29.0 and 30.5, with only very few stars at lower or higher luminosities. 75% of the stars lie in this mid-luminosity range. The small number of low-luminosity stars can be explained by the flux-limit of the ROSAT All-Sky Survey. Stars with X-ray luminosities below 28.5 could only be detected if they were within a distance of 36pc. For the high-luminosity stars, on the other hand, the small number of detections leads to the assumption that such sources are rare, at least within the detection sphere of the RASS.

Also shown in Fig. 5.2 are the distributions for the single stars and the multiple systems. In those cases the percentage is calculated relative to the corresponding subsample. It is clear that the detected multiple systems tend towards the higher X-ray luminosities. I applied χ^2 tests to the three distributions, whole sample, single star subsample and binary subsample.

If R_i is the number of events in bin i for the first sample, and S_i the number of events in the same bin for the second sample. Then χ^2 is defined as

$$\chi^2 = \sum_i \frac{(R_i - S_i)^2}{R_i + S_i} \tag{5.2}$$

The probability P_{χ^2} to find, in random distributions, a value of χ^2 that is larger or equal the one found (i.e. the significance of χ^2) is given by the incomplete gamma function
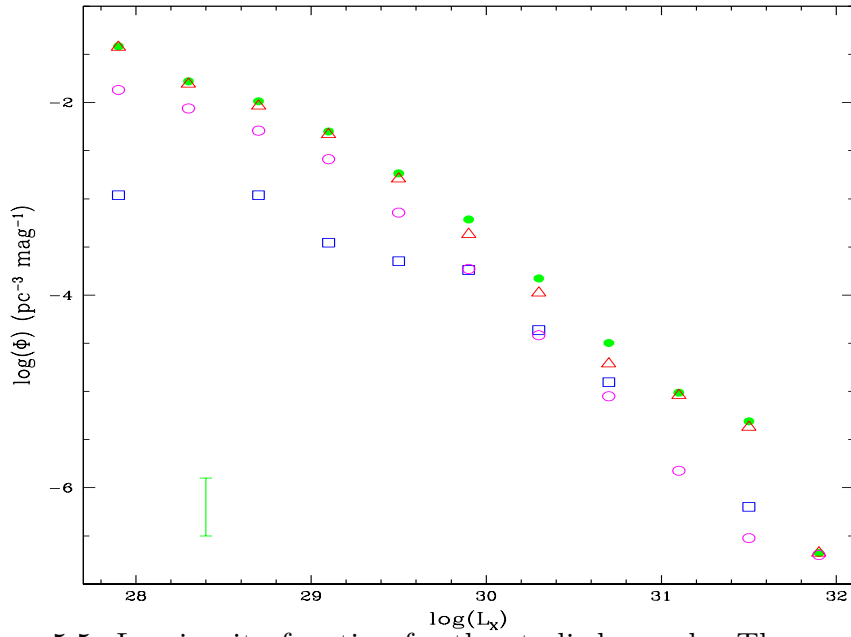
Figure 5.5: Luminosity function for the studied sample. The green filled points represent the whole sample, the red triangles the luminosity function for the single stars alone and the blue squares the luminosity function for the binaries. The empty circles represent the luminosity function for the EMSS subsample, for which ROSAT X-ray luminosites were available.
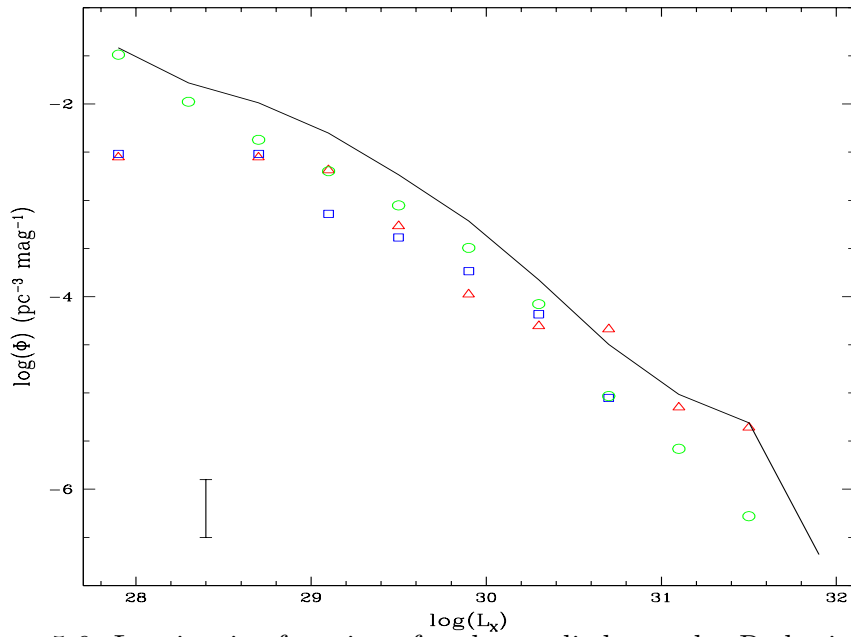
Figure 5.6: Luminosity functions for the studied sample. Red triangles: F stars; blue squares: G stars; green points: K stars. Both single stars and binaries are taken into account. The black line represents the luminosity function for the complete sample.
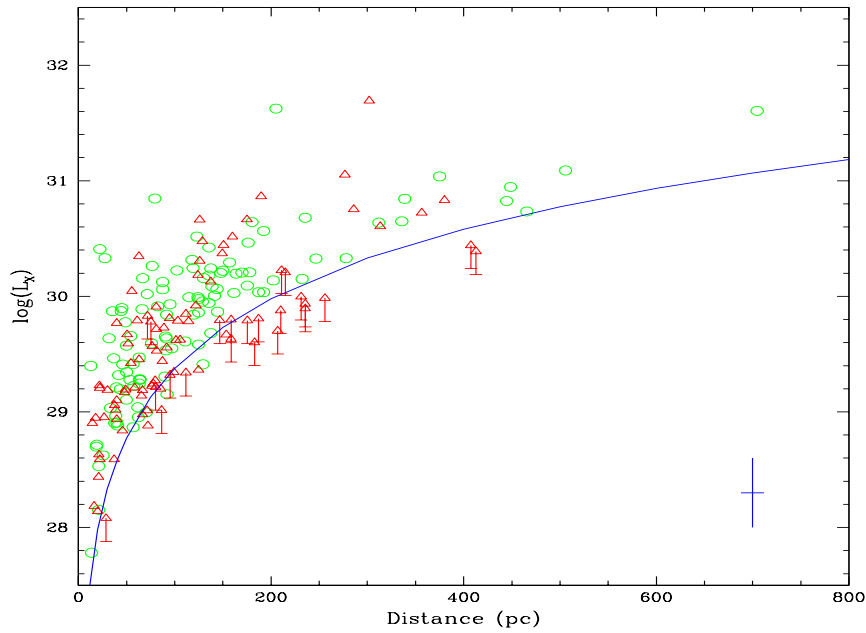
Figure 5.7: X-ray luminosity as a function of distance for the studied RASS sample (open circles) and for the EMSS sample (open triangles). Triangles with downward pointing lines represent upper limits for the X-ray luminosity of EMSS objects. The continous line represents the detection limit of ROSAT.
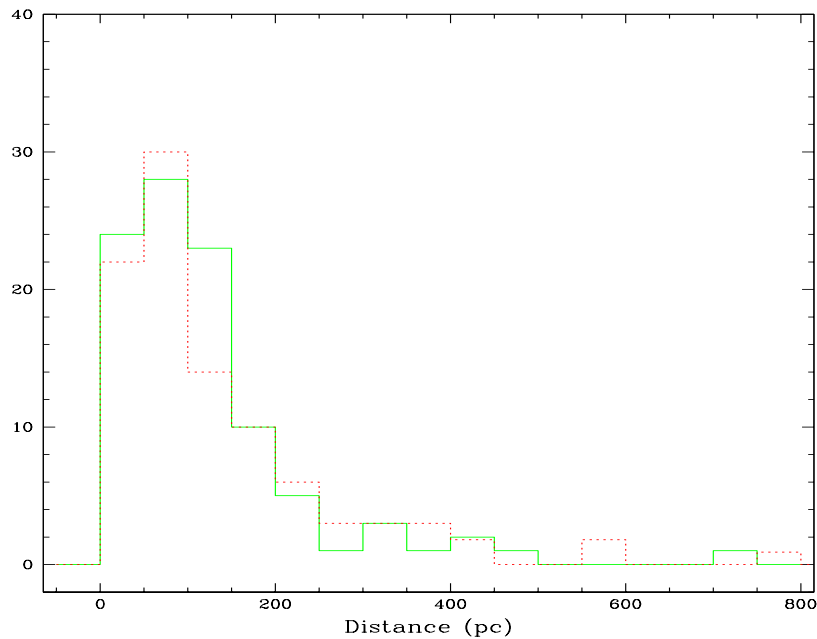
Figure 5.8: Histrogram of the distance distribution. Continuous green line: my RASS sample; red pointed line: the EMSS sample. Values are percentage of the whole sample.

$$Q(\frac{\chi^2}{2}, \frac{\nu}{2}) \equiv \frac{1}{\Gamma(\frac{\nu}{2})} \int_{\chi^2/2}^{\infty} e^{-t} t^{(\nu/2)-1} dt \qquad (5.3)$$

were ν represents the degrees of freedom and $\Gamma(x)$ is the Gamma Function. The test was taken from Press et al. (1992).

The smaller $Q(\frac{\chi^2}{2}, \frac{\nu}{2})$, the less probable it is that the two distributions compared are similar. A small value of $Q(\frac{\chi^2}{2}, \frac{\nu}{2})$ (of the order 0.05) means that the two samples compared are significantly different.

The results, listed in Table 5.2, show that the single stars have an X-ray luminosity distribution similar to the one of the complete sample, while the distribution for the binaries shows significant differences to both other distributions. The similarity between the distribution for the complete sample and the single star subsample can be explained by the fact that the single stars constitute the largest part of the complete sample. As for the binaries and multiple systems, most of the detected ones can be expected to be short-period interacting ones, where the interaction should enhance stellar activity. So their luminosity distribution should tend towards the higher luminosities.

The breakdown of the distribution among the three spectral type classes studied is shown in Fig. 5.3. The percentages are calculated again relative to the respective subsamples. From this plot, it is recognizable that the F stars tend to contribute more to both extremes of the luminosity distribution rather than to the mid-luminosity range of $\log(L_X)$ between 29.0 and 30.5. The G stars, on the other hand, have X-ray luminosities lying only in the mid-luminosity range, up to a $\log(L_X)$ of 31.0. The K stars are more evenly distributed over the whole range. χ^2 tests (Table 5.2) show that only the distribution for the G star subsample can be considered significantly different from the distribution for the complete sample. Since a large fraction of the G star subsample is composed of binaries, this is not surprising.

In order to compare the distribution of X-ray luminosities of my sample with those from the EMSS and EXOSAT samples, I plotted the three distributions in Fig. 5.4. The X-ray luminosities used for the EMSS sample are ROSAT luminosities taken from Fleming et al (1995). In this paper the results of a re-detection of the EMSS sources in the RASS are listed. Only 95 sources out of the 109 late-type sources studied by Fleming (1988) were re-detected with ROSAT. These sources were used to determine the X-ray luminosity distribution, to facilitate the comparison with my sample. The luminosities given for the EXOSAT sample, on the other hand, are the EXOSAT luminosities. A direct comparison between this sample and my RASS sample is more difficult, since the energy range of both surveys are very different (ROSAT: 0.1-2.4 keV, EXOSAT: 1-50 keV). The sample was added for completeness. The large difference in the distributions is hard to interpret. It would be useful to get ROSAT luminosities for the EXOSAT objects, to allow a better comparison of this sample, which

appears to be very different from both the EMSS and my RASS samples.

Figure 5.4 shows again a strong similarity between my sample and the EMSS sample, as is confirmed by the χ^2 test performed (see Table 5.2). Both have the strongest concentration of stars between $\log(L_X)$ of 29.0 and 30.5. The mean values of both samples are near to identical, $<\log(L_X)> = 29.77$ for my sample, and 29.68 for the EMSS sample. On the other hand, the median values are very different: 29.78 for my sample, and 29.62 for the EMSS sample. The difference in the median value is due to the uneven distribution of the sources between luminosity bins. The distribution is not even near Gaussian, having two bins with very large concentration of sources. Therefore I consider the difference of nearly 0.2 dex between the median values of the two samples as a negligible difference, caused by the errors inherent to such statistically small samples, and tend to consider both samples as coming from the same stellar X-ray population.

The one major difference between the two samples is the presence of very high X-ray luminosity ($\log(L_X) \geq 32$) stars in the EMSS. Four such stars are contained in the sample studied by Fleming (1988), of which one has been re-detected with ROSAT, and a second has an upper limit for its ROSAT luminosity. Such extremely luminous stars are not present in my sample. This is most probably due to the fact that such sources are extremely rare. But this difference could also be partly due to the identification criteria used in the identification programs as well as the spectral classification. The spectral classification is in so far critical, as it is sometimes difficult to distinguish luminosity classes (for instance dwarfs and subgiants), and a misclassification in the luminosity class would lead to a very large error in the distance and the X-ray luminosity.

To check out the validity of the assumption that both X-ray luminosity distributions, my sample's and the EMSS's, are significantly similar, I have applied to the distributions two statistical tests: the Wilcoxon test mentioned in Sect. 5.1, and the χ^2 test.

The results of both tests (Wilcoxon:$|U - n_1 n_2/2| = 9 < U_\alpha = 27$; P_{χ^2}=0.640, see Table 5.2) indicate that the null hypothesis, that the two X-ray luminosity distributions are similar, cannot be disproved. Both samples can be considered to have similar X-ray luminosity distributions. A similar χ^2 test applied to my RASS sample and the EXOSAT one confirms, on the other hand, the differences between the X-ray luminosity distributions to be significant.

Since all the stars of my sample have known X-ray luminosities, I can also construct luminosity functions for various subsamples. I can do this, since my sample can be considered complete within the studied fields.

To obtain the luminosity function, I use a method described by Schmidt (1968). For each star, the maximal radius and volume V_a at which it could still be detected by ROSAT is calculated. To take into account the spatial distribution of the stars in a disk, a new volume V_a' is defined:

$$dV_a' = e^{-z/z_0} dV_a \qquad (5.4)$$

where z is the height above the galactic plane, and z_0 is the stellar scale height (Upgren 1963). The values for the stellar scale height used were 115pc for the A star, 190pc for the F dwarfs, 340pc for the G dwarfs and 400pc for the giants, and 350pc for the K dwarfs. These are the same values as those used by Fleming (1988) to determine the X-ray luminosity function for the EMSS sample. The contribution of each star to the total luminosity function is then given by $1/V'_a$. The X-ray luminosities are binned in 0.4dex intervals, which roughly correspond to one optical magnitude.

The resulting luminosity functions for the available range of $\log(L_X)$ between 27.5 and 32.0 are shown in the Fig. 5.5 and 5.6.

Fig. 5.5 shows the luminosity function of the whole sample as well as those for the single stars and the multiple systems. The trends already visible in the corresponding X-ray distributions are even more marked here.

The luminosity function for the whole sample has the strongest slope between $\log(L_X)$ 29.0 and 31.5. The contribution of the binaries to the total luminosity function is small, with the largest contribution at the high-luminosity end. The single stars have nearly the same luminosity function as the complete sample. Unfortunately, the number of binaries in the sample is small, so their luminosity function is rather uncertain.

Also plotted in Fig. 5.5 is the luminosity function for the EMSS sample. The similarity between both this sample and my RASS one are again visible. Only toward the high-luminosity end do both samples differ from one another.

The luminosity functions for the F-, G- and K-stars subsamples are given in Fig. 5.6. In these cases also, the trends recognizable in the X-ray distribution are more notable. The luminosity function for the F stars rises strongly at the low-luminosity end, while the function for the G stars starts around $\log(L_X)$=30.5 and rises until $\log(L_X)$=29.0, where it flattens. The luminosity function that best reproduces the one for the whole sample is that of the K stars.

5.4   Distribution with distance

More information about the general properties of the sample is given by the distribution of the X-ray luminosity with distance. Fig. 5.7 shows a plot of L_X as a function of the distance for my sample as well as the EMSS sample. In this case also, the available ROSAT X-ray luminosities were used for the EMSS sample, to facilitate a comparison between the two samples.

Figure 5.7 is a plot of the X-ray luminosity as a function of distance for both samples. Here, as well as with the X-ray luminosity distribution, both samples display a similar behavior. A few of the EMSS stars have upper limits for their ROSAT luminosity that lie bellow the detection limit of the RASS. Apart from this, and the already mentioned, in the plot not visible, high-luminosity tail at $\log(L_X) \geq 32$, the distribution of the X-ray luminosity with distance is very similar for the two samples. This was at least partly substantiated by a 2

First sample	Second sample	χ^2	ν	P_{χ^2}
RASS complete sample	EMSS sample	9.436	12	0.665
RASS single stars	RASS binaries	46.588	11	2.544e-6

Table 5.3: Results of the χ^2 tests for the distance distributions.

dimensional Kolmogorov-Smirnov test applied to the two sets of (distance,L_X) data points.

The Kolmogorov-Smirnov test for two samples, as described by Fasano & Franceschini (1987), consists of determining the maximal difference D between the data points of both samples. The procedure was taken from Press et al. (1992).

The significance of this maximal difference is then given by:

$$P_{KS}(D > observed) = Q_{KS} \left(\frac{\sqrt{N}D}{1 + \sqrt{1 - r^2 \left(0.25 - 0.75/\sqrt{N} \right)}} \right) \qquad (5.5)$$

where Q_{KS} is defined as:

$$Q_{KS}(x) = 2 \sum_{J=1}^{\infty} (-)^{j-1} e^{-2j^2 x^2} \qquad (5.6)$$

The number of data points N for two samples is $N = \frac{N_1 N_2}{N_1 + N_2}$, and r is a combination of Pearson's r for each sample, $r = \sqrt{1 - 0.5(r_1^2 r_2^2)}$. The smaller P_{KS}, the less probable it is that both samples have the same distribution. A small value, of the order of 0.05, means that both samples have to be considered significantly different.

The results of this test, $D = 0.197$ and $P_{KS} = 0.101$, confirm the similarity of the distribution of X-ray luminosity with distance for both samples.

Figure 5.7 also shows a higher density of X-ray sources for distances of $\leq$ 200pc. To verify this, I have plotted the distance histograms for both the EMSS and my sample, only with percentages of the total sample instead of the number of objects for every bin. The histograms, in Fig. 5.8, confirm the higher concentration of stars at distances $\leq$ 200pc. Indeed, for my sample $\sim$ 85% lie within the sphere of radius 200pc, while for the EMSS sample, it is 76%. A χ^2 test for the two distributions shows again that both samples display strong similarities (see Table 5.3).

This result confirms the assumption made for the reddening of the stars. Most of them lie within distances that make a correction for reddening negligible.
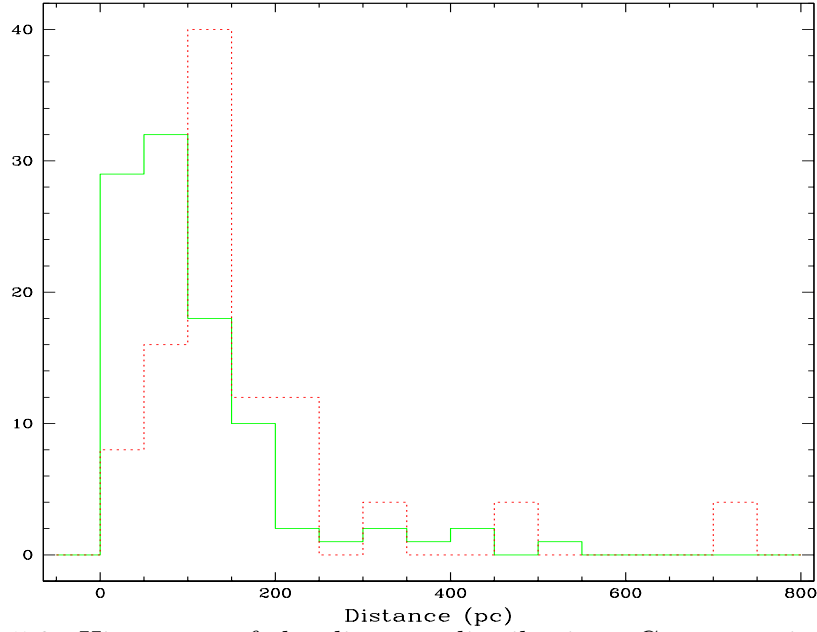
Figure 5.9: Histogram of the distance distribution. Green continuous line: the single stars in my sample; red dotted line: the binaries and multiple systems.
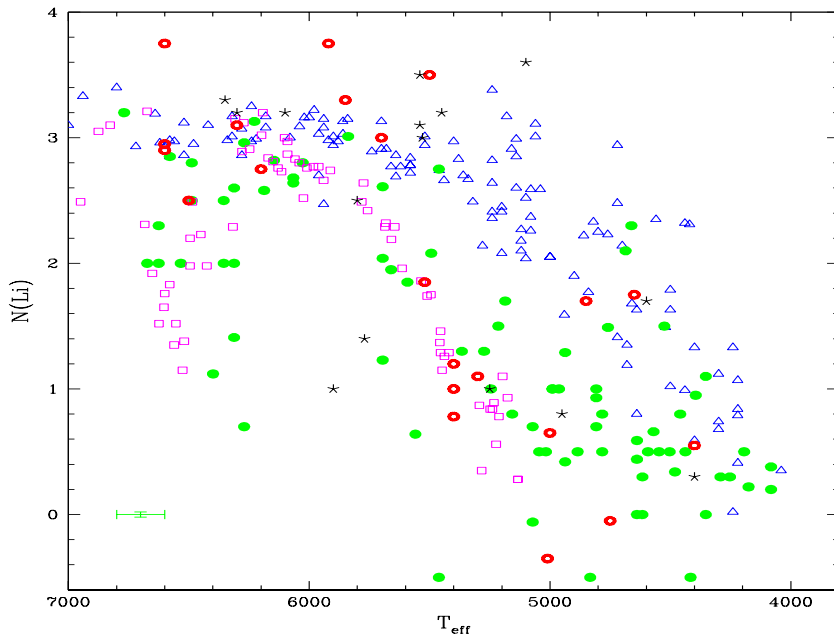
Figure 5.10: Lithium abundances for single stars as a function of effective temperature. Blue triangles: Pleiades data (Soderblom et al. 1993); purple squares: Hyades data (Balachandran 1995); green filled circles: my RASS sample; red empty circles: the EMSS sample (Fleming et al. 1995, Favata et al 1995); black stars: the EXOSAT sample (Tagliaferri et al. 1994).

45
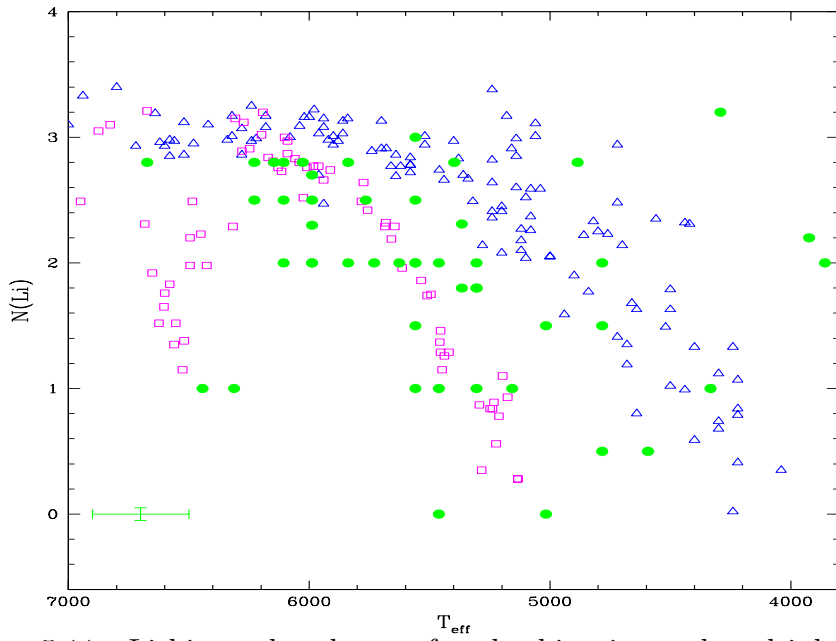
Figure 5.11: Lithium abundances for the binaries and multiple systems as a function of effective temperature. Blue triangles: Pleiades data (Soderblom et al. 1993); purple squares: Hyades data (Balachandran 1995); green filled circles: my RASS sample.
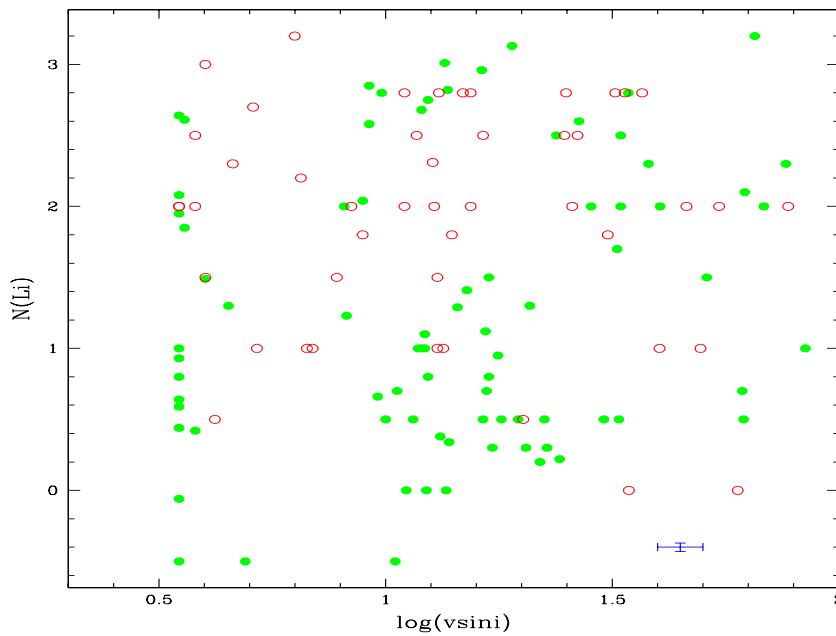
Figure 5.12: Lithium abundance vs rotational velocity for the single stars (filled circles) and multiple systems (empty circles) of the studied sample.

47
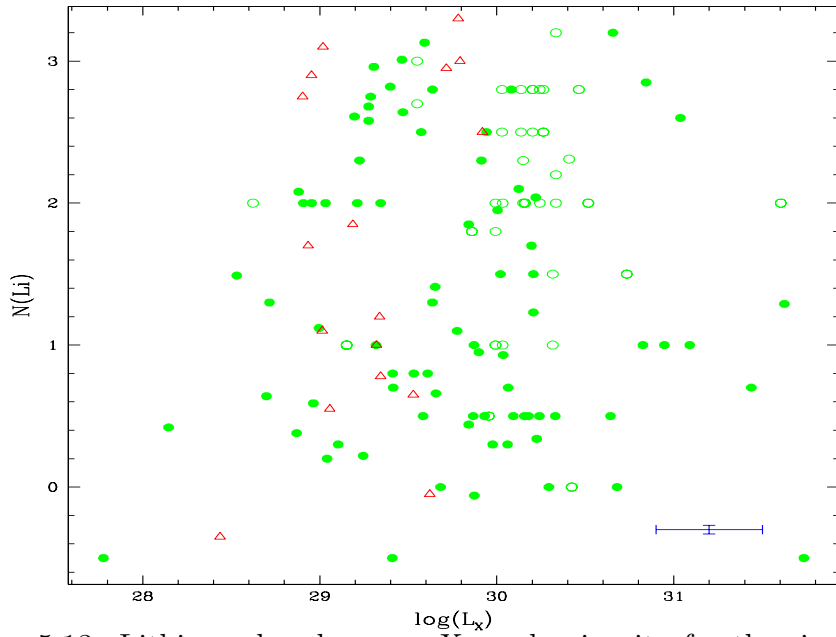
Figure 5.13: Lithium abundance vs X-ray luminosity for the single stars (filled circles) and the multiple systems (open circles) of the studied sample, as well as the stars from the EMSS with available lithium abundances (red open triangles).
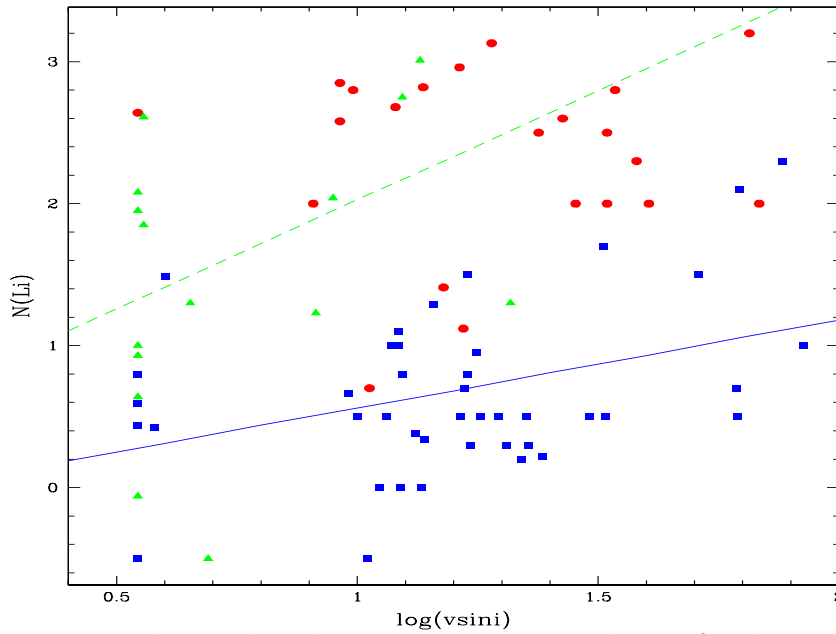
Figure 5.14: Lithium abundance vs. rotational velocity for the single stars of my sample. The red circles represent the early F stars, the green triangles the late F and G stars and the blue squares the K stars. The linear regression fits found for the F7 to G9 stars (dashed green line) and the K stars (continous blue line) are also plotted.
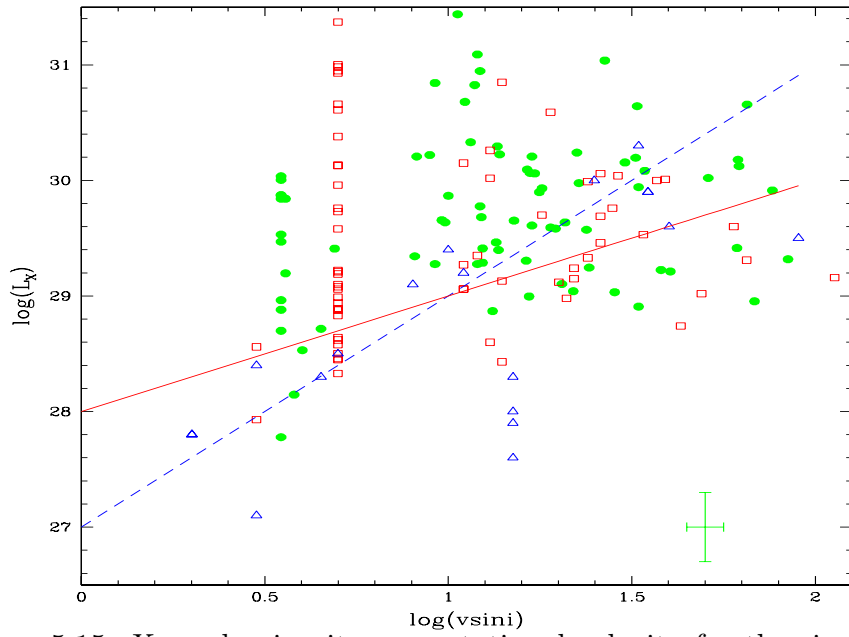
Figure 5.15: X-ray luminosity vs. rotational velocity for the single stars of my sample (green filled circles), the EMSS sample (empty red squares) and the opticaly selected sample of Pallavicini et al. (1981) (empty blue triangles). The correlations found by Pallavicini et al. (1981) (dashed blue line) and Fleming (1988)(continous red line) are also plotted.
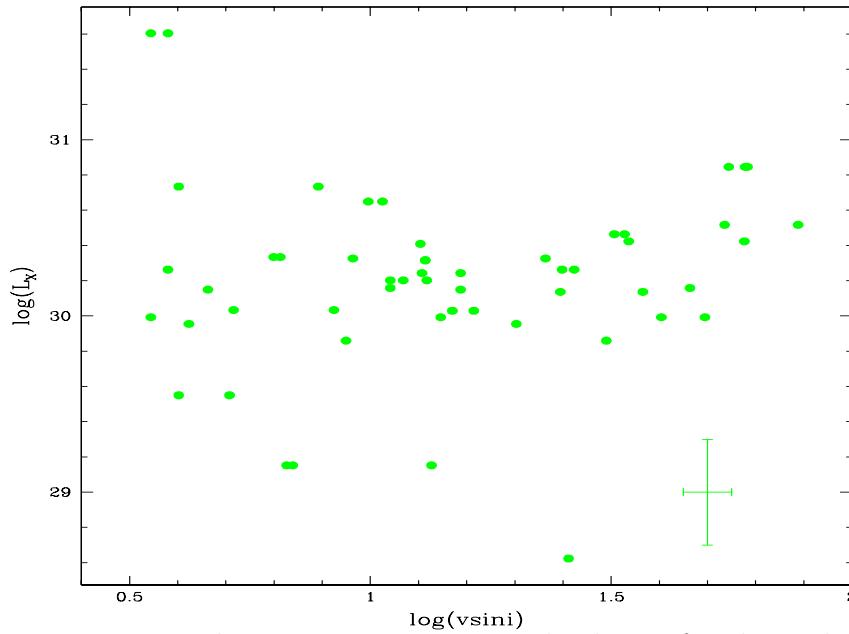
Figure 5.16: X-ray luminosity vs. rotational velocity for the multiple systems in my RASS sample.

Since both samples display such similarities in their general properties, as seen already in Sects. 5.1 and 5.3, and now with the distance distribution, I tend to assume that indeed both are representative of the late-type stellar X-ray population in the solar neighborhood.

Since my single stars and multiple systems subsamples had displayed previously differences, I also compare the distribution of distance for those two subsamples. This is done in Fig. 5.9. The percentage values are calculated relative to the number of sources in the corresponding subsample. The two subsamples display also in this case differences which are significant, as the χ^2 test shows (Table 5.3). Although the largest part of both subsamples is still contained within the first 200pc from the Sun, it is easy to recognize that the multiple systems tend towards larger distances. The peak of the distribution for the multiple systems lies in the 100-150pc bin, instead of the 50-100pc bin where the distribution of the single stars peaks. 79% of the single stars lie between 0pc and 200pc. A comparative percentage of the binaries, 80%, lie 50pc further, between 50pc and 250pc. Only 8% of the binaries are within 50pc from the Sun, compared to the 20% of the single stars. This is consistent with the X-ray luminosity distribution for the binaries, which tends towards the higher luminosities.

5.5 Lithium abundances

The lithium abundance determined for each star in my sample can be used to get a first idea of the star's age. Since the lithium in late-type stars is destroyed pretty fast once the stars reach the main-sequence, the lithium abundance was thought to be a good age indicator. But it has been noted in recent years that this simple model is not adequate. Many evolved late-type stars with high lithium abundances have been detected, stars which, according to the simple model should show no, or only very little lithium in the spectrum (see for example Favata et al. 1997 and 1996, Pasquini et al. 1994, Randich & Pallavicini 1991). So lithium abundances cannot be used as an age indicator, but can still give an idea of the evolutionary phase the star is currently passing through.

For this, the lithium abundances can be compared, for instance, to those of stars of similar spectral types belonging to open clusters of known age. The most popular, and among the best studied open clusters are the Zero-Age Main-Sequence (ZAMS) Pleiades cluster, with an age of $\sim 10^8$ years, and the older ($\sim 10^9$ years) Hyades cluster. The lithium data for the Pleiades was taken from Soderblom et al. (1993), the data for the Hyades was obtained from Balachandran (1995). Stars that show a lithium abundance well above the abundance of the Pleiades stars can be considered as Pre-Main-Sequence (PMS) stars. All other stars are either Main Sequence or older.

The distribution of lithium abundances for the single stars in my sample, compared to the abundances found for the Pleiades and Hyades clusters as well as some data from the EMSS and EXOSAT samples, is shown in Fig. 5.10,

while Fig. 5.11 shows a similar plot, but for the components of the binaries and multiple systems. The lithium abundance is given as N(Li)$\equiv \log \epsilon$(Li) relative to the hydrogen abundance N(H)=12.

The first thing that can be recognized from Fig. 5.10 is that among the single stars no PMS candidates are present. The youngest stars in my sample can only be ZAMS stars, with an age similar to that of the Pleiades stars. In this again, my sample differs from the EMSS sample, which does contain PMS candidates, as can be seen in Fig. 5.10.

Previous works, using the EMSS sample, have shown that about a third of the sample is composed of young stars, at least stars younger than the Hyades stars (Favata et al. 1993). A comparison of the lithium abundances for the single stars in my sample with those for the Hyades stars shows that about 32% (34 stars) of my sample has indeed lithium abundances high enough to be considered young, in accordance with the results of Favata et al. (1993).

For the binaries, the problem of age determination is even more complex than that for the single stars. It has been found that short-period interacting binaries often show a lithium overabundance. A proposed explanation for this is that the high rotation rate induced by the interaction between the binary components inhibits the transport of lithium to the deeper layers where it is destroyed. Only for one system is the case clear enough: it is the quadruple system RXJ 1122.0-2446, better known as HD 98800. The distance information from Hipparcos, as well as the lithium abundances (taken from Soderblom et al. 1997) show clearly that this system must be composed of PMS stars.

According to different studies of the lithium abundance in late-type stars, a correlation between stellar activity, or the related rotation, and the lithium abundance can be detected (Soderblom et al. 1993, Favata et al. 1997), although some samples do not display such a correlation (Favata et al. 1995). The dynamo model for the activity of late-type stars also predicts a slowing down of the rotation rate of a star through magnetic breaking. The older a star, therefore, the slower it should rotate, and the less active it should be. Since the lithium abundance is related to age, and also to rotation insofar as high rotation rates inhibit the destruction of lithium, a correlation between lithium abundance and rotation or X-ray luminosity would be a simple consequence of the models.

Since the stars in my sample show a wide range of lithium abundances, I decided to check whether a correlation between lithium and rotation or X-ray emission exists. Figures 5.12 and 5.13 show the lithium abundance as a function of either rotational velocity or X-ray luminosity.

Both the single stars and the binaries are represented. It is clearly recognizable that no correlation can be detected for the lithium abundance of the complete single star subsample with either parameter. To confirm the lack of correlation, I applied two statistical tests to my single star subsample, Pearson's r and Spearman's Rank Order Coefficient r_s.

Both are correlation tests, but differ in that Pearson's r compares the actual

data points while Spearman's Coefficient compares the ranks of the data point values within the whole sample.

For a sample composed of N data points (x_i, y_i), Pearson's r is defined as:

$$r = \frac{\sum_i (x_i - \bar{x})(y_i - \bar{y})}{\sqrt{\sum_i (x_i - \bar{x})^2}\sqrt{\sum_i (y_i - \bar{y})^2}} \tag{5.7}$$

with $\bar{x}$ being the mean value of all x_i's, and $\bar{y}$ the mean value of all y_i's.

The significance of Pearson's r is given by the error function, a special case of the incomplete Gamma function:

$$P_r \equiv 1 - \frac{2}{\sqrt{\pi}} \int_x^\infty e^{-t^2} dt \tag{5.8}$$

Spearman's Rank Order Coefficient considers the ranks of the x_i and y_i. If R_i is defined as the rank of x_i among all the other x values, and S_i the rank of y_i among all the y values, then Spearman's r_s is given by:

$$r_s = \frac{\sum_i (R_i - \bar{R})(S_i - \bar{S})}{\sqrt{\sum_i (R_i - \bar{R})^2}\sqrt{\sum_i (S_i - \bar{S})^2}} \tag{5.9}$$

The significance of r_s is given by computing

$$P_{r_s} \equiv t = r_s \sqrt{\frac{N-2}{1-r_s^2}} \tag{5.10}$$

which is distributed like Student's distribution with $n - 2$ degrees of freedom.

Pearson's r and Spearman's r_s have values lying between -1 and 1. The closer the result is to $|1|$, the more significant is the correlation between the two variables being compared is. On the other hand, the smaller the value for P_r and P_{r_s} are, the more significant the correlation between the two variables. These tests, as the χ^2 test before, have been taken from Press et al. (1992).

The results of both tests, listed in Table 5.4, for between the lithium abundances and the X-ray luminosity or the rotational velocity confirm the lack of correlation of N(Li) with either of the other parameters, when the complete sample is taken.

Many factors could cause the lack of correlation observed between lithium abundance and either X-ray luminosity or rotational velocity. One of the most obvious factors is the lithium dip in the early F stars. To verify whether the lithium dip could indeed be one of the causes for the absence of any notable correlation, I checked out possible correlations for the K single star as well as the late F/G single star subsample separately. The results are also listed in Table 5.4.

For the lithium abundance as a function of X-ray luminosity, the result remained, for both subsamples, the same as for the complete single star subsample.

Subsample tested	Variable correlated to N(Li)	r	P_r	r_s	P_{r_s}
all single stars	$v \sin i$	0.181	0.108	0.146	0.197
all single stars	$\log L_X$	-6.173e-2	0.586	-9.865e-2	0.384
all binary stars	$v \sin i$	-0.102	0.490	-3.990e-2	0.788
all binary stars	$\log L_X$	0.101	0.496	0.148	0.315
single F7 to G9 stars	$v \sin i$	0.469	2.759e-2	0.540	9.534e-3
single F7 to G9 stars	$\log L_X$	-0.207	0.356	-0.210	0.348
all F7 to G9 stars	$v \sin i$	0.233	0.153	0.367	2.166e-2
single K stars	$v \sin i$	0.380	1.195e-2	0.226	0.144
single K stars	$\log L_X$	0.133	0.395	0.133	0.396
all K stars	$v \sin i$	0.233	0.118	0.193	0.198

Table 5.4: Results of the correlation tests Pearson's r and Spearman's r_s tests for the lithium abundance.

There is no detectable correlation between these two stellar parameters for my sample. One reason for this could be that I do not have any very young stars, and so have only a limited range in N(Li) over which to look for correlations. But with the information available this cannot be verified.

For the lithium abundance vs. rotational velocity, on the other hand, the result changed drastically as soon as the single star subsample was divided into spectral types. Both for the K single stars and the G ones, there appears a clear correlation between N(Li) and $v \sin i$. I calculated the corresponding correlation functions using the least square fit method.

For the K stars subsample the best fit was

$$N(Li) \propto (0.620 \pm 0.236) \cdot v \sin i + (-6.060e - 2 \pm 0.295)$$

while for the late F and G stars, it was

$$N(Li) \propto (1.541 \pm 0.649) \cdot v \sin i + (0.485 \pm 0.586)$$

Both relations are drawn in Fig. 5.14. Statistical errors could be partly cause for this difference, since both subsamples are quite small, especially the late-F/G stars subsample (22 stars). The early F stars show no correlation, which is due to a large part to the strong dip in lithium abundance for main-sequence or older stars in that temperature range. No correlation could be found between lithium abundance and X-ray luminosity for any of the subsamples.

The binaries do not display any correlation, no matter how the sample is divided. But since for the binaries the errors in determining both rotational velocity and lithium abundance are larger, and the total number of objects small, a correlation could still exist, without being detected.
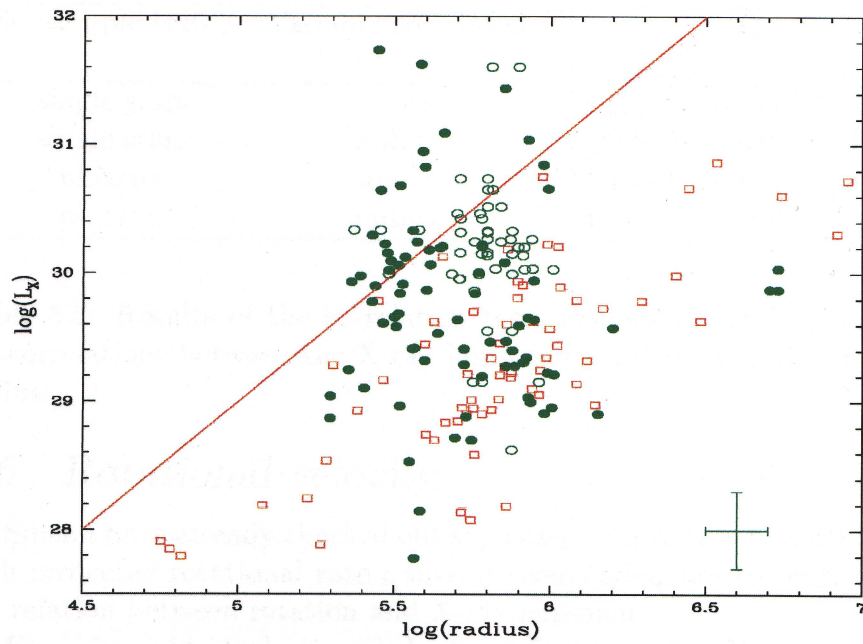
Figure 5.17: X-ray luminosity vs. radius for the single stars (filled circles) and multiple systems (empty circles) in my RASS sample, as well as the EMSS stars (empty red squares). The correlation and at the same time upper limit found by Fleming for his sample is given by the continous line. The error bars represent typical errors for my sample.

57

Subsample tested	Variable correlated to L_X	r	P_r	r_s	P_{r_s}
single stars	$v \sin i$	0.132	0.241	9.957e-2	0.376
single stars	radius	-5.293e-2	0.639	-0.151	0.179
binaries	$v \sin i$	2.957e-2	0.833	0.104	0.458
binaries	radius	-0.107	0.460	-0.128	0.376

Table 5.5: Results of the correlation tests Pearson's r and Spearman's r_s tests for correlations between the X-ray luminosity and the rotational velocity or the radius.

5.6 Rotational velocity

Since I have already checked out the possible correlation of lithium abundance with projected rotational rate $v \sin i$, it seems adequate to continue by studying the relation between rotation and X-ray emission.

First, I consider only the single stars of my sample. Older studies have shown that a clear correlation between the projected rotational velocity and the X-ray luminosity exists. This was detected first for an optically selected sample (Pallavicini et al. 1981), then also for the EMSS sample (Fleming 1988). But the correlation itself differs for both samples. Pallavicini et al. found a correlation between the X-ray luminosity and the square of the rotational velocity $L_X \propto (v \sin i)^2$, while Fleming gets a linear correlation between X-ray luminosity and rotation $L_X \propto v \sin i$.

Since the sample studied by Pallavicini et al. (1981) is optically selected, it seems reasonable to assume that the differences between the two correlations are a result of the strong bias present in this sample, and that the correlation found by Fleming corresponds more to the true correlation between X-ray luminosity and rotation. To check this assumption, I have plotted the X-ray luminosity as a function of rotational velocity for the single stars in Fig. 5.15. I have added both the EMSS sample and the sample of Pallavicini et al., as well as the correlations found for each sample.

The surprising result was a total lack of detectable correlation between projected rotational velocity and X-ray emission for my single star subsample. This is unexpected, since the model for the origin of the X-ray emission in late-type stars (see Chapter 1) clearly requires a correlation between the X-ray luminosity and rotation.

To make sure that the appearances really correspond to the "truth", I have calculated the linear correlation coefficient, Pearson's r, and the Spearman Rank Order Coefficient r_s, as described in the previous section, for my single star subsample. The results, listed in Table 5.5, confirm the lack of correlation between

$v \sin i$ and L_X.

The reason for this lack of correlation is hard to determine with the available data. One assumption would be that the lack of correlation comes from the use of the *projected* instead of the true rotational velocity. This would be easy to verify, but for this, the true rotational velocity has first to be determined, which will require more observations.

Another possibility would be the fact that my sample is composed mainly of high-activity stars, near the saturation limit. In this case, the lack of correlation would be even easier to explain, and would be even expected. Unfortunately, the global properties of my sample, first of all the spread present in the X-ray to visual luminosity ratio for every spectral type, imply that my sample is composed of stars with very different levels of activity, not only near-saturated ones.

One possible check of this hypothesis is by determining the radius for each single star, and looking for a correlation with the X-ray luminosity. Since saturation means that a star has its complete surface covered by active zones, the X-ray luminosity for saturated and near-saturated stars should correlate with the surface, and therefore also with the radius.

To estimate the radius, I used the information given by Popper (1980) as well as the $(B - V)$ index and the absolute magnitude derived from it. The radii obtained are listed in Table C.1. The result is plotted in Fig. 5.17.

Not so surprisingly no correlation can be detected in this case either. The calculated correlation coefficients confirm again the lack of correlation. Also noteworthy is the fact that quite a few stars have values of $\log(L_X)$ above the limit detected by Fleming (1988).

Clearly, my single stars subsample displays an unexpected behavior that is hard to explain with the available data. The lack of correlation between X-ray emission and rotation clearly doesn't come from a bias toward near-saturated stars in my X-ray selected sample. More data will be necessary to understand this behavior.

The binaries don't show any correlation either, neither between X-ray luminosity and rotation nor radius. But in this case, the behavior corresponds to the one shown by the stars in the EMSS sample, and can be due at least in part to the errors for $v \sin i$.

For the fast rotators among the binaries, determining with precision the rotational velocity is difficult, all the more so when the lines of the two line systems blend heavily. And the orbital motion of the system also contributes to the broadening of the lines, enlarging the error for the rotational velocity. More data will be necessary, spread over a few orbital periods, to try and get rotational velocities with less error. Only then will a conclusion about the correlation, or rather lack thereof, between rotation and X-ray luminosity be possible for the binaries.

6 Discussion

I presented optical observations of an X-ray selected sample of stars of spectral types F to K detected during the ROSAT All-Sky Survey. These stars are located in four high-galactic latitude fields of the southern hemisphere.

The observations were used to determine different stellar parameters. A spectral classification was done for each sample object, from which the distance and X-ray luminosity could be determined. Binary and multiple systems were identified. For each single star and multiple system component the effective temperature, radial and projected rotational velocities and lithium abundances were determined.

The distribution of the sample between the spectral types studied is as expected, within the statistical error limits. The largest part of the sample is by far composed of K stars, with about a third being F stars, and less than a fourth G stars. The G stars fraction is a bit lower than the one third of the sample expected, but this is certainly just a statistical effect.

The fraction of binaries is also near to the expected fraction of about a third of the sample. Although this estimate was done without differentiating between the short-period (1 to 15 days) active binaries, and the longer period ones. Most of the binaries detected are expected to be short-period ones, so the fraction of binaries to single stars would not be much modified by reclassifying the long period binaries into the single star subsample.

A study of the X-ray to visual luminosity ratio as a function of the color index $(B - V)$ showed that the activity levels for the sample stars cover 3 orders of magnitude. Most of the stars have X-ray luminosities well within the saturation limits found in previous works (Vilhu and Walter 1987 for the bluer stars, and Fleming 1988 for the later spectral types), with only a few stars being outside of those limits. This stands already in some contradiction to the results obtained by Fleming (1988). The study of the EMSS sample seemed to indicate that the stars in an X-ray selected sample tend rather towards saturation, instead of spanning such a broad range of activity levels.

The X-ray luminosity distribution as well as the distance distribution of my sample reproduces well the expected trends. Most stars have X-ray luminosities in the mid- to high-level range, from 10^{29} to $10^{31} erg \ s^{-1}$. Since the RASS was a flux-limited survey, it is expected that the sample should be biased towards higher levels of X-ray luminosities. Most of the stars detected are concentrated in a sphere of 200pc radius from the Sun. Considering the flux limitation of the RASS, of $\sim 2 \cdot 10^{-13} erg \ cm^{-2} \ s^{-1}$, this is very near to the limiting distance for the detection of stars with an X-ray luminosity of $10^{30} erg \ s^{-1}$. Since most of my stars have luminosities between $\log(L_X)$ of 29.0 and 31.0, a concentration of stars within such a relatively small radius is normal.

The X-ray luminosity and distance distributions of the single stars are very similar to the distributions obtained for the complete sample. Since the largest part of the sample is composed of single stars, this is a logical result. But the multiple system distributions show significant differences to the distributions of the complete sample. The multiple systems tend towards the higher X-ray luminosities and larger distances. The distribution over distance is shifted by 50pc compared to the distribution for the complete sample or for the single stars. Since most multiple systems are expected to be short-period binaries, the tendency toward higher X-ray luminosities is easy to understand. In the short-period interactive binaries, the components are tidally locked, and strongly influence one another. The tidal lock tends to synchronize the rotational velocities of the component stars with the binary period (Giuricin et al., 1984), which means that the stars have high rotational velocities and enhanced chromospheric and coronal activity. In some of the systems (Algol, W UMa), there is also mass transfer between the components, which means the existence of an accretion disk and hot spot (where the accreted matter falls upon the stellar surface) on one of the stars. The accretion disk and hot spot can contribute to the X-ray luminosity of the system.

The tendency towards larger distances is not so easily understandable. It can only mean that at high-galactic latitudes, active binaries are rare in the immediate (≤50pc) solar neighborhood.

A comparison of my RASS sample with the EMSS sample of Fleming (1988) has shown that both samples display very similar characteristics. The comparison between those two samples is insofar meaningful and interesting, because the EMSS sample was, until the launch of ROSAT, the largest X-ray selected sample studied, and has many similarities to my RASS sample. It has been observed in the soft X-ray range, is composed of stars detected during flux-limited "mini-surveys" (pointed observations with a large field of view) and is composed of a similar number of stars. And to make a comparison easier, most of the sample was re-detected in the RASS, so that the X-ray luminosities can be directly compared, since they were obtained with the same instrument.

For both samples, the distribution between the studied spectral types is identical within the statistical errors. The distance and X-ray luminosity distributions are also similar. Statistical tests have confirmed, or at least not disproved, this result. This is of importance, since the results obtained with such X-ray selected samples as the RASS and EMSS ones can be relevant to the study of X-ray emission in late-type stars only if the samples can be considered representative of the corresponding stellar X-ray population. Since both samples display such similarities despite their difference in spatial distribution, the assumption that indeed both samples are representative of the stellar X-ray population in the solar neighborhood is reasonable.

The lithium abundances obtained for the sample were used to estimate the evolutionary stages the stars have reached. Works using the EMSS observations

have revealed that X-ray selected samples contain a large fraction of young, or even very young stars (Favata et al. 1993, 1995). About a third of the studied sample was composed of stars that can be considered to be either still in a Pre-Main-Sequence phase, or as having just reached the Main-Sequence. A comparison of the lithium abundance obtained for my sample has shown that in this aspect too, the results corresponded to the expectations. 32% of my stars, particularly in the late-G and K spectral type range, have a lithium abundance significantly higher than the abundances found in the Hyades. Since in those stars the lithium is burned very rapidly once the Main-Sequence is reached, this leads to the conclusion that the stars must be young. But since their lithium abundance was not higher, for most even lower than the Pleiades abundances for the corresponding effective temperatures, the stars have most probably already reached the Main-Sequence. No Pre-Main-Sequence candidates could be detected among the single stars, and only one, already well known in the literature, was found among the multiple systems. It is the quadruple system HD98800 (Soderblom et al. 1997). This is a result differing from the ones obtained with the EMSS sample, since that sample contains clear PMS candidates. But it is easily understandable, if one considers that, in the regions studied, the PMS stars detected would have to be isolated PMS stars. Not many such stars are known, and their presence far from any larger star forming region is not yet understood (De la Reza et al. 1989, Rucinski 1992). It can be assumed that such sources are rare in the immediate solar neighborhood.

The activity level of a star has been found to be linked with its age. The magnetic fields necessary to heat up the corona are also responsible for slowing down the rotation of the star, leading to a reduction of the activity. Since the lithium abundance N(Li) is also dependent on age, a correlation between N(Li) and $\log L_X$ or $v \sin i$ can be expected. Such correlations were found for different samples (Soderblom et al. 1993, Favata et al. 1997). A correlation between lithium abundance and rotation could be found for two spectral type single star subsamples, the K stars and the late-F/G stars, but not for the complete single star subsample. The fact that no correlation could be found for the complete single star subsample can be ascribed to two reasons, firstly to the fact that lithium depletion is temperature dependent, and also to the inclusion of the early F stars, which lie in the range of the lithium dip. More factors can play a part in the absence of detectable correlation over the whole range of temperatures considered, but these seem to be the main factors, since a splitting of the single stars in spectral type groups reveals the existence of a correlation, as expected, between rotation and lithium abundance.

On the other hand, no splitting of the sample changed the fact that no correlation can be found between lithium abundance and X-ray luminosity. The reason for this is not understood, but could be linked to the results obtained when studying the correlation between rotational velocity and X-ray emission.

The models developed to explain the X-ray emission in late-type stars, as

mentioned in Chapter 1, link the X-ray emission to a dynamo mechanism. Magnetic fields existing in the convection zone of the stars are pushed to the surface, and the plasma enclosed in the field lines is heated to the temperatures observed in coronae and necessary for X-ray emission. The higher the rotation rate of a star, the stronger the dynamo mechanism is, and the more luminous the corona can be. A correlation between X-ray luminosity and rotational velocity (mostly the projected velocity $v \sin i$) has been observed in the previous studies, though a different correlation depending on the selection method used to create the sample.

The X-ray selected EMSS sample (Fleming 1988) shows a linear correlation $L_X \propto v \sin i$ for the single stars, while the optically selected sample studied by Pallavicini et al. (1981) has a different correlation, $L_X \propto (v \sin i)^2$. The difference can be explained by the assumption that the X-ray selected sample of Fleming is composed mainly of saturated or nearly saturated stars, for which the complete available surface is covered with active regions, while the sample of Pallavicini et al., being optically selected, includes stars of different activity levels, even low-activity ones. Since Fleming found also a correlation between L_X and the radii of his sample stars, but no correlation of L_X with the angular rotation rate, this assumption seems reasonable.

As my sample has been created using a similar selection method than the one used for the EMSS sample, it is reasonable to assume that the projected rotational velocities and X-ray luminosities of my single star subsample will show similar correlations to the ones found by Fleming (1988) rather than the correlation found by Pallavicini et al. (1981). All the more so since the EMSS sample and mine show strong similarities in their general X-ray properties. It is therefore strange that no correlation at all could be found between L_X and $v \sin i$ for the single stars of my sample. Nor could a correlation between the radii of the stars and the X-ray luminosity be found. This last result, together with the large spread in X-ray to visual luminosity ratio for any given spectral type, clearly indicates that my single star subsample is not composed only of saturated and near-saturated stars, but includes a whole range of activity levels. This makes the absence of any correlation between $v \sin i$ and L_X all the stranger and more difficult to explain, since in the case of a wide range of activity, a correlation closer to the one found by Pallavicini et al. (1981) should be detected. The simplest way of explaining the result, without contradicting model predictions, is that the statistical distribution of the projection factor $\sin i$ is such that it hides the correlation. But to verify this, it would be necessary to determine the true, unprojected rotational velocities of all the single stars, and see if those velocities correlate with the X-ray luminosity.

It is clear that the data available currently for the sample stars doesn't allow a further study of this last result, and the possible explanations for it. More observations are necessary in order to be able to verify whether the X-ray luminosity really does not correlate as expected with the rotation rate for my single stars, or whether this is just an effect due to the fact that the projected velocities

were used.

One way of checking this out would be by determining the true rotational velocity for as many single stars as possible. This can be done by using photometric light curves, at least for the faster rotators. Variations due to the transition of stellar spots can allow the determination of the rotation period. This method would be limited to stars for which such variations can be observed, meaning sufficiently "spotted" stars, which do not have their rotation axis parallel to the line of sight.

Another way of verifying predictions would be by looking directly for a correlation between the X-ray luminosity and the activity level of the stars. For this, spectral lines that are strongly influenced by the chromospheric activity can be used. Since models consider the X-ray emission to be linked with the chromospheric activity, an assumption that is based on observations and has been confirmed by various studies so far, this would be a much more direct check for the models than the correlation with rotation. Some of the best studied lines for chromospheric activity are the Ca II H & K lines. These lines have already been used in studies of the correlation between X-ray emission and activity (for example Eggen 1989, Piters et al. 1997). Part of the sample has already observations of those lines, and a full set of observations would allow the direct verification of the models.

The results obtained for my sample so far could also be checked against results of a similar study of the available northern sample, which contains 193 stars of spectral types A to K. With this sample added to mine, the statistical errors could be reduced, and the absence of any detectable correlation between rotation and X-ray emission revised.

Bibliography

Alonso, A., Arribas, S., Martinez-Roger, C., 1996, A&A 313, 873

Andrillat, Y., Jaschek, C., Jaschek, M., 1995, A&A 112, 475

Appenzeller, I., Thiering, I., Zickgraf, F.-J., Krautter, J., Voges, W., Chavarria, C., Kneer, R., Mujica, R., Pakull, M., Rosso, C., Ruzicka, F., Serrano, A., Ziegler, B. 1997, A&A, submited

Balachandran, S. 1995, ApJ 446, 203

Bessel, M.S. 1990, A&AS 83, 357

Bradt, H.V.D., Ohashi, T., Pounds, K.A. 1992, Ann. Rev Astr. Ap. 30, 391

Cassinelli, J.P., Swank, J.H. 1983, ApJ 271, 681

Christian, C.A., Adams, M., Barnes, J.V., Butcher, H., Hayes, D.S., Mould, J.R., Siegel, M. 1985, PASP 97, 363

Cousins, A.W.J. 1964, Mon. Notes Astron. Soc. South Africa 23, 175

Cutispoto, G., Tagliferri, G., Pallavicini, R., Pasquini, L., Rodono, M. 1996, A&A Suppl. 115, 41

Cruddace, R.G., Hasinger, G.R., Schmitt, J.H., 1988, *ESO Conference on Large Databases*, F. Murtagh, A. Heck (Eds)

Danziger, I.J., et al. 1990, ESO Messenger 62, 4

De La Reza, R., Torres, C.A.O., Quast, G., Castilho, B.V., Vieira, G.L. 1989, ApJ 343, L61

Downie, N.M., Heath, R.W. 1965, *Basic Statistical Methods*, 2nd ed., New York: Harper and Row

Duquennoy, A., Mayor, M. 1991, A&A 248, 485

Eggen, O.J. 1977, ApJ 215, 812

Eggen, O.J. 1989, AJ 98, 184

Fasano, G., Franceschini, A. 1987, MNRAS 225, 155

Favata, F., Barbera, M., Micela, G., Sciortino, S. 1993, A&A 277, 428

Favata, F., Barbera, M., Micela, G., Sciortino, S. 1995, A&A 295, 147

Favata, F., Micela, G., Sciortino, S. 1996, A&A 311, 951

Favata, F., Micela, G., Sciortino, S. 1997, A&A 322, 131

Fleming, T.A. 1988, Ph.D. dissertation, University of Arizona

Fleming, T.A., Gioia, I.M., Maccacaro, T. 1989, ApJ 340, 1011

Fleming, T.A., Molendi, S., Maccararo, T., Wolter, A. 1995, ApJ Sup., 99, 701

Giacconi, R., Gursky, H., Paolini, F., Rossi, B. 1962, Phys. Rev. Lett. 9, 439

Giommi, P., Tagliaferri, G., Beuermann, K., Branduardi-Raymont, G., Brissenden, R., Graser, U., Mason, K.O., Mittaz, J.D.P., Murdin, P., Pooley, G., Thomas, H.-C., Tuohy, I. 1991, ApJ 378, 77

Giuricin, G., Mardirossian, F., Mezzetti, M. 1984, A&A 141, 227

Gliese, W. 1982, A&A Suppl. 47, 471

Golub, L., Harnden, F.R. Jr., Maxson, C.W., Rosner, R., Vaiana, G.S, Cash, W. Jr., Snow, T.P. Jr. 1983, ApJ 271, 264

Kurucz, R.L. 1993, CD-ROM No 18

Linsky, J.L. 1990, in *Imaging X-ray Astronomy*, M. Elvis (Ed.), Cambridge University Press

Lucy, L.B. 1982, ApJ 255, 286

Maggio, A., Sciortino, S., Vaiana, G.S., Majer, P., Bookbinder, J., Golub, L., Harnden, F.R. Jr., Rosner, R. 1987, ApJ 315, 687

Mewe, R. 1979, Sp. Sc. Rev. 24, 101

Odewahn, S.C., Bryja, C., Humphreys, R.M 1992, PASP 104, 553

Pallavicini, R., Golub, L, Rosner, R., Vaiana, G.S., Ayres, T., Linsky, J.L. 1981, ApJ 248, 279

Pallavicini, R. 1989, Astron. and Astroph. Rev. 1, 177

Parker, E.N. 1979, *Cosmical Magntic Fields*, Clarendon Press

Pasquini, L., Pallavicini, R., Pakull, M. 1988, A&A 191, 253

Pasquini, L., Liu, Q:, Pallavicini, R. 1994, A&A 287, 191

Perryman, M.A.C., Lindegren, L., Kovalevsky, J., Hog, E., Bastian, U., Bernecca, P.L., Greze, M., Donati, F. et al. 1997 A&A 323, L49

Piskunov, N.E. 1992, in Proceedings of *Stellar Magnetism*, Glagolevskij, Yu.V., Romanuk, I.I. (Eds), Nauka, St. Petersburg

Piters, A.J.M., Schrijver, C.J., Schmitt, J.H.M.M., Rosso, C., Baliunas, S.L., Van Paradijs, J., Zwaan, C. 1997, A&A 325, 1115

Popper, D.M. 1980, Ann. Rev. Astr. Astrop. 19, 115

Press, W.H., Teukolsky, S.A., Vetterling, W.T., Flannery, B.P. 1992, *NUmerical recipes in Fortran*, 2nd Ed., Cambridge University Press

Randich, S., Pallavicini, R. 1991, Mem. Soc. Astron. Italia vol 62, 75

Randich, S., Gratton, R., Pallavicini, R. 1993, A&A 273, 194

Randich, S. 1997, private communication

Rosner, R., Golub, L., Vaiana, G.S. 1985, Ann. Rev. Astr. Ap. 23, 415

Rucinski, S.M. 1992, PASP 104, 311

Schmidt, M. 1968, ApJ 151, 393

Schmitt, J.H.M.M., Collura, A., Sciortino, S., Vaiana, G.S., Harnden, F.R. Jr., Rosner, R. 1990, ApJ 365, 704

Schmitt, J.H.M.M., Fleming, T.A., Giampapa, M.S. 1995, ApJ 450, 392

Soderblom, D.R. 1982, Ap.J 263, 239

Soderblom, D.R., Pendelton, J., Pallavicini, R. 1989, AJ 97, 539

Soderblom, D.R:, Jones, B.F., Balachandran, S., Stauffer, J.R., Duncan, D.K., Fedele, S.B:, Hudon, J.D. 1993, AJ 106, 1059

Soderblom, D.R., Henry, T.J., Shetrone, M.D., Jones, B.F., Saar, S.H. 1997, ApJ 460, 984

Sletteback, A., Collins II, G.W, Boyce, P.B., White, N.M. 1975, Ap.J. Suppl. 281, 137

Stocke, J.T., Morris, S.L., Gioia, I.M., Maccacaro, T., Schild, R.E., Wolter, A., Fleming, T.A., Henry, J.P. 1991, ApJ Suppl. 76, 813

Tagliaferri, G., Cutispoto, G., Pallavicini, R., Randich, S., Pasquini, L. 1994, A&A 285, 272

Tonry, J., Davis, M. 1979, AJ 84, 1511

Trümper et al. 1991, Nature 349, 579

Upgren, A.R. 1963, AJ 68, 194

Vilhu, O., Walter, F.M. 1987, ApJ 321, 958

Voges, W. 1993, Adv. Space Res. Vol. 13, No. 12, 391

Vogt, N., Geisse, H.S., Rojas, S. 1981, A&A Suppl. 46, 7

Zeidler, E. (Ed.) 1996, *Teubner-Taschenbuch der Mathematik*, Teubner Verlagsgesellschaft

Zickgraf, F.-J., Thiering, I., Krautter, J., Appenzeller, I., Kneer, R., Voges, W.H., Ziegler, B., Chavarria, C., Serrano, A., Mujica, R., Pakull, M., Heidt, J. 1997, A&A Suppl. 123, 103

Ziegler, B. 1993, Diploma thesis, University of Heidelberg

A   X-ray data of the sample

Here we list the data coming from the ROSAT observations of the sample objects. The columns of the table have following meaning:

Column 1: the ROSAT name of the object, composed of the prefix RXJ and a short form of the coordinates.

Column 2: the coordinates of the X-ray source, as determined from the ROSAT plates (equinox 2000.0). The error for these positions is typically 30".

Column 3: the countrates for the X-ray sources, in counts per second.

Column 4: the total exposure time for each source.

Column 5: the hardness ratio 1 of each source.

Table A.1: ROSAT X-ray data for the sources in the studied southern sample.

ROSAT Name RXJ	X-ray source coord. (2000.0)	Countrate (3)	t_{exp} (4)	HR 1 (5)
2246.6−3928	22 46 33.4 −39 28 44	0.172 ± 0.024	301.9	$+0.06 \pm 0.16$
2258.3−4149	22 58 15.7 −41 49 47	0.107 ± 0.030	121.3	$+0.57 \pm 0.48$
2305.1−3823	23 05 03.4 −38 23 37	0.066 ± 0.019	186.1	-0.23 ± 0.67
2306.5−3855	23 06 32.5 −38 55 47	0.124 ± 0.026	188.7	-0.03 ± 0.71
2323.3−3730	23 23 15.4 −37 30 53	0.131 ± 0.032	90.0	-0.12 ± 0.53
2331.4−4209	23 31 26.0 −42 09 43	0.153 ± 0.032	147.1	$+0.38 \pm 0.45$
2356.2−3903	23 56 10.1 −39 03 20	0.089 ± 0.028	115.0	-0.30 ± 0.64
0005.9−4145	00 05 52.2 −41 45 28	0.170 ± 0.031	175.2	$+0.09 \pm 0.22$
0015.0−4036	00 14 59.8 −40 36 07	0.058 ± 0.015	248.8	-0.18 ± 0.69
0022.2−3943	00 22 10.2 −39 43 25	0.037 ± 0.010	332.0	$+0.13 \pm 0.69$
0027.7−4126	00 27 42.4 −41 26 07	0.215 ± 0.027	297.4	$+0.28 \pm 0.13$
0028.8−3930	00 28 50.4 −39 30 55	0.061 ± 0.021	141.9	$+0.58 \pm 0.36$
0032.1−3827	00 32 08.9 −38 27 17	0.049 ± 0.016	363.4	$+0.42 \pm 0.43$
0035.7−2513	00 35 43.7 −25 13 59	0.111 ± 0.019	321.3	$+0.20 \pm 0.23$
0038.6−2335	00 38 35.4 −23 35 46	0.042 ± 0.011	331.7	$+0.03 \pm 0.71$
0041.2−2649	00 41 10.8 −26 49 58	0.075 ± 0.015	323.4	-0.22 ± 0.50
0042.7−2956	00 42 40.2 −29 56 49	0.037 ± 0.010	342.3	$+0.60 \pm 0.45$
0045.0−4014	00 45 01.4 −40 14 31	0.033 ± 0.009	369.9	-0.38 ± 0.61
0045.2−2455	00 45 09.1 −24 55 03	0.040 ± 0.011	336.3	-0.40 ± 0.59
0047.3−2245	00 47 17.7 −22 45 02	0.196 ± 0.023	355.2	$+0.09 \pm 0.14$
0050.6−4221	00 50 34.5 −42 21 20	0.030 ± 0.009	374.2	$+0.18 \pm 0.68$
0052.8−2728	00 52 45.4 −27 28 30	0.162 ± 0.026	236.4	-0.25 ± 0.20
0053.0−3021	00 52 59.1 −30 21 33	0.051 ± 0.012	331.7	-0.56 ± 0.36
0055.5−3731	00 55 28.8 −37 31 40	0.044 ± 0.011	360.7	-0.22 ± 0.67
0100.2−3818	01 00 13.3 −38 18 36	0.128 ± 0.018	389.4	$+0.37 \pm 0.16$
0105.4−4016	01 05 21.9 −40 16 09	0.032 ± 0.009	427.3	-0.11 ± 0.70
0116.8−3932	01 16 49.4 −39 32 10	0.024 ± 0.007	404.8	$+0.51 \pm 0.52$
0121.2−3729	01 21 10.0 −37 29 28	0.386 ± 0.032	370.8	$+0.03 \pm 0.09$
0121.5−4058	01 21 29.6 −40 58 17	0.058 ± 0.012	420.8	-0.03 ± 0.26

Table A.1 – continued.

ROSAT Name RXJ	X-ray source coord. (2000.0)	Countrate (3)	t_{exp} (4)	HR 1 (5)
0125.6−4148	01 25 33.7 −41 48 35	0.076 ± 0.014	406.4	$+0.20 \pm 0.24$
0126.4−4127	01 26 25.3 −41 27 54	0.037 ± 0.009	427.0	$+0.66 \pm 0.40$
0135.8−3956	01 35 48.5 −39 56 44	0.057 ± 0.012	363.0	$+0.03 \pm 0.71$
0136.8−3811	01 36 47.6 −38 11 19	0.072 ± 0.019	193.7	$+0.46 \pm 0.56$
0141.4−3808	01 41 25.5 −38 08 06	0.096 ± 0.015	424.8	-0.04 ± 0.20
0155.4−3846	01 55 21.5 −38 46 22	0.470 ± 0.042	260.5	-0.48 ± 0.12
0440.3−5856	04 40 17.2 −58 56 31	0.160 ± 0.044	81.9	-1.05 ± 0.50
0450.1−5856	04 50 07.4 −58 56 52	0.933 ± 0.252	14.7	
0454.9−5832	04 54 53.0 −58 32 54	0.470 ± 0.071	93.7	-0.04 ± 0.50
0501.5−5930	05 01 31.8 −59 30 51	0.024 ± 0.007	546.0	
0505.5−5728	05 05 30.8 −57 28 15	2.024 ± 0.015	131.2	-0.02 ± 0.08
0505.6−5755	05 05 33.9 −57 55 28	0.158 ± 0.020	405.2	$+0.17 \pm 0.16$
0505.8−6210	05 05 47.5 −62 10 10	0.063 ± 0.013	367.8	$+0.43 \pm 0.50$
0507.6−5459	05 07 33.3 −54 59 04	0.047 ± 0.013	269.8	
0508.1−5316	05 08 04.2 −53 16 20	0.072 ± 0.023	137.1	$+0.05 \pm 0.55$
0510.4−5732	05 10 26.2 −57 32 30	0.047 ± 0.009	577.8	-0.40 ± 0.50
0513.2−5507	05 13 11.5 −55 07 44	0.074 ± 0.022	158.4	$+0.44 \pm 0.57$
0516.1−6006	05 16 07.2 −60 06 14	0.136 ± 0.032	130.2	$+0.29 \pm 0.49$
0518.7−5803	05 18 43.3 −58 03 11	0.053 ± 0.020	129.2	$+1.00 \pm 0.50$
0519.2−5756	05 19 14.3 −57 56 59	0.023 ± 0.006	567.7	
0523.2−5751	05 23 15.4 −57 51 14	0.088 ± 0.020	227.9	-0.09 ± 0.22
0523.7−6041	05 23 41.4 −60 41 31	0.050 ± 0.011	388.9	$+0.37 \pm 0.50$
0525.8−5451	05 25 47.5 −54 51 11	0.019 ± 0.005	830.3	-0.31 ± 0.50
0527.6−6024	05 27 39.1 −60 24 53	0.172 ± 0.034	147.2	-0.32 ± 0.21
0528.3−6052	05 28 20.2 −60 52 03	0.045 ± 0.010	463.2	
0531.8−5239	05 31 50.3 −52 39 52	0.034 ± 0.013	212.9	-0.40 ± 0.59
0534.4−6006	05 34 24.6 −60 06 24	0.082 ± 0.026	123.2	-0.39 ± 0.45
0535.0−6110	05 34 57.5 −61 10 36	0.050 ± 0.016	181.4	$+0.51 \pm 0.39$
0538.2−5555	05 38 13.2 −55 55 55	0.020 ± 0.009	231.2	$+0.66 \pm 0.40$

Table A.1 − continued.

ROSAT Name RXJ	X-ray source coord. (2000.0)	Countrate (3)	t_{exp} (4)	HR 1 (5)
0538.4−5718	05 38 24.5 −57 18 57	0.072 ± 0.021	214.9	-0.19 ± 0.53
0539.1−5657	05 39 05.4 −56 57 54	0.032 ± 0.012	211.5	$+0.09 \pm 0.55$
0540.0−5343	05 40 01.4 −53 43 42	0.046 ± 0.015	216.4	$+0.44 \pm 0.57$
0541.1−6151	05 41 04.4 −61 51 23	0.077 ± 0.026	116.2	$+0.24 \pm 0.51$
0543.9−6005	05 43 51.7 −60 05 56	0.110 ± 0.026	166.2	-0.22 ± 0.51
0544.4−5523	05 44 21.1 −55 23 36	0.033 ± 0.012	246.2	$+0.55 \pm 0.37$
0545.3−5543	05 45 15.2 −55 43 22	0.020 ± 0.004	1328.5	-0.18 ± 0.50
0545.4−5411	05 45 26.9 −54 11 48	0.060 ± 0.015	273.9	-0.14 ± 0.52
0547.3−5450	05 47 17.8 −54 50 35	0.029 ± 0.009	377.4	-0.20 ± 0.68
0548.0−6241	05 48 01.0 −62 41 14	0.042 ± 0.014	205.8	$+0.53 \pm 0.51$
0549.7−5950	05 49 42.1 −59 50 10	0.073 ± 0.015	334.3	$+0.17 \pm 0.50$
1053.9−2423	10 53 51.1 −24 23 25	0.031 ± 0.041	365.5	$+0.46 \pm 0.56$
1056.1−2653	10 56 04.7 −26 53 13	0.049 ± 0.010	376.7	$+0.00 \pm 0.71$
1058.2−2926	10 58 11.6 −29 26 29	0.075 ± 0.015	314.5	$+0.01 \pm 0.52$
1101.1−3132	11 01 10.1 −31 32 48	0.083 ± 0.015	374.2	-0.02 ± 0.21
1102.1−2252	11 02 07.2 −22 52 37	0.030 ± 0.009	379.5	-0.37 ± 0.61
1108.5−3007	11 08 35.0 −30 07 41	0.015 ± 0.006	368.8	$+0.55 \pm 0.49$
1110.5−3027	11 10 35.7 −30 27 20	0.030 ± 0.009	352.2	$+0.61 \pm 0.33$
1110.6−2853	11 10 39.8 −28 53 34	0.049 ± 0.012	356.8	$+0.39 \pm 0.60$
1115.9−2750	11 15 54.8 −27 50 19	0.040 ± 0.015	176.4	$+0.47 \pm 0.43$
1118.3−3234	11 18 23.8 −32 34 48	0.031 ± 0.016	345.0	$+0.68 \pm 0.38$
1119.5−2351	11 19 29.4 −23 51 49	0.026 ± 0.009	333.3	$+0.60 \pm 0.46$
1121.5−3131	11 21 34.6 −31 31 40	0.051 ± 0.012	339.3	$+0.09 \pm 0.70$
1121.8−2411	11 21 49.1 −24 11 16	0.060 ± 0.013	349.4	$+0.23 \pm 0.50$
1122.0−2446	11 22 04.6 −24 46 34	0.973 ± 0.071	190.9	$+0.02 \pm 0.07$
1122.9−2545	11 22 55.9 −25 45 39	0.056 ± 0.013	329.4	-0.22 ± 0.51
1123.3−2342	11 23 18.1 −23 42 27	0.036 ± 0.010	354.6	$+0.09 \pm 0.70$
1124.0−2404	11 24 02.5 −24 04 34	0.067 ± 0.020	170.7	$+0.35 \pm 0.46$

Table A.1 − continued.

ROSAT Name RXJ	X-ray source coord. (2000.0)	Countrate (3)	t_{exp} (4)	HR 1 (5)
1132.9−3151	11 32 58.0 −31 51 42	0.424 ± 0.055	140.1	$+0.20 \pm 0.15$
1345.2−0043	13 45 10.3 −00 43 39	0.040 ± 0.010	412.9	$+0.21 \pm 0.68$
1354.2−0157	13 54 09.0 −01 57 03	0.039 ± 0.010	386.4	-0.08 ± 0.70
1354.9−0222	13 54 51.8 −02 22 53	0.026 ± 0.008	395.9	-0.06 ± 0.70
1355.5+0015	13 55 27.5 +00 15 26	0.025 ± 0.008	378.2	$+0.23 \pm 0.67$
1358.4−0139	13 58 24.9 −01 39 45	0.160 ± 0.020	415.6	$+0.48 \pm 0.14$
1358.9+0058	13 58 52.1 +00 58 00	0.038 ± 0.009	412.9	$+0.39 \pm 0.60$
1401.9+0025	14 01 53.4 +00 25 14	0.066 ± 0.012	424.2	$+0.15 \pm 0.51$
1404.0−0021	14 04 02.4 −00 21 41	0.090 ± 0.014	434.0	$+0.71 \pm 0.25$
1411.5+0121	14 11 31.7 +01 21 59	0.071 ± 0.012	460.0	-0.41 ± 0.43
1413.7−0050	14 13 40.5 −00 50 45	0.115 ± 0.017	407.6	$+0.08 \pm 0.21$
1428.2−0213	14 28 12.3 −02 13 40	1.341 ± 0.062	348.0	$+0.16 \pm 0.05$
1429.4−0049	14 29 26.1 −00 49 34	0.120 ± 0.018	356.7	$+0.41 \pm 0.20$
1432.1−0114	14 32 07.5 −01 14 42	0.040 ± 0.011	338.4	$+0.05 \pm 0.71$
1433.3−0126	14 33 20.5 −01 26 43	0.040 ± 0.011	324.0	$+0.34 \pm 0.62$
1436.9−0239	14 36 52.1 −00 39 57	0.027 ± 0.015	342.8	$+0.41 \pm 0.59$
1437.5+0216	14 37 29.3 +02 16 48	0.046 ± 0.012	341.9	$+0.60 \pm 0.33$
1442.7−0039	14 42 44.2 −00 39 57	0.129 ± 0.019	352.1	$+0.25 \pm 0.48$
1446.3+0153	14 46 15.9 +01 53 43	0.053 ± 0.012	356.6	-0.03 ± 0.54
1450.7+0055	14 50 39.8 +00 55 46	0.052 ± 0.013	300.4	$+0.81 \pm 0.18$
1451.9+0201	14 51 52.1 +02 01 05	0.057 ± 0.013	359.5	-0.18 ± 0.68

74

B   Stellar parameters

Various informations about the sources in the studied sample.

Column 1: the ROSAT name of the object.

Column 2: the coordinates, also for equinox 2000.0, of the stellar counterparts of the ROSAT sources.

Column 3: the separation between the X-ray position, as listed in tab. A.1 and the position of the counterpart, in arcseconds.

Column 4: the results from the spectral classification for the sample stars.

Column 5: the distance of the stars from the Sun, in pc, as determined using their spectral classification. Also given is the error, assuming an error for M_v of $\pm 0.3 mag$.

Column 6: the X-ray flux of the X-ray sources, in units of $10^{-12} \ erg \ s^{-1} \ cm^{-2}$, as well as the errors for the flux.

Column 7: the X-ray luminosities of the studied stars, in units of $10^{29} \ erg \ s^{-1}$, as well as the errors, as determined using the errors of the distance and X-ray flux.

Column 8: Catalogue name, if existing.

Column 9: spectral type, from literature (and SIMBAD) or from the first classification obtained from the identification program.

Column 10-14: V magnitude and color indices, from the photometric observations, with exception of the 4 very bright stars that have data from the literature.

Table B.1: Data for the counterparts of the sample sources.

ROSAT Name RXJ	Counterpart coord. (2000.0)	Diff. (3)	Spect. Type (4)	Dist. (5)	f_X (6)
2246.6−3928	22 46 33.2 −39 28 45	2.5	G6V	66^{+04}_{-03}	$1.49^{+0.37}_{-0.33}$
2258.3−4149	22 58 16.5 −41 49 36	14.0	G6V+K1V	136^{+13}_{-08}	$1.21^{+0.53}_{-0.68}$
2305.1−3823	23 05 04.5 −38 22 57	42.0	K1/3V	144 ± 10	$0.47^{+0.43}_{-0.30}$
2306.5−3855	23 06 34.4 −38 55 36	24.7	K4V	82 ± 3	$1.01^{+0.77}_{-0.58}$
2323.3−3730	23 23 14.2 −37 30 54	14.3	K1V	42 ± 2	$1.00^{+0.70}_{-0.52}$
2331.4−4209	23 31 25.7 −42 09 34	9.6	F8/9V+F9V+G1V*	$98.4^{+17.9*}_{-13.0}$	$1.58^{+0.77}_{-0.62}$
2356.2−3903	23 56 10.1 −39 03 05	15.0	K3V	$22.0^{+0.6*}_{-0.4}$	$0.60^{+0.58}_{-0.40}$
0005.9−4145	00 05 52.2 −41 45 08	20.0	G1V	$40.0^{+2.0*}_{-1.0}$	$1.50^{+0.51}_{-0.44}$
0015.0−4036	00 14 57.4 −40 35 24	49.7	G4V	141^{+8}_{-6}	$0.42^{+0.38}_{-0.27}$
0022.2−3943	00 22 10.6 −39 43 33	9.2	G3V+G5V	336 ± 17	$0.33^{+0.27}_{-0.19}$
0027.7−4126	00 27 42.7 −41 26 18	11.5	K4/5V	49^{+1}_{-2}	$2.11^{+0.43}_{-0.39}$
0028.8−3930	00 28 56.2 −39 30 50	67.3	K3/4V	92^{+4}_{-3}	$0.69^{+0.39}_{-0.31}$
0032.1−3827	00 32 09.9 −38 26 45	37.7	K3/4V	39^{+2}_{-1}	$0.52^{+0.32}_{-0.24}$
0035.7−2513	00 35 43.6 −25 14 03	4.2	G0V+G9V	119^{+15}_{-08}	$1.04^{+0.23}_{-0.29}$
0038.6−2335	00 38 36.2 −23 35 56	14.9	F3/4V	$62.5^{+3.8*}_{-3.5}$	$0.36^{+0.30}_{-0.21}$
0041.2−2649	00 41 11.5 −26 50 12	16.8	F9V+G8V	124^{+09}_{-14}	$0.53^{+0.35}_{-0.27}$
0042.7−2956	00 42 40.3 −29 56 39	10.1	G3V	178^{+15}_{-13}	$0.43^{+0.23}_{-0.18}$
0045.0−4014	00 45 00.8 −40 14 31	6.7	K4/5V	125^{+12}_{-11}	$0.21^{+0.20}_{-0.13}$
0045.2−2455	00 45 06.4 −24 55 12	37.8	F6V+G2V	192^{+21}_{-15}	$0.25^{+0.23}_{-0.16}$
0047.3−2245	00 47 17.8 −22 45 08	6.2	K4/5V	71^{+4}_{-3}	$1.72^{+0.37}_{-0.33}$
0050.6−4221	00 50 34.4 −42 21 17	3.2	F7/8V+G5V	202^{+29}_{-20}	$0.28^{+0.23}_{-0.16}$
0052.8−2728	00 52 45.6 −27 28 30	2.7	K5V	180^{+22}_{-20}	1.16 ± 0.35
0053.0−3021	00 52 59.8 −30 21 24	12.8	K2/3V	14	$0.27^{+0.19}_{-0.14}$
0055.5−3731	00 55 26.5 −37 31 24	31.7	G6V/IV*	$81.8^{+8.1*}_{-6.7}$	$0.32^{+0.28}_{-0.20}$
0100.2−3818	01 00 12.3 −38 18 38	11.9	K4V	54 ± 3	$1.32^{+0.31}_{-0.28}$
0105.4−4016	01 05 21.7 −40 16 11	3.0	F3V	$54.9^{+2.6*}_{-2.3}$	$0.25^{+0.22}_{-0.15}$
0116.8−3932	01 16 50.6 −39 32 07	14.2	K1V	21 ± 1	$0.27^{+0.17}_{-0.13}$
0121.2−3729	01 21 10.0 −37 29 29	1.0	K5V	45^{+3}_{-2}	$3.27^{+0.47}_{-0.44}$

76

Table B.1 − continued

L_X	Name	Sp_0	V	U-B	B-V	V-R	V-I
(7)	(8)	(9)	(10)	(11)	(12)	(13)	(14)
$7.74^{+3.07}_{-2.26}$		G	9.45	0.18	0.71	0.40	0.77
$26.48^{+23.30}_{-13.46}$	CD-52 16149	K3	10.60	0.03	0.73	0.45	0.85
$11.57^{+14.00}_{-08.00}$		K3	11.89	0.33	0.84	0.53	1.00
$8.19^{+7.37}_{-4.94}$		K5	11.33	0.58	1.00	0.59	1.13
$2.08^{+1.80}_{-1.17}$	HD 220345	K2III	9.35	0.54	0.87	0.47	0.89
$18.32^{+19.64*}_{-06.21}$	HD 221330	G0V	8.25	0.06	0.58	0.34	0.64
$0.34^{+0.39*}_{-0.22}$	HD 224228	K3V	8.22	0.82	0.96	0.56	1.04
$2.91^{+1.33*}_{-0.98}$	HD 105	G0V	7.52	0.04	0.60	0.34	0.66
$10.10^{+11.38}_{-06.68}$		G5	10.74	0.14	0.65	0.36	0.70
$44.56^{+44.60}_{-27.51}$		K3	11.96	0.12	0.67	0.39	0.78
$5.97^{+1.56}_{-1.54}$		K5Ve	10.74	0.87	1.14	0.50	0.95
$6.94^{+4.97}_{-3.36}$		K5V	10.61	0.84	1.01	0.56	1.04
$0.92^{+0.72}_{-0.47}$		K5V	9.74	0.75	1.01	0.53	1.03
$17.55^{+11.88}_{-06.60}$	SAO 166391	G2V	9.70	0.05	0.63	0.37	0.71
$1.68^{+1.79*}_{-1.06}$	HD 3581	F3IV/V	7.10	−0.04	0.41	0.25	0.47
$9.83^{+8.94}_{-5.95}$	HD 3877	G0V	9.86	0.01	0.60	0.37	0.71
$16.13^{+13.30}_{-08.24}$		G5	11.18	0.04	0.64	0.34	0.69
$3.83^{+5.14}_{-2.72}$		dK8e	12.35	0.79	1.03	0.63	1.18
$10.85^{+14.86}_{-07.55}$	HD 4288	F3/5V	9.89	−0.10	0.46	0.34	0.65
$10.47^{+3.87}_{-2.78}$		K8e	11.27	0.79	1.06	0.64	1.23
$13.75^{+18.60}_{-08.98}$	CD-43 234	F8	10.32	0.00	0.52	0.34	0.65
$43.88^{+30.04}_{-19.08}$		K8V	12.34	0.82	1.10	0.70	1.38
$0.06^{+0.05}_{-0.03}$	HD 5133	K3V+..	7.17	0.74	0.93	0.54	1.01
$2.57^{+3.22*}_{-1.76}$	HD 5403	G5V	8.67	0.22	0.71	0.41	0.77
$4.53^{+1.79}_{-1.28}$		K5Ve	10.58	0.77	1.04	0.61	1.15
$0.90^{+0.95*}_{-0.57}$	HD 6493	F3V	7.17	−0.05	0.40	0.24	0.46
$0.14^{+0.11}_{-0.07}$	HD 7777	G8	7.97	0.46	0.89	0.47	0.90
$7.92^{+2.49}_{-1.67}$		K8e	10.52	0.92	1.12	0.71	1.38

Table B.1 – continued

ROSAT Name RXJ	Counterpart coord. (2000.0)	Diff. (3)	Spect. Type (4)	Dist. (5)	f_X (6)
0121.5−4058	01 21 29.3 −40 58 17	3.4	F6V	$89.6^{+14.1*}_{-10.7}$	$0.47^{+0.19}_{-0.16}$
0125.6−4148	01 25 33.6 −41 48 36	1.5	G5V+K3V	130^{+08}_{-11}	$0.71^{+0.24}_{-0.21}$
0126.4−4127	01 26 25.3 −41 27 49	5.0	G8V	91^{+7}_{-8}	$0.44^{+0.21}_{-0.17}$
0135.8−3956	01 35 49.3 −39 56 30	16.7	F4V	$37.7^{+1.0*}_{-1.0}$	$0.48^{+0.36}_{-0.27}$
0136.8−3811	01 36 48.4 −38 11 26	11.7	K2/3V	137^{+15}_{-10}	$0.77^{+0.48}_{-0.36}$
0141.4−3808	01 41 28.6 −38 08 23	40.3	F3V	$41.9^{+1.2*}_{-1.1}$	$0.78^{+0.24}_{-0.21}$
0155.4−3846	01 55 22.5 −38 46 23	11.7	K5V	67 ± 4	$2.71^{+0.57}_{-0.52}$
0440.3−5856	04 40 17.6 −58 56 43	12.4	G5V/IV*	$31.0^{+0.9*}_{-1.0}$	$0.48^{+0.62}_{-0.14}$
0450.1−5856	04 50 09.7 −58 57 31	42.9	K2V	205^{+30}_{-20}	$8.40^{+5.40}_{-4.08}$
0454.9−5832	04 54 53.1 −58 32 54	0.8	F5V	$30.9^{+0.5*}_{-0.5}$	$3.81^{+2.01}_{-1.63}$
0501.5−5930	05 01 32.3 −59 30 46	6.3	F9V+G6V	232^{+21}_{-24}	$0.22^{+0.13}_{-0.12}$
0505.5−5728	05 05 31.1 −57 28 25	11.5	F7/8V	$11.6^{+0.1*}_{-0.1}$	$15.64^{+2.06}_{-1.94}$
0505.6−5755	05 05 36.4 −57 55 36	21.4	K4V	87^{+5}_{-7}	$1.46^{+0.33}_{-0.30}$
0505.8−6210	05 05 47.3 −62 09 58	12.1	K5V	157^{+21}_{-20}	$0.67^{+0.34}_{-0.44}$
0507.6−5459	05 07 34.3 −54 59 21	19.1	F5/6V/IV*	66.4^{+*}_{-}	$0.42^{+0.28}_{-0.22}$
0508.1−5316	05 08 07.0 −53 16 15	25.6	G3V	150^{+13}_{-11}	$0.62^{+0.48}_{-0.34}$
0510.4−5732	05 10 26.8 −57 31 59	31.4	F9V+G5V	247^{+21}_{-27}	$0.29^{+0.21}_{-0.16}$
0513.2−5507	05 13 12.0 −55 07 48	5.9	K5/7V	95^{+12}_{-14}	$0.79^{+0.52}_{-0.39}$
0516.1−6006	05 16 04.7 −60 06 55	45.0	K4/5V	102 ± 10	$1.34^{+0.76}_{-0.59}$
0518.7−5803	05 18 42.4 −58 02 48	25.0	K4V	236^{+31}_{-28}	$0.72^{+0.47}_{-0.36}$
0519.2−5756	05 19 16.4 −57 56 53	16.2	G5V+K3V	466^{+29}_{-56}	$0.21^{+0.13}_{-0.11}$
0523.2−5751	05 23 15.3 −57 51 01	13.0	K1/2V	136^{+13}_{-12}	$0.69^{+0.28}_{-0.23}$
0523.7−6041	05 23 43.2 −60 41 25	14.5	K5/7V	125^{+12}_{-19}	$0.51^{+0.28}_{-0.22}$
0525.8−5451	05 25 46.6 −54 51 21	12.7	K3V	129^{+14}_{-13}	$0.13^{+0.10}_{-0.07}$
0527.6−6024	05 27 40.3 −60 24 53	8.9	G9V	$19.6^{+0.2*}_{-0.2}$	$1.14^{+0.46}_{-0.38}$
0528.3−6052	05 28 21.9 −60 51 59	13.0	F5V	136^{+13}_{-06}	$0.40^{+0.24}_{-0.20}$
0531.8−5239	05 31 51.3 −52 40 00	9.3	K4V	137^{+17}_{-16}	$0.21^{+0.23}_{-0.15}$
0534.4−6006	05 34 26.3 −60 06 15	15.6	F7V	$80.1^{+4.6*}_{-4.1}$	$0.51^{+0.42}_{-0.29}$
0535.0−6110	05 34 57.6 −61 10 32	4.1	G4/5III*	$106.7^{+6.2*}_{-5.5}$	$0.55^{+0.32}_{-0.25}$

Table B.1 – continued

L_X	Name	Sp_0	V	U-B	B-V	V-R	V-I
(7)	(8)	(9)	(10)	(11)	(12)	(13)	(14)
$4.49^{+3.98*}_{-2.18}$	HD 8283	F3V	8.58	-0.06	0.48	0.29	0.55
$14.38^{+7.34}_{-5.91}$	VW Phe	G2	10.48	0.15	0.72	0.47	0.89
$4.33^{+3.00}_{-2.11}$		K0V	10.30	0.17	0.74	0.42	0.78
$0.81^{+0.69*}_{-0.47}$	HD 9895	F3/5V	6.41	-0.08	0.43	0.25	0.48
$17.43^{+17.43}_{-09.53}$		K0V	12.12	0.48	0.91	0.54	1.03
$1.63^{+0.62*}_{-0.50}$	HD 10481	F2V	6.18	-0.06	0.41	0.24	0.45
$14.35^{+5.23}_{-3.96}$		K5V	11.15	0.81	1.07	0.70	1.36
$0.55^{+0.78*}_{-0.18}$	HD 30003	G5V	6.53	0.23	0.68	0.38	0.72
$421.08^{+490.86}_{-244.25}$		K2	12.91	0.42	0.89	0.50	0.99
$4.34^{+2.53*}_{-1.95}$	HD 31746	F3V	6.11	-0.06	0.44	0.27	0.52
$14.14^{+13.08}_{-09.00}$		G2V	10.85	-0.00	0.58	0.35	0.67
$2.50^{+0.49*}_{-0.45}$	HD 33262	F7V	4.70		0.52	0.31	0.60
$13.30^{+5.11}_{-4.27}$		K8	11.41	0.67	0.99	0.61	1.19
$19.66^{+18.40}_{-14.60}$		K8	13.28	0.50	1.14	0.64	1.25
$2.21^{+1.78*}_{-1.23}$	HD 33514	F5V	7.34	-0.02	0.47	0.28	0.54
$16.65^{+18.05}_{-10.23}$		G6V	10.81	0.11	0.64	0.37	0.68
$21.19^{+21.32}_{-13.42}$		G2V	10.93	0.05	0.57	0.34	0.67
$8.54^{+9.28}_{-5.40}$		K8V	12.54	1.16	1.22	0.77	1.51
$16.76^{+14.74}_{-09.15}$		K5	12.12	0.90	1.08	0.63	1.19
$47.84^{+53.43}_{-29.29}$		K5	13.66	1.36	1.01	0.62	1.10
$54.24^{+44.16}_{-34.50}$		G5V	13.25	0.34	0.71	0.43	0.87
$15.14^{+10.30}_{-06.81}$		G	11.81	0.42	0.85	0.52	1.02
$9.48^{+8.11}_{-5.54}$		K5	12.98	1.25	1.19	0.67	1.33
$2.58^{+2.93}_{-1.63}$		K5	12.13	0.48	0.95	0.54	1.04
$0.52^{+0.22*}_{-0.18}$	HD 36435	G6V	7.01	0.28	0.77	0.41	0.80
$8.75^{+8.11}_{-4.68}$	HD 36530	F3V	9.53	-0.16	0.44	0.27	0.57
$4.81^{+7.78}_{-3.64}$		K8V	12.52	0.82	1.02	0.59	1.13
$3.91^{+4.05*}_{-2.40}$	HD 37402	F8	8.40	-0.03	0.50	0.30	0.58
$7.46^{+5.72*}_{-3.78}$	HD 37501	G5IV	6.33	0.48	0.84	0.45	0.88

Table B.1 – continued

ROSAT Name RXJ	Counterpart coord. (2000.0)	Diff. (3)	Spect. Type (4)	Dist. (5)	f_X (6)
0538.2−5555	05 38 08.6 −55 56 02	39.3	K3V	278^{+37}_{-31}	$0.23^{+0.17}_{-0.13}$
0538.4−5718	05 38 24.6 −57 19 08	11.0	F9V	139^{+10}_{-09}	$0.53^{+0.42}_{-0.30}$
0539.1−5657	05 39 05.2 −56 57 58	4.3	K1/2V	445^{+78}_{-54}	$0.28^{+0.24}_{-0.17}$
0540.0−5343	05 39 59.3 −53 43 43	18.6	K0V	164^{+24}_{-18}	$0.49^{+0.34}_{-0.25}$
0541.1−6151	05 41 04.9 −61 51 29	7.0	F3/4V	$204.1^{+44.6*}_{-31.1}$	$0.74^{+0.52}_{-0.38}$
0543.9−6005	05 43 49.7 −60 05 54	15.1	G7V+K2V	176 ± 12	$0.79^{+0.55}_{-0.41}$
0544.4−5523	05 44 20.7 −55 23 30	6.9	K5/7V	63^{+8}_{-9}	$0.37^{+0.22}_{-0.17}$
0545.3−5543	05 45 14.9 −55 43 27	5.6	F5V+G6V	89.2^{+*}_{-}	$0.15^{+0.09}_{-0.07}$
0545.4−5411	05 45 26.8 −54 11 34	14.0	K3V+K4V	129^{+13}_{-47}	$0.45^{+0.32}_{-0.24}$
0547.3−5450	05 47 17.9 −54 50 28	7.0	F6V	90^{+4}_{-8}	$0.21^{+0.20}_{-0.14}$
0548.0−6241	05 48 02.3 −62 41 08	10.8	K0/1V	170^{+34}_{-22}	$0.47^{+0.31}_{-0.23}$
0549.7−5950	05 49 41.1 −59 50 23	15.0	F7V+F7/8V+F7/8V	$141.4^{+38.8*}_{-25.0}$	$0.67^{+0.37}_{-0.29}$
1053.9−2423	10 53 53.0 −24 23 35	27.8	K4V	175^{+24}_{-23}	$0.34^{+0.22}_{-0.17}$
1056.1−2653	10 56 02.4 −26 52 47	40.3	G5V	120^{+10}_{-11}	$0.41^{+0.32}_{-0.23}$
1058.2−2926	10 58 14.1 −29 26 12	36.8	K0V+K5V	115^{+20}_{-17}	$0.62^{+0.38}_{-0.29}$
1101.1−3132	11 01 10.9 −31 32 49	10.3	K3V	57 ± 3	$0.68^{+0.22}_{-0.20}$
1102.1−2252	11 02 06.7 −22 52 33	8.0	K7V	57^{+8}_{-7}	$0.19^{+0.18}_{-0.13}$
1108.5−3007	11 08 34.4 −30 07 39	8.0	F5/6V	70 ± 3	$0.17^{+0.13}_{-0.09}$
1110.5−3027	11 10 34.1 −30 27 16	21.1	F3V+F7V	161^{+16}_{-14}	$0.34^{+0.17}_{-0.14}$
1110.6−2853	11 10 38.0 −28 54 01	35.9	F4V	339^{+33}_{-30}	$0.51^{+0.31}_{-0.24}$
1115.9−2750	11 15 55.9 −27 50 15	15.1	K5V	50 ± 3	$0.43^{+0.29}_{-0.22}$
1118.3−3234	11 18 23.1 −32 34 23	26.5	K2/3V	449^{+78}_{-52}	$0.37^{+0.28}_{-0.22}$
1119.5−2351	11 19 30.1 −23 52 02	16.2	K1V	145^{+18}_{-15}	$0.29^{+0.18}_{-0.14}$
1121.5−3131	11 21 35.4 −31 31 16	26.1	F7/8V	$59.4^{+3.4*}_{-3.0}$	$0.45^{+0.34}_{-0.25}$
1121.8−2411	11 21 49.8 −24 11 23	11.9	G3V	$48.0^{+2.3*}_{-2.0}$	$0.57^{+0.32}_{-0.25}$
1122.0−2446	11 22 05.4 −24 46 38	11.6	K4/5V+...	$46.7^{+7.1*}_{-5.5}$	$8.19^{+0.99}_{-0.94}$
1122.9−2545	11 22 56.0 −25 45 53	14.1	K4/5V	64^{+5}_{-4}	$0.40^{+0.28}_{-0.21}$
1123.3−2342	11 23 18.4 −23 42 25	4.6	G8III	$170.9^{+25.2*}_{-19.4}$	$0.31^{+0.26}_{-0.19}$
1124.0−2404	11 24 00.4 −24 04 44	30.4	F8V+G4V	705^{+50}_{-56}	$0.68^{+0.41}_{-0.32}$

Table B.1 – continued

L_X	Name	Sp_0	V	U-B	B-V	V-R	V-I
(7)	(8)	(9)	(10)	(11)	(12)	(13)	(14)
$21.39^{+26.06}_{-14.08}$		K7V	13.79	0.86	0.95	0.49	1.06
$12.13^{+12.73}_{-07.50}$		G	10.06	0.03	0.55	0.33	0.63
$66.93^{+102.89}_{-045.62}$		K2V	14.49	0.59	0.87	0.52	0.97
$15.71^{+19.30}_{-09.60}$		G2V	11.97	0.18	0.80	0.44	0.86
$36.77^{+56.27*}_{-23.93}$	HD 38372	F0V	9.62	0.02	0.38	0.27	0.50
$29.12^{+27.18}_{-17.04}$		G6	11.31	0.12	0.74	0.44	0.91
$1.76^{+1.81}_{-1.08}$		K5	11.70	1.26	1.23	0.68	1.26
$1.42^{+1.29*}_{-0.77}$	HD 38829	F5V	8.22	0.03	0.49	0.29	0.54
$9.01^{+9.56}_{-7.26}$		K5+K8	11.51	0.64	0.98	0.61	1.12
$2.02^{+2.30}_{-1.44}$	HD 39139	F6V	8.77	−0.04	0.49	0.28	0.57
$16.05^{+22.59}_{-09.98}$		G6V	12.00	0.30	0.79	0.47	0.92
$15.94^{+24.36*}_{-09.80}$	HD 39579	F7V	8.86	0.03	0.53	0.29	0.55
$12.37^{+14.09}_{-07.59}$		K2/5V	13.17	0.87	1.05	0.60	1.16
$6.94^{+7.59}_{-4.51}$		G8V+K8V	10.48	0.20	0.67	0.38	0.74
$9.83^{+11.92}_{-06.04}$		G5V	10.98	0.23	0.82	0.50	1.02
$2.60^{+1.20}_{-0.92}$		K7V	10.30	0.55	0.94	0.55	1.10
$0.74^{+1.16}_{-0.54}$	1E 1059.6-2236	K5Ve	11.77	1.05	1.28	0.80	1.55
$0.99^{+0.92}_{-0.59}$	HD 96803	F5V	7.94	−0.03	0.46	0.29	0.58
$10.68^{+8.65}_{-5.47}$	HD 97131	F2V	8.81	−0.01	0.41	0.26	0.53
$69.74^{+65.94}_{-39.13}$		F2V	11.05	0.08	0.42	0.26	0.51
$1.27^{+1.12}_{-0.71}$		K5V	10.92	0.78	1.17	0.64	1.22
$88.36^{+126.37}_{-060.07}$		K0V	14.56	−0.14	0.88	0.59	1.03
$7.36^{+7.69}_{-4.27}$		G4V	12.00	0.24	0.86	0.46	0.92
$1.89^{+1.82*}_{-1.13}$	HD 98753	F6V	7.74	−0.03	0.51	0.30	0.60
$1.57^{+1-12*}_{-0.69}$	HD 98764	G5	8.12	0.13	0.64	0.37	0.74
$21.36^{+10.20*}_{-06.62}$	HD 98800	K5V + ??	8.94	1.14	1.26	0.80	1.59
$1.92^{+1.89}_{-1.12}$		K8Ve	11.24	0.99	1.11	0.63	1.16
$10.86^{+15.21*}_{-07.58}$	HD 98975	K0	7.17	0.67	0.94	0.50	0.97
$402.43^{+340.96}_{-219.96}$		F8V	13.03	−0.03	0.54	0.34	0.66

Table B.1 − continued

ROSAT Name RXJ	Counterpart coord. (2000.0)	Diff. (3)	Spect. Type (4)	Dist. (5)	f_X (6)
1132.9−3151	11 33 00.4 −31 51 10	44.2	G8III	$39.6^{+1.4*}_{-1.2}$	$3.97^{+0.90}_{-0.81}$
1345.2−0043	13 45 10.3 −00 43 58	19.0	F8V	312^{+30}_{-27}	$0.37^{+0.27}_{-0.20}$
1354.2−0157	13 54 07.3 −01 57 56	58.8	F8V	$71.3^{+5.6*}_{-4.9}$	$0.31^{+0.26}_{-0.19}$
1354.9−0222	13 54 51.9 −02 22 50	3.3	F9V+G5V	$119.0^{+19.9*}_{-14.8}$	$0.21^{+0.19}_{-0.13}$
1355.5+0015	13 55 27.8 +00 15 23	5.4	K5/7V	62^{+9}_{-5}	$0.24^{+0.20}_{-0.14}$
1358.4−0139	13 58 24.8 −01 39 38	7.1	G0V+G5V	$125.9^{+29.4*}_{-20.0}$	$1.74^{+0.35}_{-0.32}$
1358.9+0058	13 58 52.2 +00 58 00	1.5	G9V+G9V	125^{+09}_{-16}	$0.39^{+0.25}_{-0.19}$
1401.9+0025	14 01 52.1 +00 25 20	20.4	F8V	$64.1^{+5.9*}_{-5.0}$	$0.60^{+0.33}_{-0.26}$
1404.0−0021	14 04 02.2 −00 21 45	5.8	F8IV+G3IV+G3IV*	$232.0^{+88.5*}_{-50.2}$	$1.09^{+0.31}_{-0.27}$
1411.5+0121	14 11 31.2 +01 21 44	16.8	F6V	$45.9^{+1.9*}_{-1.7}$	$0.43^{+0.26}_{-0.21}$
1413.7−0050	14 13 40.6 −00 05 40	5.2	F6V	$55.7^{+2.7*}_{-2.4}$	$1.01^{+0.30}_{-0.26}$
1428.2−0213	14 28 12.1 −02 13 36	5.0	G2III/IV+K0V*	$41.4^{+1.8*}_{-1.6}$	$12.49^{+0.73}_{-1.12}$
1429.4−0049	14 29 26.2 −00 49 46	12.1	K0V	87 ± 6	$1.26^{+0.34}_{-0.30}$
1432.1−0114	14 32 07.4 −01 14 47	5.2	K3/4V	91^{+9}_{-8}	$0.35^{+0.29}_{-0.20}$
1433.3−0126	14 33 20.5 −01 25 44	1.0	K0/1V	506^{+116}_{-075}	$0.40^{+0.30}_{-0.21}$
1436.9−0239	14 36 54.2 −02 44 32	34.0	K4/5V	111 ± 12	$0.28^{+0.19}_{-0.14}$
1437.5+0216	14 37 29.3 +02 16 40	8.0	F9V	26^{+1}_{-2}	$0.53^{+0.23}_{-0.19}$
1442.7−0039	14 42 44.3 −00 39 54	3.3	G5V+K1V	118^{+08}_{-10}	$1.24^{+0.56}_{-0.46}$
1446.3+0153	14 46 14.7 +01 53 13	26.9	A0V	$39.4^{+1.4*}_{-1.3}$	$0.43^{+0.28}_{-0.21}$
1450.7+0055	14 50 38.2 +00 55 53	25.0	F6V	375^{+36}_{-33}	$0.65^{+0.23}_{-0.20}$
1451.9+0201	14 51 53.3 +02 00 51	22.8	G5/6V	$38.9^{+2.1*}_{-1.8}$	$0.42^{+0.34}_{-0.25}$

Table B.1 − continued

L_X	Name	Sp_0	V	U-B	B-V	V-R	V-I
(7)	(8)	(9)	(10)	(11)	(12)	(13)	(14)
$7.43^{+2.29*}_{-1.88}$	HD 100407	G7III	3.54		0.94	0.33	0.68
$43.43^{+46.58}_{-26.66}$		F8V	11.67	0.04	0.39	0.32	0.62
$1.89^{+2.13*}_{-1.26}$	HD 121218	F8	8.32	0.01	0.54	0.31	0.62
$3.55^{+5.62*}_{-2.51}$	HD 121322	F8V	8.89	0.03	0.56	0.34	0.67
$1.10^{+1.52}_{-0.71}$		K8	11.95	1.11	1.28	0.73	1.40
$32.87^{+27.45*}_{-13.96}$	HD 121909	G0	9.61	0.05	0.61	0.35	0.71
$7.24^{+6.38}_{-4.40}$	BD+01 2868	G5V	10.38	0.28	0.76	0.43	0.84
$2.95^{+2.50*}_{-1.53}$	HD 122444	F8V	8.30	0.02	0.54	0.30	0.58
$70.10^{+101.47*}_{-037.73}$	HD 122798	F8V	8.50	0.07	0.58	0.34	0.67
$1.08^{+0.80*}_{-0.57}$	HD 124115	F7V	6.41	0.02	0.48	0.28	0.55
$3.74^{+1.58*}_{-1.21}$	HD 124425	F7V	5.90	−0.00	0.47	0.28	0.55
$25.64^{+4.02*}_{-4.10}$	HD 126868	G2IV+G4V	4.82		0.74	0.39	0.75
$11.50^{+5.26}_{-3.88}$	BD-00 2832	G5V	10.66	0.26	0.81	0.47	0.82
$3.40^{+4.08}_{-2.24}$	CM Vir	G2/5V	11.62	0.01	1.02	0.56	1.04
$122.72^{+191.96}_{-079.43}$		K5	14.32	1.08	0.78	0.50	0.92
$4.07^{+4.41}_{-2.49}$		K5	12.32	0.47	1.09	0.61	1.19
$0.42^{+0.24}_{-0.19}$	HD 128563	F8	6.45	0.11	0.56	0.32	0.62
$20.66^{+13.78}_{-09.89}$		K5	10.12	0.20	0.70	0.41	0.82
$0.80^{+0.60*}_{-0.42}$	HD 130109	A0V	3.72	−0.02	−0.01		
$109.05^{+67.79}_{-46.49}$		F	11.67	−0.01	0.48	0.29	0.58
$0.76^{+0.76*}_{-0.48}$	HD 131179	G5V	8.34	0.17	0.70	0.39	0.75

C   Spectroscopic Data

Here we list the results of the spectroscopic observations of the southern hemisphere sample stars.

Column 1: ROSAT name.

Column 2: Spectral type.

Column 3: $(B - V)$ colour index. For the single stars the observed index is listed, for the multiple system components the index taken from the tables of Cutispoto et al. (1996).

Column 4: Effective temperature.

Column 5: gravitational acceleration.

Column 6: Radial velocity, in km/s.

Column 7: Projected rotational velocity, in km/s. Values marked with an $*$ are literature values

Column 8: Lihtium abundance.

Column 9: Radius fo the star, in units of the solar radius.

Table C.1: Velocities, Li abundances for the southern hemisphere sample.

ROSAT Name RXJ	Spectral type	$(B-V)$ (3)	T_{eff} (4)	log(g) (5)	V_{rad} (6)	$v \cdot sini$ (7)	N(Li) (8)	Radius (9)
2246.6−3928	G6V	0.71	5461	4.48	−5.43	12.40	2.75	0.868
2258.3−4149a	G6V	0.71	5461	4.48	54.38	59.80	0.00	0.864
b	K1V	0.86	5017	4.55	−71.64	34.40	0.00	0.738
2305.1−3823	K1/3V	0.84	5072	4.57	−14.87	16.70	0.70	0.746
2306.5−3855	K4V	1.00	4662	4.60	22.42	76.40	2.30	0.717
2323.3−3730	K1V	0.87	4990	4.55	−117.05	84.30	1.00	0.72
2331.4−4209a	F8/9V	0.55	6027	4.40	−51.20	25.00	2.80	1.069
b	F9V	0.56	5988	4.41	48.70	26.50	2.50	0.900
c	G1V	0.62	5765	4.44	−7.40	3.80	2.50	1.251
2356.2−3903	K3V	0.96	4759	4.58	12.79	4.00	1.49	0.718
0005.9−4145	G1V	0.60	5838	4.44	1.61	13.50	3.01	1.001
0015.0−4036	G4V	0.65	5660	4.46	1.34	3.50	1.95	0.940
0022.2−3943a	G3V	0.65	5660	4.46	−5.55	9.90		0.936
b	G5V	0.68	5559	4.46	6.55	10.60		0.902
0027.7−4126	K4/5V	1.14	4353	4.60	23.54	12.20	1.10	0.697
0028.8−3930	K3/4V	1.01	4639	4.59	38.42	3.50	0.44	0.712
0032.1−3827	K3/4V	1.01	4639	4.59	−1.66	3.50	0.59	0.712
0035.7−2513a	G0V	0.60	5838	4.42	27.83	15.40	2.80	0.997
b	G9V	0.76	5305	4.52	4.92	12.80	2.00	0.820
0038.6−2335	F3/4V	0.41	6625	4.30	13.05	38.00	2.30	1.427
0041.2−2649	F9V	0.56	5988	4.41	10.22	3.50	2.00	1.083
b	G8V	0.74	5366	4.50	19.02	14.00	1.80	0.847
0042.7−2956	G3V	0.64	5695	4.46	23.56	8.20	1.23	0.955
0045.0−4014	K4/5V	1.03	4593	4.60	52.71	19.60	0.50	0.713
0045.2−2455a	F6V	0.48	6312	4.35	45.11	5.20	1.00	1.261
b	G2V	0.63	5730	4.45	67.22	8.40	2.00	0.956
0047.3−2245	K4/5V	1.06	4525	4.60	13.20	51.10	1.50	0.704
0050.6−4221a	F7/8V	0.52	6146	4.38	−1.32	36.80	2.80	1.174
b	G5V	0.68	5559	4.46	66.06	24.80	2.50	0.902
0052.8−2728	K5V	1.10	4438	4.60	33.34	32.70	0.50	0.699
0053.0−3021	K2/3V	0.93	4833	4.58	−13.65	3.50	−0.50	0.715
0055.5−3731	G6V/IV	0.71	5461	4.48	−43.95	4.90	−0.50	0.868
0100.2−3818	K4V	1.04	4570	4.60	32.75	9.60	0.66	0.713
0105.4−4016	F3V	0.40	6673	4.29	13.14	68.30	2.00	1.474
0116.8−3932	K1V	0.89	4937	4.55	−19.97	3.80	0.42	0.711
0121.2−3729	K5V	1.12	4395	4.60	6.83	17.70	0.95	0.690
0121.5−4058	F6V	0.48	6312	4.35	16.95	15.10	1.41	1.261

Table C.1 − continued

ROSAT Name RXJ	Spectral type	$(B-V)$ (3)	T_{eff} (4)	log(g) (5)	V_{rad} (6)	$v \cdot sini$ (7)	N(Li) (8)	Radius (9)
0125.6−4148a	G5V	0.68	5559	4.46	65.48	46.10	2.00	0.902
b	K3V	0.95	4783	4.58	−42.50	11.00	2.00	0.737
0126.4−4127	G8V	0.74	5366	4.50	16.10	20.80	1.30	0.847
0135.8−3956	F4V	0.43	6533	4.31	15.65	33.00	2.00	1.402
0136.8−3811	K2/3V	0.91	4885	4.58	34.15	22.40	0.50	0.717
0141.4−3808	F3V	0.41	6625	4.29	10.16	40.30	2.00	1.495
0155.4−3846	K5V	1.07	4503	4.60	38.05	30.30	0.50	0.705
0440.3−5856	G5V/IV	0.68	5559	4.46	10.85	3.50	0.64	0.906
0450.1−5856	K2V	0.89	4937	4.57	−16.65	14.40	1.29	0.711
0454.9−5832	F5V	0.44	6488	4.32	21.09	9.80	2.80	1.297
0501.5−5930a	F9V	0.56	5988	4.41	50.22	4.60	2.30	1.083
b	G6V	0.71	5461	4.48	77.96	15.40	2.00	0.864
0505.5−5728	F7/8V	0.52	6146	4.38	−1.86	13.70	2.82	1.142
0505.6−5755	K4V	0.99	4686	4.60	17.32	62.00	2.10	0.720
0505.8−6210	K5V	1.14	4353	4.60	23.69	13.60	0.00	0.697
0507.6−5459	F5/6V/IV	0.47	6355	4.34	15.89	8.10	2.00	1.244
0508.1−5316	G3V	0.64	5695	4.46	43.50	8.90	2.04	0.955
0510.4−5732a	F9V	0.56	5988	4.41	19.00	9.20		1.083
b	G5V	0.68	5559	4.46	42.66	23.10		0.902
0513.2−5507	K5/7V	1.22	4194	4.60	8.67	18.00	0.50	0.682
0516.1−6006	K4/5V	1.08	4481	4.60	43.48	13.80	0.34	0.702
0518.7−5803	K4V	1.01	4639	4.60	20.71	11.10	0.00	0.712
0519.2−5756a	G5V	0.68	5559	4.46	19.27	7.80	1.50	0.902
b	K3V	0.95	4783	4.58	23.59	4.00	1.50	0.737
0523.2−5751	K1/2V	0.85	5045	4.56	48.53	61.60	0.50	0.740
0523.7−6041	K5/7V	1.19	4253	4.60	2.16	22.70	0.30	0.691
0525.8−5451	K3V	0.95	4783	4.58	−0.49	12.40	0.80	0.717
0527.6−6024	G9V	0.77	5274	4.52	13.36	4.50	1.30	0.845
0528.3−6052	F5V	0.44	6488	4.32	6.50	33.00	2.50	1.297
0531.8−5239	K4V	1.02	4616	4.60	78.09	12.30	0.00	0.712
0534.4−6006	F7V	0.50	6228	4.37	16.66	19.00	3.13	1.187
0535.0−6110	G4/5III	0.84	5072	3.30	7.08	3.50	−0.06	2.969
0538.2−5555	K3V	0.95	4783	4.58	8.34	11.50	0.50	0.717
0538.4−5718	F9V	0.55	6027	4.41	−25.96	34.30	2.80	1.089
0539.1−5657	K1/2V	0.87	4990	4.56	60.18	11.80	1.00	0.722
0540.0−5343	K0V	0.80	5186	4.53	50.32	32.40	1.70	0.768
0541.1−6151	F3/4V	0.38	6769	4.30	11.06	65.20	3.20	1.425

Table C.1 – continued

ROSAT Name RXJ	Spectral type	$(B-V)$ (3)	T_{eff} (4)	log(g) (5)	V_{rad} (6)	$v \cdot sini$ (7)	N(Li) (8)	Radius (9)
0543.9−6005a	G7V	0.73	5397	4.48	43.83	33.70	2.80	0.852
b	K2V	0.91	4885	4.57	−19.93	32.10	2.80	0.720
0544.4−5523	K5/7V	1.23	4175	4.60	43.76	24.20	0.22	0.676
0545.3−5543a	F5V	0.45	6443	4.32	−9.62	13.40	1.00	1.321
b	G6V	0.71	5461	4.48	−23.04	6.70	1.00	0.868
c	G9V	0.76	5305	4.52	11.93	6.90	1.00	0.812
0545.4−5411a	K3V	0.95	4783	4.58	33.36	4.20	0.50	0.737
b	K4V	1.03	4593	4.60	32.47	20.10	0.50	0.733
0547.3−5450	F6V	0.49	6270	4.35	23.02	16.30	2.96	1.226
0548.0−6241	K0/1V	0.79	5215	4.54	17.14	16.90	1.50	0.777
0549.7−5950a	F7V	0.50	6228	4.38	−49.82	11.00	2.80	1.133
b	F7/8V	0.53	6106	4.38	8.40	11.70	2.50	1.184
c	F7/8V	0.53	6106	4.38	61.72	13.10	2.80	1.184
1053.9−2423	K4V	1.05	4547	4.60	−22.49	16.40	0.50	0.707
1056.1−2653	G5V	0.67	5592	4.46	28.49	3.60	1.85	0.920
1058.2−2926a	K0V	0.81	5157	4.53	−1.46	40.20	1.00	0.693
b	K5V	1.15	4333	4.60	13.42	49.50	1.00	0.435
1101.1−3132	K3V	0.94	4808	4.58	22.88	61.20	0.70	0.720
1102.1−2252	K7V	1.28	4082	4.59	16.62	13.20	0.38	0.642
1108.5−3007	F5/6V	0.46	6399	4.34	−9.37	16.60	1.12	1.279
1110.5−3027a	F3V	0.40	6673	4.29	−26.31	14.80	2.80	1.467
b	F7V	0.50	6228	4.37	16.41	16.40	2.50	1.187
1110.6−2853	F4V	0.42	6579	4.31	−10.67	9.20	2.85	1.383
1115.9−2750	K5V	1.17	4292	4.60	50.34	20.40	0.30	0.691
1118.3−3234	K2/3V	0.88	4963	4.58	7.05	12.20	1.00	0.727
1119.5−2351	K1V	0.86	5017	4.55	26.53	10.00	0.50	0.735
1121.5−3131	F7/8V	0.51	6187	4.38	4.60	9.20	2.58	1.154
1121.8−2411	G3V	0.64	5695	4.46	6.60	3.60	2.61	0.955
1122.0−2446a	K4/5V	1.17	4292	4.60		6.30∗	3.20∗	0.543
b	K7V	1.37	3924	4.59		6.50∗	2.20∗	0.409
c	M1V	1.41	3858	4.59			2.00∗	0.336
d	??							
1122.9−2545	K4/5V	1.11	4416	4.60	71.38	10.50	−0.50	0.696
1123.3−2342	G8III	0.94	4808	2.90	16.22	3.50	0.93	10.02
1124.0−2404a	F8V	0.53	6106	4.39	13.18	3.80	2.00	1.136
b	G4V	0.66	5626	4.46	16.48	3.50	2.00	0.930
1132.9−3151	G8III	0.94	4808	2.90	1.43	3.50	1.00	10.02
1345.2−0043	F8V	0.49	6270	4.39	−23.01	10.60	0.70	1.068

Table C.1 – continued

ROSAT Name RXJ	Spectral type	$(B-V)$ (3)	T_{eff} (4)	log(g) (5)	V_{rad} (6)	$v \cdot sini$ (7)	N(Li) (8)	Radius (9)
1354.2−0157	F8V	0.54	6066	4.39	−9.75	12.00	2.68	1.100
1354.9−0222a	F9V	0.56	5988	4.41	66.71	5.10	2.70	1.083
b	G5V	0.68	5559	4.46	−60.32	4.00	3.00	0.902
1355.5+0015	K5/7V	1.28	4082	4.60	58.80	21.90	0.20	0.642
1358.4−0139a	G0V	0.60	5838	4.42	52.09	77.30	2.00	0.997
b	G5V	0.68	5559	4.46	−105.39	54.40	2.00	0.902
1358.9+0058a	G9V	0.76	5305	4.52	45.71	30.90	1.80	0.820
b	G9V	0.76	5305	4.52	−77.96	8.90	1.80	0.820
1401.9+0025	F8V	0.54	6066	4.39	−2.73	3.50	2.64	1.100
1404.0−0021a	F8IV	0.53	6105	3.50	25.66	55.50		2.173
b	G3IV	0.66	5626	3.50	45.44	60.70		2.213
c	G3IV	0.66	5626	*	87.77	60.00		2.213
1411.5+0121	F6V	0.48	6312	4.35	−17.14	28.40	2.00	1.261
1413.7−0050	F6V	0.47	6355	4.35	0.57	23.80	2.50	2.359
1428.2−0213a	G2III/IV	0.70	5366	3.45	−5.49	12.70	2.31	5.000
b	K0V	0.81	5157	4.53				0.693
1429.4−0049	K0V	0.81	5157	4.53	10.74	3.50	0.80	0.762
1432.1−0114	K3/4V	1.02	4616	4.59	51.45	17.20	0.30	0.712
1433.3−0126	K0/1V	0.78	5245	4.54	−79.96	12.00	1.00	0.783
1436.9−0239	K4/5V	1.09	4459	4.60	−42.88	16.90	0.80	0.706
1437.5+0216a	F9V	0.56	5988	4.41	−0.03	25.80	2.00	1.083
b	K1V	0.86	5017	4.55	27.87	8.10	1.50	0.738
1442.7−0039a	G5V	0.68	5559	4.46	87.71	13.00	1.00	0.902
b	K1V	0.86	5017	4.55	65.20	13.00	1.50	0.738
1446.3+0153	A0V	−0.01	9409	4.27		340.0		2.366
1450.7+0055	F6V	0.48	6312	4.35	15.95	26.70	2.60	1.261
1451.9+0201	G5/6V	0.70	5493	4.47	−3.11	3.50	2.08	0.878

D   Standards

The standards used for the data analysis.

Table D.1: The photometric standards from the E-regions used in the photometry for the southern sample. Data from Vogt et al. (1981)

Name	Spectr. type	V	U-B	B-V	V-R	V-I	Coordinates (2000.0)
E101	A0V	7.704	0.091	0.087	0.038	0.084	01 27 34 -46 09 05
E102	A3III/IV	8.444	0.112	0.206	0.126	0.274	01 22 10 -46 13 18
E106	F3V	7.864	-0.026	0.396	0.235	0.472	01 31 29 -44 39 19
E107	F5V	8.613	-0.038	0.440	0.253	0.516	01 18 22 -44 11 49
E124	K0III	8.928	0.933	1.082	0.555	1.063	01 18 54 -44 56 12
E126	K0/1V	7.831	0.477	0.829	0.456	0.860	01 33 25 -43 54 08
E130	K2III	6.580	1.268	1.204	0.614	1.154	01 16 12 -42 00 53
E131	K2IIICNIa/	6.975	1.265	1.164	0.571	1.064	01 38 03 -46 05 03
E135	K3III	9.464	1.710	1.428	0.770	1.506	01 22 02 -44 25 31
E141	K1II	6.265	1.079	1.144	0.575	1.092	01 24 41 -44 31 41
E142	F0V	6.665	-0.007	0.330	0.196	0.397	01 38 30 -42 55 39
E146	B9III/Iv	7.857	-0.370	-0.086	-0.042	-0.091	01 17 00 -42 31 56
E164	A3V	6.640	0.123	0.129	0.068	0.143	01 41 41 -50 02 19
E168	K1/2III	8.567	1.202	1.177	0.595	1.122	01 36 41 -44 48 20
E176	K2III	8.946	1.410	1.302	0.680	1.302	01 18 01 -45 21 01
E301	B8V	8.059	-0.290	-0.085	-0.046	-0.095	06 37 24 -44 58 33
E304	A0V	7.689	-0.024	-0.014	-0.014	-0.030	06 37 42 -44 29 44
E326	F3/5IV	9.530	0.133	0.463	0.264	0.520	06 42 31 -45 21 21
E331	G8III	8.044	0.686	0.956	0.489	0.945	06 52 40 -46 48 33
E335	G8III	6.689	0.737	1.000	0.513	0.992	06 31 04 -43 43 03
E338	K3III	7.978	1.764	1.487	0.786	1.503	06 46 46 -44 58 26
E346	B8V	7.341	-0.388	-0.111	-0.050	-0.112	06 48 43 -43 48 06
E348	F5II/III	6.519	0.142	0.412	0.238	0.464	06 52 39 -42 30 15
E351	A0IV	6.829	-0.223	-0.065	-0.019	-0.050	06 58 00 -46 05 45
E352	A0V	6.219	-0.061	-0.003	-0.005	-0.014	06 58 41 -45 46 03
E389	B2III	7.215	-0.740	-0.156	-0.062	-0.142	06 45 10 -47 13 22
E502	B8/9V	8.061	-0.238	-0.032	-0.014	-0.031	12 08 43 -44 55 33
E507	A5V	8.830	0.178	0.178	0.098	0.206	11 57 47 -46 47 11
E523	G3V	8.378	0.180	0.652	0.350	0.680	12 00 04 -46 46 57
E584	K1/2III	7.431	1.316	1.280	0.660	1.248	11 54 50 -43 36 39

Table D.1 – continued

Name	Spectr. type	V	U-B	B-V	V-R	V-I	Coordinates (2000.0)
E633	K2III	6.834	1.208	1.176	0.602	1.134	14 38 13 -45 52 16
E682	B9V	6.890	-0.125	-0.017	0.005	0.012	14 35 10 -46 27 42
E703	B3III	8.110	-0.564	-0.004	0.014	0.027	17 36 40 -44 33 51
E722	F3/5V	7.254	-0.026	0.430	0.254	0.504	17 27 32 -43 32 30
E723	F0III	7.213	0.544	0.624	0.415	0.844	17 18 41 -46 47 56
E732	G8IIICNII	7.645	1.148	1.248	0.625	1.194	17 25 40 -44 46 45
E739	K4III	7.383	1.701	1.432	0.764	1.434	17 36 41 -44 52 43
E740	K3III	7.931	1.707	1.518	0.816	1.552	17 38 30 -44 52 32
E746	A0V	7.252	0.069	0.088	0.029	0.071	17 20 50 -45 25 11
E748	F3V	6.656	-0.012	0.382	0.223	0.443	17 24 43 -45 00 30
E749	A0V	5.789	-0.034	-0.011	0.005	0.012	17 41 16 -46 55 18
E750	ApSi	7.549	-0.351	-0.056	0.007	-0.010	17 29 52 -44 44 28
E765	G2/3V	7.165	0.164	0.648	0.356	0.692	17 37 53 -42 33 44
E766	G5V	7.245	0.250	0.722	0.393	0.764	17 39 00 -43 08 34
E780	B9V	5.759	-0.132	-0.048	-0.018	-0.040	17 18 47 -44 07 46
E782	B0.5Ib	6.458	-0.684	0.256	0.173	0.355	17 17 05 -44 46 42
E789	B8/9V	6.091	-0.250	-0.057	-0.017	-0.038	17 38 08 -42 52 47
E790	B9IV/V	6.918	-0.153	-0.026	-0.006	-0.012	17 43 37 -45 58 15
E801	ApEuCr	7.788	-0.036	-0.015	0.014	0.014	20 13 34 -45 35 25
E802	ApSi	7.915	-0.251	-0.042	-0.014	-0.046	20 02 10 -44 27 58
E803	A0V	8.744	0.017	0.030	0.002	0.010	20 00 53 -45 41 57
E809	A9IV	7.821	0.072	0.296	0.171	0.343	20 04 29 -44 56 48
E816	F5V	8.476	-0.034	0.448	0.260	0.518	20 08 01 -44 11 31
E826	G5/6III	6.542	0.568	0.885	0.460	0.887	20 11 15 -43 39 43
E828	K1III	6.567	1.222	1.224	0.633	1.208	20 02 36 -43 11 46
E830	K3/4III	6.954	1.854	1.509	0.803	1.546	20 05 07 -46 05 48
E834	K1III	7.846	1.232	1.188	0.602	1.132	20 09 26 -43 55 00
E840	K3/4III	8.104	1.640	1.416	0.756	1.431	20 06 55 -44 18 11
E846	G8IV	9.978	0.504	0.885	0.486	0.940	20 08 50 -44 24 55
E870	B8/9V	7.166	-0.216	-0.072	-0.024	-0.052	19 56 05 -44 00 44
E872	A9III/IV	6.727	0.078	0.274	0.148	0.284	20 26 04 -46 39 35
E876	K3/4III	8.880	1.900	1.526	0.822	1.598	20 01 04 -44 23 06

Name	Coordinates (2000.0)	Source
NGC 7790	23 58 40.30 +61 13 00.0	1,2
NGC 2419	07 38 08.45 +38 52 54.9	1
NGC 7006	21 01 29.34 +16 11 14.2	1,2

Table D.2: The open clusters used for standard stars in the photometry for the northern sample. The standards from the clusters and their colors are taken from: 1: Christian et al. (1985), 2: Odewahn et al. (1992).

Name	Spectr. type	V	$v_{\rm rad}$	Coordinates (2000.0)	Source
HD 4813	F8V	5.19	8.16	00 50 08.30 −10 38 28.3	1
HD 18455	G5	7.35	50.63	02 57 14.40 −24 58 07.6	1
HD 22879	F9V	6.74	120.31	03 40 19.70 −03 12 51.1	1
HD 30495	dG1	5.50	21.63	04 47 35.80 −16 56 12.5	1
HD 36079	G5II	2.84	-13.50	05 28 14.69 −20 45 29.8	2
HD 73752		5.05	44.60	08 39 08.82 −22 40 04.2	2
HD 109379	G5II	2.65	-7.00	12 34 23.16 −23 23 45.2	2
HD 150798	K2IIb/IIIa	1.92	-3.70	16 48 39.60 −69 01 38.0	2
HD 158614	G9IV/V	5.31	-80.62	17 30 24.14 −01 03 36.7	1
HD 168454	K2.5IIIa	2.70	-20.00	18 20 59.40 −29 49 40.0	2
HD 184985	F7V	5.47	-15.36	19 37 34.66 −14 17 59.2	1
HD 188512	G8IV	3.71	-40.71	19 55 18.54 +06 24 48.3	1

Table D.3: The radial velocity standards used for the southern sample. The standards were taken from 1: Duquennoy and Mayor (1991) 2: The Astronomical Almanach (1996)

Name	Spectr. type	V	$v \sin i$	Coordinates (2000.0)	Comments	Source
HD 1835	G2V	6.38	7.0	00 22 50.30 −12 12 37.3	Hyades group	1
HD 3196	F8V	5.20	30.0	00 35 13.40 −03 35 33.0		4
HD 4813	F8V	5.19	3.5	00 50 08.30 −10 38 28.3	CV?	1
HD 17206	F6V	4.50	36.0	02 45 04.90 −18 34 23.0		4
HD 27290	F2V	4.20	50.0	04 16 01.00 −51 29 21.3		2
HD 31993	K2III	8.30	29.0	05 00 08.10 +03 17 12.7		3
HD 36705	K1IV	6.83	85.0	05 28 44.50 −65 27 02.2	single	3
HD 37824	K2III	7.10	13.0	05 41 26.60 +03 46 40.3	SB1	3
HD 84117	F9IV	4.94	5.0	09 42 15.80 −23 55 09.0		4
HD 94388	F6V	5.24	8.3	10 53 29.20 −20 08 07.0		4
HD 101309	K1IV	8.50	20.0	11 39 22.50 −39 23 04.0		3
HD 101379	G5IIIp	5.17	14.0	11 39 29.80 −65 23 52.0		3
HD 102634	F7V	6.15	6.5	11 49 01.86 −00 19 06.9		4
HD 102870	F8V	4.00	4.0	11 50 39.20 +01 46 07.0		1
HD 105211	F0IV	4.20	50.0	12 06 52.60 −64 36 47.0		2
HD 119756	F2IV	4.23	65.0	13 45 43.00 −33 02 30.0		2
HD 125451	F3IV	5.40	39.0	14 19 15.80 +13 00 17.0		4
HD 126053	G2V	6.30	1.0	14 23 14.46 +01 14 53.8		1
HD 136905	K1III	7.40	35.0	15 23 25.90 −06 36 31.0		3
HD 141004	G0V	4.43	2.4	15 46 27.30 +07 21 15.0		1
HD 146233	G2V	5.50	2.4	16 15 36.38 −08 21 45.3		1
HD 147449	F0V	4.80	70.0	16 22 04.78 +01 01 42.1		4
HD 154417	F8.5IV/V	6.01	5.5	17 05 11.82 +00 42 25.7	variable	1,4
HD 165141	G8III+wd	6.80	16.0	18 07 00.12 −48 14 48.7	SB1	3
HD 174429	K5V+Ps	7.80	70.0	18 53 05.64 −50 10 45.1	single	3
HD 182640	F0IV	3.40	80.0	19 25 28.95 +03 06 49.0	variable	2
HD 182776	K2/3III	8.20	12.0	19 28 05.32 −40 50 03.9	SB1	3
HD 185510	K0III/IV	8.00	17.0	19 39 38.62 −06 03 48.0	SB1	3
HD 190540	K0III	8.30	19.0	20 06 02.60 −18 42 16.2	SB1	3
HD 204121	F3V	6.13	18.5	21 26 27.60 +01 06 20.0		4
HD 205249	K1III	7.90	9.0	21 34 16.42 −13 29 01.9	SB1	3
HD 208450	F0IV	4.40	110.0	21 57 54.71 −54 59 33.6	double/multiple	2
HD 212697		6.57	7.5	22 26 33.20 −16 44 29.0		3

Table D.4: The $v \sin i$ standards used for the southern sample. The standards were taken from 1: Soderblom (1982), 2: Sletteback et al. (1975), 3: Randich et al. (1993), 4: Soderblom et al. (1989)

Name	Spectr. type	V	$v_{\rm rad}$	Coordinates (2000.0)
HD 5294	G5	7.38	-8.56	00 54 59.8 +24 06 10
HD 6582	G5Vb	5.12	-98.74	01 07 56.1 +54 56 35
HD 12235	G2IV	5.90	-18.47	02 00 08.3 +03 06 02
HD 19373	G0V	4.05	49.51	03 08 57.4 +49 36 52
HD 22879	F9V	6.74	120.31	03 40 19.7 −03 12 51

Table D.5: The radial velocity standards used for the northern sample.The standards were taken from Duquennoy and Mayor (1991).

Name	Spectr. type	V	$v \sin i$	Coordinates (2000.0)	Source
HD 17094	F0IV	4.20	40.0	02 44 55.5 +10 06 52	2
HD 25680	G5V	5.90	3.0	04 05 19.6 +22 00 38	1
HD 27859	G2V	7.80	8.0	04 24 27.9 +16 53 11	1
HD 30652	F6V	3.19	10.0	04 49 48.8 +06 57 40	2
HD 31738	G5	7.10	30.0	04 58 17.4 +00 27 16	3
HD 32923	G4V	5.01	1.6	05 07 25.1 +18 38 41	1
HD 37824	G5	7.10	13.0	05 41 26.6 +03 46 40	3
HD 39587	G0V	4.41	9.4	05 54 23.5 +20 16 38	1

Table D.6: The $v \sin i$ standards used for the northern sample.The standards were taken from 1: Soderblom (1982), 2: Sletteback et al. (1975), 3: Randich et al. (1993).

Name	Spectr. type	V	Coordinates (2000.0)
HD 2834	A0V	4.77	00 31 24.2 −48 48 14
HD 13709	B9V	5.29	02 12 54.4 −30 43 27
HD 40200	B3V	6.10	05 54 41.2 −49 37 38
HD 160461	A1V	7.47	17 41 30.6 −34 04 25
HD 169398	B5IV	6.30	18 25 54.5 −33 56 43
HD 170770	B5IV	7.76	18 32 15.6 −27 13 16
HD 174996	B3IV	7.20	18 54 22.7 −24 46 08
HD 175544	B2V	7.35	18 55 46.5 +00 15 54
HD 181074	B3	9.00	19 19 00.9 +00 31 07

Table D.7: A- and B-type stars used in the Ca II H & K and He I D$_3$ observations.

E   Northern Sample

Description of the sources in the northern hemisphere sub-sample.

Column 1: ROSAT name.

Column 2: coordinates of the ROSAT X-ray source.

Column 3: the countrate for the X-ray source, in counts per second.

Column 4: the total exposure time for the X-ray source.

Column 5: the hardness ratio 1 of the X-ray source.

Column 6: spectral type, from SIMBAD or from the low-resolution spectra.

Column 7: catalogue name.

Column 8: visual magnitude.

Column 9: Johnson (B/V) index.

Column 10: Separation in R.A. between the X-ray source and the counterpart, in arcsec.

Column 11: Separation in Dec. between the X-ray source and the counterpart, in arcsec.

Table E.1: The northern sample stars.

ROSAT Name RXJ	ROSAT coordinates (2000.0)	Countrate (3)	t_{exp} (4)	HR 1 (5)
0328.2+0409	03 28 14.6 +04 09 48	0.824 ± 0.040	534.3	-0.07 ± 0.05
0330.7+0305	03 30 43.7 +03 05 55	0.082 ± 0.014	542.5	$+0.96 \pm 0.16$
0331.1+0713	03 31 08.3 +07 13 21	0.274 ± 0.030	390.5	-0.26 ± 0.10
0334.8+0624	03 34 50.0 +06 24 45	0.093 ± 0.018	356.1	$+0.77 \pm 0.16$
0336.5+0726	03 36 35.0 +07 26 20	0.087 ± 0.017	382.5	-0.15 ± 0.19
0336.7+0035	03 36 47.2 +00 35 10	14.000 ± 0.185	443.4	-0.08 ± 0.01
0338.7+0136	03 38 44.5 +01 36 57	0.061 ± 0.015	368.2	-0.29 ± 0.20
0338.7+0243	03 38 42.9 +02 43 27	0.048 ± 0.013	385.3	$+0.26 \pm 0.27$
0338.8+0216	03 38 48.7 +02 16 29	0.231 ± 0.026	382.7	-0.10 ± 0.11
0339.9+0314	03 39 59.1 +03 14 12	0.037 ± 0.012	373.3	-0.12 ± 0.34
0341.4−0013	03 41 24.5 −00 13 11	0.160 ± 0.022	392.3	$+0.61 \pm 0.13$
0343.9+0327	03 43 55.7 +03 27 04	0.039 ± 0.012	367.0	-1.11 ± 0.46
0344.4−0123	03 44 25.9 −01 23 28	0.407 ± 0.034	393.8	-0.24 ± 0.08
0344.8+0359	03 44 53.6 +03 59 37	0.047 ± 0.013	378.7	$+0.85 \pm 0.15$
0344.9+0819	03 44 59.0 +08 19 30	0.128 ± 0.022	340.7	$+0.46 \pm 0.17$
0345.0+0237	03 45 03.5 +02 37 14	0.084 ± 0.017	353.4	-0.17 ± 0.19
0347.1−0052	03 47 09.9 −00 52 02	0.032 ± 0.011	371.3	$+0.72 \pm 0.29$
0347.4−0217	03 47 25.7 −02 17 47	0.080 ± 0.017	389.9	$+0.03 \pm 0.20$
0348.5+0831	03 48 32.5 +08 31 33	0.051 ± 0.014	357.0	$+0.84 \pm 0.23$
0348.9+0110	03 48 59.0 +01 10 51	0.090 ± 0.018	344.9	-0.03 ± 0.19
0349.6−0219	03 49 38.3 −02 19 45	0.119 ± 0.021	380.1	-0.05 ± 0.16
0350.2−0131	03 50 15.5 −01 31 14	0.119 ± 0.020	370.1	-0.04 ± 0.16
0350.6+0133	03 50 41.0 +01 33 46	0.073 ± 0.016	359.6	-0.16 ± 0.22
0353.1−0149	03 53 07.5 −01 49 42	0.062 ± 0.016	367.1	$+0.10 \pm 0.24$
0354.2−0257	03 54 17.1 −02 57 20	0.203 ± 0.025	357.0	$+0.13 \pm 0.12$
0354.3+0535	03 54 21.3 +05 35 27	0.042 ± 0.012	362.7	$+0.76 \pm 0.28$
0355.2+0329	03 55 14.8 +03 29 20	0.049 ± 0.014	349.5	-0.06 ± 0.28
0355.3−0143	03 55 20.2 −01 43 44	0.414 ± 0.037	343.3	-0.03 ± 0.09
0356.8−0034	03 56 53.7 −00 34 41	0.044 ± 0.014	330.3	-0.12 ± 0.29
0357.4−0109	03 57 28.7 −01 09 20	0.436 ± 0.037	335.4	-0.35 ± 0.08
0358.1−0121	03 58 10.1 −01 21 36	0.041 ± 0.013	331.9	$+0.04 \pm 0.36$
0358.9−0017	03 58 55.1 −00 17 53	0.032 ± 0.012	331.8	-0.34 ± 0.33
0400.1+0818	04 00 09.8 +08 18 24	0.347 ± 0.033	334.1	$+0.26 \pm 0.09$

Table E.1 − continued

Spect. type	Catal. Name	m_v	(B/V)	$\Delta\alpha$	$\Delta\delta$	observed			
(6)	(7)	(8)	(9)	(10)	(11)	Li	Ca	He	Ph.
K0	SAO 111210	10.93	+0.77	−3	−2	no	no	no	no
K1		13.49		+6	+4	no	no	no	no
K4e		12.60	+0.89	−2	−4	no	no	no	no
F7	HD 22211	6.49	+0.63	+13	−24	yes	no	yes	no
K0		10.59	+0.75	+9	+1	no	no	no	no
K2	HR 1099	5.71	+0.92	−6	−19	no	no	no	no
K5e		13.82	+1.01	+0	+7	no	no	no	no
A2V	HD 26653	8.00	+0.50	+5	−10	yes	no	yes	no
K4	SAO 111315	8.80	+1.40	+2	−2	yes	yes	no	no
K2		12.48	+0.96	+2	−20	no	no	no	no
K3				+26	+14	no	no	no	no
K1	HD 23261	8.44	+1.05	+26	+21	no	no	no	no
G9	BD-01 524	11.16	+1.04	−2	+3	no	yes	no	no
K1e		12.86	+0.79	+8	+7	no	no	no	no
F6	HD 23376	8.49	+0.68	+2	+18	yes	yes	no	no
F5	HD 23412	6.71	+1.69	+9	−8	yes	no	yes	no
K3		13.15	+0.81	= 20	−17	no	no	no	no
K7e				−14	+36	no	no	no	no
G4		10.90	+0.75	+18	−4	no	no	no	no
K3e		11.23		+5	−8	no	no	no	no
G0V	HD 24031	7.00	+0.70	−9	−4	yes	yes	no	no
F4	HD 24098	8.72	−1.12	−5	+5	yes	no	yes	no
F5	HD 24133	10.86		−14	−5	yes	no	yes	no
F7	HD 24435	8.94	+0.41	−14	+29	no	yes	yes	no
G8III	HR 1212					no	no	no	no
A2V	HR 1211					no	no	no	no
G1		9.80	+0.58	+0	−14	no	no	no	no
K3e		11.60	+0.73	+8	+10	no	no	no	no
G5	HD 24681	11.24	+0.92	−3	−2	no	no	no	no
K4e		12.61	+0.92	+12	+1	no	no	no	no
K5	GJ 157A	8.00	+1.13	−11	+3	yes	yes	no	no
M3e	GJ 157B	12.62	+0.92			no	no	no	no
K4		11.52	+1.11	+0	+8	no	no	no	no
K3		10.95	+0.92	+27	−14	no	no	no	no
G5	BD+07 582	9.90		+4	+7	no	no	no	no
G5	BD+07 582B	9.80				no	no	no	no

Table E.1 – continued

ROSAT Name RXJ	ROSAT coordinates (2000.0)	Countrate (3)	t_{exp} (4)	HR 1 (5)
0402.2−0137	04 02 15.3 −01 37 40	0.034 ± 0.012	323.7	-0.62 ± 0.27
0402.5+0551	04 02 34.5 +05 51 51	0.040 ± 0.012	315.5	$+0.64 \pm 0.28$
0402.6−0016	04 02 36.7 −00 16 05	1.550 ± 0.070	320.8	-0.07 ± 0.05
0403.8+0846	04 03 49.1 +08 46 14	0.074 ± 0.017	314.9	-0.27 ± 0.22
0403.9+0811	04 03 56.7 +08 11 48	0.155 ± 0.024	313.2	-0.24 ± 0.14
0404.1+0249	04 04 09.6 +02 49 44	0.235 ± 0.030	325.6	$+0.26 \pm 0.12$
0404.4+0518	04 04 28.1 +05 18 49	0.046 ± 0.013	315.6	$+5.48 \pm 4.27$
0405.5+0323	04 05 30.1 +03 23 57	0.074 ± 0.017	317.2	$+2.90 \pm 0.95$
0405.6+0341	04 05 40.5 +03 41 52	0.075 ± 0.017	319.0	-0.12 ± 0.23
0406.6+0140	04 06 41.1 +01 40 54	0.101 ± 0.020	321.4	-0.33 ± 0.17
0406.8+0053	04 06 49.6 +00 53 19	0.049 ± 0.015	325.7	-0.25 ± 0.27
0407.1−0206	04 07 09.2 −02 06 20	0.046 ± 0.015	331.8	$+1.00 \pm 0.28$
0412.1+0044	04 12 09.1 +00 44 06	0.108 ± 0.020	325.0	$+0.45 \pm 0.18$
0413.5+0742	04 13 32.3 +07 42 52	0.112 ± 0.024	260.9	-0.60 ± 0.15
0415.0+0724	04 15 02.7 +07 24 51	0.042 ± 0.014	278.4	$+0.69 \pm 0.27$
0415.4+0611	04 15 27.2 +06 11 30	0.499 ± 0.043	274.5	-0.42 ± 0.08
0416.2+0709	04 16 16.9 +07 09 21	0.049 ± 0.015	292.6	-1.15 ± 0.35
0416.5+0247	04 16 35.1 +02 47 16	0.076 ± 0.019	268.3	$+0.94 \pm 0.19$
0638.9+6409	06 38 58.5 +64 09 02	0.032 ± 0.011	360.7	$+0.27 \pm 0.35$
0642.7+6405	06 42 46.3 +64 05 34	0.044 ± 0.013	374.3	$+0.13 \pm 0.28$
0648.5+6639	06 48 35.6 +66 39 06	0.043 ± 0.012	403.9	$+0.44 \pm 0.35$
0701.0+6541	07 01 01.2 +65 41 50	0.052 ± 0.014	371.3	$+0.24 \pm 0.26$
0701.3+6827	07 01 23.4 +68 27 43	0.052 ± 0.013	407.4	$+0.01 \pm 0.25$
0704.0+6214	07 04 05.0 +62 14 40	0.040 ± 0.013	365.4	$+0.23 \pm 0.35$
0707.0+5752	07 07 00.5 +57 52 01	0.076 ± 0.017	373.6	-0.06 ± 0.21
0708.0+5815	07 08 01.2 +58 15 42	0.041 ± 0.013	361.8	-0.27 ± 0.29
0711.9+5730	07 11 56.7 +57 30 07	0.045 ± 0.012	389.5	$+0.18 \pm 0.27$
0714.8+6208	07 14 52.3 +62 08 02	0.046 ± 0.013	348.0	-0.03 ± 0.27
0717.4+6603	07 17 28.8 +66 03 34	0.072 ± 0.014	430.4	-0.11 ± 0.19
0720.6+6139	07 20 39.8 +61 39 47	0.036 ± 0.012	366.7	-0.05 ± 0.32

Table E.1 – continued

Spect. type (7)	Catal. Name (8)	m_v (9)	(B/V) (10)	$\Delta\alpha$ (11)	$\Delta\delta$ (12)	observed			
						Li	Ca	He	Ph.
F6	HD 25414	8.23	+0.75	−26	+13	no	no	no	no
G4		12.57	+0.86	−16	+17	no	no	no	no
F5	HR 1249	5.38	+0.50	+0	+3	yes	no	yes	no
K9e		13.44	+1.14	+0	−6	no	no	no	no
F2V	HR 1254	5.50	+0.33	+5	−2	yes	no	yes	no
F6V	HR 1257	5.36	+0.50	+5	+1	yes	no	yes	no
G7		12.44	+0.84	−5	+6	no	no	no	no
G4e		11.28	+0.90	−2	+5	no	no	no	no
G0	SAO 111600	11.19	+0.38	−3	+5	no	no	no	no
F7	HD 25953	8.86	+0.87	−3	−10	yes	no	yes	no
K8e		12.93	+1.22	−6	−4	no	no	no	no
F5						no	no	no	no
G5						no	no	no	no
G5	HD 26573	6.62				yes	yes	no	no
G0	BD+00 710B					no	no	no	no
F2V	HR 1309	5.29	+0.36	−10	−3	yes	no	yes	no
G0	HD 26861	10.54	+0.83	−6	−2	yes	no	yes	no
G5IV	HR 1321	6.93				yes	yes	no	no
G0	HR 1322	6.30				yes	yes	no	no
G0	HD 26990	9.98		+0	−18	yes	yes	no	no
A5	HD 27039	7.99		−6	−12	yes	no	yes	no
K2	HD 46606	7.90	+1.00	+9	−23	yes	yes	no	no
G5	HD 47373	7.80	+1.10	+1	−13	yes	yes	no	no
G5		10.91		−1	−5	no	no	no	no
K2e		12.25	+1.04	−6	+0	no	no	no	no
F5	HD 51069	8.80	+0.10	−9	−12	no	no	yes	no
K7e		12.85	+1.16	−6	−21	no	no	no	no
K9						no	no	no	no
K7e		12.68	+1.33	−11	−35	no	no	no	no
K7		10.90		−7	−43	no	no	no	no
F5	AG+57 634	8.00				yes	no	yes	no
G5	BD+57 1045B	10.30				no	no	no	no
G0	HD 54943	7.80	+0.70	−12	−12	yes	yes	no	no
K3e		12.09	+1.17	−2	−5	no	no	no	no
F7		10.40	+0.74	−35	+23	no	no	no	no

99

Table E.1 – continued

ROSAT Name RXJ	ROSAT coordinates (2000.0)	Countrate (3)	Exp. time (4)	HR 1 (5)
0721.1+6739	07 21 06.7 +67 39 37	0.069 ± 0.014	430.4	-0.45 ± 0.20
0724.3+5857	07 24 21.3 +58 57 13	0.040 ± 0.013	314.8	$+0.68 \pm 0.30$
0725.9+6840	07 25 56.9 +68 40 44	0.046 ± 0.011	420.5	$+0.49 \pm 0.21$
0731.1+6118	07 31 07.7 +61 18 15	0.043 ± 0.017	204.6	$+0.34 \pm 0.34$
0732.3+6441	07 32 20.9 +64 41 22	0.069 ± 0.016	345.5	$+0.64 \pm 0.30$
0735.1+6540	07 35 08.8 +65 40 31	0.069 ± 0.016	345.5	-0.03 ± 0.23
0741.3+6241	07 41 19.6 +62 41 59	0.038 ± 0.014	254.6	-0.71 ± 0.33
0742.8+6109	07 42 49.8 +61 09 24	0.436 ± 0.034	384.3	$+0.63 \pm 0.06$
0752.5+5732	07 52 30.3 +57 32 11	0.044 ± 0.012	422.9	$+0.37 \pm 0.25$
0752.8+6304	07 52 48.3 +63 04 54	0.038 ± 0.011	443.4	-0.03 ± 0.29
0755.1+5819	07 55 11.5 +58 19 22	0.047 ± 0.013	416.6	-0.06 ± 0.26
0755.8+6509	07 55 52.4 +65 09 04	0.055 ± 0.013	485.5	$+1.33 \pm 0.21$
0759.2+5722	07 59 15.2 +57 22 44	0.061 ± 0.014	495.2	$+0.06 \pm 0.23$
0801.3+5902	08 01 20.9 +59 02 53	0.102 ± 0.018	442.3	$+0.23 \pm 0.17$
0801.4+6845	08 01 27.8 +68 45 35	0.043 ± 0.012	375.0	$+0.20 \pm 0.27$
0802.5+5716	08 02 35.0 +57 16 29	1.330 ± 0.055	447.6	$+0.03 \pm 0.04$
0803.2+6141	08 03 17.9 +61 41 06	0.048 ± 0.013	406.8	$+0.03 \pm 0.25$
0809.2+6639	08 09 17.0 +66 39 13	0.049 ± 0.012	414.8	$+0.54 \pm 0.23$
0811.9+5730	08 11 54.5 +57 30 56	0.040 ± 0.012	434.2	$+0.32 \pm 0.30$
0814.5+6256	08 14 35.9 +62 56 05	0.046 ± 0.012	441.4	-0.26 ± 0.23
0818.3+5923	08 18 18.6 +59 23 03	0.031 ± 0.010	406.5	$+0.90 \pm 0.19$
0818.8+6029	08 18 53.0 +60 29 49	0.040 ± 0.012	404.7	-0.38 ± 0.26
0819.1+6842	08 19 09.6 +68 42 18	0.048 ± 0.012	437.3	-0.28 ± 0.22
0819.3+6230	08 19 18.9 +62 30 35	0.038 ± 0.012	422.0	-0.40 ± 0.25
0820.4+5744	08 20 25.7 +57 44 44	0.110 ± 0.019	413.3	-0.21 ± 0.16
0821.0+6526	08 21 04.9 +65 26 33	0.077 ± 0.016	423.9	-0.26 ± 0.18
0823.2+6127	08 23 15.0 +61 27 46	0.197 ± 0.025	405.6	$+0.07 \pm 0.12$
0824.5+6453	08 24 32.3 +64 53 28	0.295 ± 0.027	436.2	-0.11 ± 0.09
0825.2+6442	08 25 17.5 +64 42 26	0.036 ± 0.011	433.9	-0.82 ± 0.20
0826.5+6835	08 26 33.9 +68 35 49	0.036 ± 0.011	433.7	-0.27 ± 0.27
0827.5+5735	08 27 34.3 +57 35 02	0.032 ± 0.010	450.2	-0.35 ± 0.28
0830.2+6043	08 30 15.8 +60 43 00	0.093 ± 0.017	426.1	-0.38 ± 0.16

Table E.1 – continued.

Spect. type (6)	Catal. Name (7)	m_v (8)	(B/V) (9)	$\Delta\alpha$ (10)	$\Delta\delta$ (11)	Li	Ca	He	Ph.
K0	HD 56168	8.50	+0.70	−3	−2	yes	yes	no	no
G8		15.06	+0.63	−18	+9	no	no	no	no
K6		12.21	+0.82	−7	−13	no	no	no	no
K0				−12	+7	no	no	no	no
K9						no	no	no	no
K5e		13.76	+1.07	+28	+25	no	no	no	no
F5	HD 59581	8.60	+0.10	−6	+1	yes	yes	no	no
K7		18.69	+1.02	+15	+23	no	no	no	no
K0	HD 61396	7.90	+1.20	−5	−3	yes	yes	no	no
G1		11.84	+0.60	−5	+2	no	no	no	no
M4						no	no	no	no
F5	HD 63408	8.50	+0.60	−16	−5	yes	no	yes	no
G2		11.69	+0.50	−2	−10	no	no	no	no
G5	BD+65 601	9.90	+1.00	−12	−8	no	no	no	no
G5	2E0755.1+5731	13.48	+0.48	−5	−12	no	no	no	no
F2V	HD 65301	5.70	+0.46	+2	+4	yes	no	yes	no
F8		12.43	+0.92	−4	−4	no	no	no	no
F8V	HD 65626	6.49	+0.62	−7	+1	yes	yes	no	no
F8	SAO 14417	9.10	+0.70	−26	−35	no	no	no	no
G5		8.16	+1.40	−7	−11	no	no	no	no
F8		13.08	+0.67	+1	−5	no	no	no	no
G7	SAO 14468	9.20	+0.70	−27	−8	no	no	no	no
K0e		13.94	+1.01	−15	−6	no	no	no	no
F0	HD 69135	8.50	+0.20	−10	+13	no	no	yes	no
K0e		13.67	+1.02	+3	−22	no	no	no	no
G8III	HD 69148	5.70	+0.90	+11	+9	no	no	no	no
F4V	HD 69548	5.90	+0.38	+0	+9	yes	no	yes	no
G0	HD 69433	8.03	+0.73	+8	+0	no	no	no	no
G5	HD 70050	8.50	+0.60	−8	+9	yes	yes	no	no
K5e	SAO 14532	8.60	+0.60	+37	+1	yes	yes	no	no
F5	HD 70312	7.50	+0.40	+15	−25	no	no	no	no
F5	HD 70399	9.00	−0.20	+28	+0	no	no	yes	no
G1		12.73	+0.69	+27	+27	no	no	no	no
G3	HD 71369	3.40	+0.80	−7	−10	no	no	no	no
	BD+61 1054B	15.20				no	no	no	no

Table E.1 – continued.

ROSAT Name RXJ	ROSAT coordinates (2000.0)	Countrate (3)	t_{exp} (4)	HR 1 (5)
1016.4−0520	10 16 28.7 −05 20 26	3.980 ± 0.108	358.7	−1.00 ± 0.00
1017.5−0808	10 17 31.0 −08 08 58	0.080 ± 0.014	501.7	+0.66 ± 0.18
1018.1+0043	10 18 07.7 +00 43 00	0.051 ± 0.012	447.8	+0.38 ± 0.24
1019.5−0506	10 19 33.4 −05 06 06	0.118 ± 0.018	471.0	+0.21 ± 0.15
1019.5−0513	10 19 34.7 −05 13 44	0.036 ± 0.011	470.7	−0.15 ± 0.27
1020.0−0754	10 20 00.6 −07 54 01	0.052 ± 0.013	452.8	+0.30 ± 0.22
1022.3+0128	10 22 23.4 +01 28 03	0.038 ± 0.013	376.9	+0.41 ± 0.32
1027.0+0048	10 27 03.4 +00 48 39	0.031 ± 0.012	356.1	−0.23 ± 0.34
1027.4−0351	10 27 29.9 −03 51 03	0.065 ± 0.015	395.3	−0.42 ± 0.21
1028.0−0117	10 28 01.7 −01 17 34	0.032 ± 0.010	454.3	+0.84 ± 0.32
1028.6−0127	10 28 38.4 −01 27 45	0.059 ± 0.013	465.1	+0.27 ± 0.24
1029.2−0159	10 29 13.8 −01 59 54	0.043 ± 0.013	448.0	−0.30 ± 0.24
1029.7+0129	10 29 42.1 +01 29 32	0.363 ± 0.032	416.4	−0.12 ± 0.13
1032.6−0653	10 32 39.5 −06 53 25	0.226 ± 0.025	411.4	+0.50 ± 0.10
1036.9−0850	10 36 59.9 −08 50 26	0.135 ± 0.021	431.5	−0.27 ± 0.14
1038.1−0615	10 38 06.8 −06 15 51	0.039 ± 0.012	429.5	+0.81 ± 0.25
1041.3−0144	10 41 23.6 −01 44 26	0.152 ± 0.022	390.0	−0.38 ± 0.13
1047.8−0113	10 47 51.2 −01 13 15	0.168 ± 0.022	433.7	+0.32 ± 0.12
1049.2−0401	10 49 16.3 −04 01 18	0.042 ± 0.012	437.7	−0.16 ± 0.25
1051.2−0553	10 51 12.6 −05 53 21	0.046 ± 0.013	446.2	−0.13 ± 0.26
1051.3−0734	10 51 23.8 −07 34 01	0.048 ± 0.013	436.9	+0.20 ± 0.29
1051.8−0547	10 51 52.2 −05 47 14	0.036 ± 0.011	449.3	−0.05 ± 0.29
1051.8+0235	10 51 53.0 +02 35 34	0.036 ± 0.011	423.8	−1.61 ± 0.40
1055.6+0044	10 55 41.6 +00 44 19	0.058 ± 0.014	434.4	−0.35 ± 0.21
1056.1−0540	10 56 09.2 −05 40 27	0.046 ± 0.013	439.9	−0.41 ± 0.23
1057.1−0101	10 57 06.3 −01 01 11	0.120 ± 0.019	438.9	−0.91 ± 0.08
1059.7−0522	10 59 45.8 −05 22 10	0.068 ± 0.015	445.1	+0.23 ± 0.20
1100.0−0657	11 00 02.7 −06 57 35	0.038 ± 0.011	435.5	+0.56 ± 0.24
1102.5−0634	11 02 31.6 −06 34 27	0.035 ± 0.011	446.7	+0.43 ± 0.28
1103.2−0654	11 03 15.8 −06 54 11	0.039 ± 0.012	438.3	+0.38 ± 0.32
1103.6−0442	11 03 38.5 −04 42 19	0.063 ± 0.014	434.4	−0.34 ± 0.19
1103.8−0741	11 03 51.4 −07 41 51	0.053 ± 0.013	411.9	+0.11 ± 0.25
1105.3−0735	11 05 21.1 −07 35 32	0.067 ± 0.016	406.5	−0.16 ± 0.21

Table E.1 − continued.

Spect. type	Catal. Name	m_v	(B/V)	$\Delta\alpha$	$\Delta\delta$	observed			
(6)	(7)	(8)	(9)	(10)	(11)	Li	Ca	He	Ph.
K9		11.69		+3	+8	no	no	no	no
G8	BD-07 3000	9.40		+3	+8	no	no	no	no
F8	BD+01 2420	9.80	+0.60	−9	+1	no	no	no	no
K0	HD 89490	6.37	+0.90	+8	+12	no	no	no	no
F2	HD 89507	7.60	+0.30	−17	−7	no	no	no	no
K2		10.87		−4	+0	no	no	no	no
F2	HD 89895	8.60	+0.80	−36	−1	no	no	no	no
G0	SAO 118308	9.10	+0.70	−9	+8	no	no	no	no
K7e		12.47		−2	−2	no	no	no	no
K1		11.98	+0.93	−3	+3	no	no	no	no
K3						no	no	no	no
K5e						no	no	no	no
G4						no	no	no	no
K4e	G162-61	11.58	+1.18	+2	+3	no	no	no	no
F5	HD 90905	6.85	+0.45	+0	+4	no	no	no	no
G0	HD 91351	9.60	+0.90	−3	+10	no	no	no	no
F9	HD 91962	7.03	+0.62	−6	−5	no	no	no	no
F7		11.14		−6	−7	no	no	no	no
K1	HR 4182	6.26	+0.88	−15	−3	no	no	no	no
K0	BD-00 2375	9.20	+1.20	−6	+15	no	no	no	no
A2	HR 4229	6.61	+0.22	−16	+10	no	no	no	no
F8	HD 94044	8.80	+0.60	+6	+15	no	no	no	no
K2	PPM 193867	9.50		−5	+2	no	no	no	no
G0	HD 94137	9.10	+0.70	+12	+5	no	no	no	no
K8e		13.93	+1.25	−50	−19	no	no	no	no
F2	HD 94672	5.91	+0.42	−6	+6	no	no	no	no
K7e		12.79		−5	−6	no	no	no	no
K5						no	no	no	no
G3						no	no	no	no
K1		10.21		+3	+1	no	no	no	no
	BD-6 3282	9.40	+0.59	−16	−6	no	no	no	no
K6		15.24		+43	+18	no	no	no	no
		14.55	+0.75	−13	+6	no	no	no	no
G0		15.64		−15	+14	no	no	no	no
K0	HD 95900	7.30	+1.20	+21	−37	no	no	no	no
K5e		11.44		−13	+27	no	no	no	no

Table E.1 − continued.

ROSAT Name RXJ	ROSAT coordinates (2000.0)	Countrate (3)	Exp. time (4)	HR 1 (5)
1201.6+3602	12 01 38.0 +36 02 38	0.039 ± 0.012	484.2	-0.53 ± 0.23
1202.7+3520	12 02 42.7 +35 20 13	0.083 ± 0.016	493.2	-0.29 ± 0.17
1205.2+3336	12 05 12.3 +33 36 58	0.033 ± 0.011	488.4	$+0.02 \pm 0.32$
1208.0+3110	12 08 02.6 +31 10 45	0.067 ± 0.014	501.5	-0.22 ± 0.30
1209.5+3356	12 09 34.8 +33 56 35	0.034 ± 0.010	509.4	$+0.08 \pm 0.28$
1210.6+3732	12 10 38.1 +37 32 43	0.033 ± 0.010	497.3	$+0.53 \pm 0.31$
1220.6+2703	12 20 40.2 +27 03 35	0.041 ± 0.012	491.0	-0.32 ± 0.26
1224.9+3602	12 24 56.2 +36 02 10	0.031 ± 0.010	537.2	-0.11 ± 0.27
1225.9+3346	12 25 56.6 +33 46 46	0.040 ± 0.011	517.2	-0.08 ± 0.27
1619.5+7022	16 19 32.2 +70 22 08	0.085 ± 0.008	1669.9	-0.22 ± 0.09
1620.8+7014	16 20 49.1 +70 14 60	0.025 ± 0.005	1720.2	$+0.46 \pm 0.18$
1625.3+7455	16 25 21.2 +75 55 43	0.010 ± 0.004	1358.9	$+4.39 \pm 5.09$
1625.5+7123	16 25 30.3 +71 23 06	0.171 ± 0.011	1728.5	-0.23 ± 0.09
1627.8+7042	16 27 48.0 +70 42 12	0.017 ± 0.004	1740.7	-0.03 ± 0.25
1627.8+7258	16 27 51.4 +72 58 16	0.010 ± 0.003	1868.8	$+0.21 \pm 0.32$
1628.4+7401	16 28 24.1 +74 01 01	0.063 ± 0.007	1633.6	$+0.09 \pm 0.11$
1629.0+7318	16 29 00.0 +73 18 25	0.019 ± 0.004	1895.6	$+0.15 \pm 0.21$
1636.6+6947	16 36 41.3 +69 47 47	0.042 ± 0.005	2142.4	$+0.29 \pm 0.12$
1637.6+6919	16 37 41.3 +69 19 09	0.014 ± 0.003	2430.1	-0.44 ± 0.38
1637.8+7239	16 37 48.2 +72 39 30	0.031 ± 0.005	2001.1	$+0.10 \pm 0.15$
1648.0+7157	16 48 04.4 +71 57 52	0.011 ± 0.003	2189.6	$+0.33 \pm 0.28$
1653.2+7015	16 53 15.7 +70 15 58	0.086 ± 0.007	2284.9	$+0.42 \pm 0.08$
1653.5+7344	16 53 34.2 +73 44 17	0.068 ± 0.008	1611.6	$+0.05 \pm 0.11$
1656.4+7407	16 56 24.7 +74 07 05	0.014 ± 0.004	1573.5	$+0.49 \pm 0.31$
1705.4+7436	17 05 25.2 +74 36 03	0.053 ± 0.007	1685.4	$+0.33 \pm 0.13$
1706.3+7329	17 06 22.9 +73 29 31	0.070 ± 0.008	1756.7	-0.10 ± 0.10
1709.4+7056	17 09 26.3 +70 56 27	0.012 ± 0.003	2703.9	$+0.09 \pm 0.22$
1711.2+6930	17 11 16.5 +69 30 13	0.030 ± 0.004	3084.9	$+0.54 \pm 0.14$
1712.5+7107	17 12 35.0 +71 07 34	0.019 ± 0.004	2694.6	$+0.04 \pm 0.18$
1716.1+7147	17 16 11.6 +71 47 39	0.103 ± 0.007	2390.2	$+0.31 \pm 0.07$
1721.1+6947	17 21 11.1 +69 47 58	0.012 ± 0.002	3463.4	$+0.00 \pm 0.20$
1722.6+7316	17 22 40.7 +73 16 39	0.035 ± 0.005	2189.8	-0.11 ± 0.12
1723.3+7347	17 23 18.2 +73 47 46	0.012 ± 0.003	2165.3	$+0.75 \pm 0.34$
1724.0+6940	17 24 00.5 +69 40 23	0.048 ± 0.004	3655.6	$+0.43 \pm 0.09$
1724.0+7354	17 24 05.6 +73 54 44	0.013 ± 0.003	2168.3	$+0.34 \pm 0.23$

Table E.1 − continued.

Spect. type	Catal. Name	m_v	(B/V)	$\Delta\alpha$	$\Delta\delta$	observed			
(6)	(7)	(8)	(9)	(10)	(11)	Li	Ca	He	Ph.
G2				−22	+0	no	no	no	no
K7		13.80	+0.94	−20	+2	no	no	no	no
G4		14.44	+0.65	−11	+23	no	no	no	no
K4		11.24	+1.01	+3	−19	no	no	no	no
F2		12.69	+0.62	+8	−4	no	no	no	no
K0		13.35	+0.64	+7	+3	no	no	no	no
F3	HR 4698	7.13	+0.36	−15	+12	no	no	no	no
K0		13.74	+0.44	+15	−10	no	no	no	no
G0						no	no	no	no
M2e						no	no	no	no
F8	HD 8004	7.40	+1.00	+0	+2	no	no	no	no
K1e		11.80	+0.92	+3	+8	no	no	no	no
F8	SAO 8518	9.60	+0.80	−9	+4	no	no	no	no
F8	HD 148941	7.10	+1.20	+6	−2	no	no	no	no
G1						no	no	no	no
K7e		12.15	+1.20	+9	+0	no	no	no	no
K0	SAO 8533	9.20	+1.30	+10	+8	no	no	no	no
F7		7.95	+0.87	+7	−8	no	no	no	no
F5	HD 150631			+12	+12	no	no	no	no
K3	SAO 17172			+32	−8	no	no	no	no
K0		10.47	+1.11	+9	−11	no	no	no	no
F8	HD 152628	9.11		+18	−9	no	no	no	no
K1		10.07	+0.88	+7	−1	no	no	no	no
K0	SAO 8653	8.44	+0.91	−10	+1	no	no	no	no
K3e		17.34	+0.98	−10	−16	no	no	no	no
K0		9.43	+0.85	+4	−5	no	no	no	no
K7		9.94	+1.70	−9	−4	no	no	no	no
K0		10.86	+0.86	+17	−3	no	no	no	no
F8	SAO 17386	9.20	+0.70	−2	+3	no	no	no	no
F2	SAO 8737	9.50	+0.50	−3	−4	no	no	no	no
K2	HD 15370	7.61	+1.20	−6	+7	no	no	no	no
F8	HD 158063	7.40	+0.90	+4	−5	no	no	no	no
K1e		11.57	+0.89	+1	+9	no	no	no	no
K1		12.69	+0.96	+7	+3	no	no	no	no
G4		10.62	+0.69	+1	−7	no	no	no	no
K1		11.11	+1.21	−3	+7	no	no	no	no

Table E.1 – continued.

ROSAT Name RXJ	ROSAT coordinates (2000.0)	Countrate (3)	Exp. time (4)	HR 1 (5)
1726.7+6937	17 26 47.0 +69 37 40	0.012 ± 0.002	3805.5	+1.19 ± 0.29
1728.1+7239	17 28 11.5 +72 39 27	0.066 ± 0.006	2424.6	+0.32 ± 0.09
1730.3+6955	17 30 20.4 +69 55 20	0.039 ± 0.004	3735.7	+0.25 ± 0.10
1732.6+7413	17 32 41.4 +74 13 46	1.240 ± 0.023	2472.3	+0.13 ± 0.02
1734.6+7300	17 34 41.6 +73 00 28	0.013 ± 0.003	2756.1	+0.71 ± 0.26
1736.9+7420	17 36 54.1 +74 20 47	0.029 ± 0.004	2653.8	−0.25 ± 0.13
2152.0+1436	21 52 04.9 +14 36 20	0.036 ± 0.012	329.7	+0.74 ± 0.26
2154.7+1433	21 54 44.3 +14 33 28	0.095 ± 0.019	320.8	+0.75 ± 0.15
2156.4+0516	21 56 27.0 +05 16 01	0.375 ± 0.036	340.3	−0.08 ± 0.09
2159.9+0302	21 59 59.1 +03 02 32	0.147 ± 0.023	331.2	+0.74 ± 0.12
2202.3+0353	22 02 20.8 +03 53 06	0.105 ± 0.021	310.7	−0.38 ± 0.18
2204.9+0749	22 04 58.9 +04 49 43	0.081 ± 0.018	306.0	+0.65 ± 0.20
2206.1+1005	22 06 10.8 +10 05 14	0.208 ± 0.034	225.3	+0.19 ± 0.15
2209.7+1032	22 09 45.3 +10 32 00	0.043 ± 0.014	296.1	+0.59 ± 0.27
2212.2+1329	22 12 13.8 +13 29 14	0.051 ± 0.016	294.7	−0.22 ± 0.27
2214.1+0546	22 14 06.1 +05 46 23	0.061 ± 0.020	203.5	−1.45 ± 0.47
2214.1+0810	22 14 10.8 +08 10 18	0.063 ± 0.016	310.2	+0.56 ± 0.21
2217.4+0606	22 17 27.5 +06 06 03	0.034 ± 0.012	303.9	+1.04 ± 0.27
2217.4+1037	22 17 28.3 +10 37 28	0.033 ± 0.012	273.3	−1.63 ± 0.98
2224.4+0821	22 24 28.4 +08 21 45	0.036 ± 0.014	251.6	+0.27 ± 0.40
2225.2+0826	22 25 13.3 +08 26 13	0.038 ± 0.015	243.3	+0.40 ± 0.43
2226.3+0351	22 26 18.2 +03 51 44	0.101 ± 0.020	270.6	+1.92 ± 0.36
2228.6+0305	22 28 36.7 +03 05 08	0.031 ± 0.012	241.2	+0.70 ± 0.29
2232.9+1040	22 32 57.8 +10 40 35	0.046 ± 0.013	422.1	−0.15 ± 0.24
2233.6+0506	22 33 40.0 +05 06 22	0.037 ± 0.014	248.5	+2.67 ± .98
2233.7+1230	22 33 44.4 +12 30 16	0.041 ± 0.012	447.7	+0.82 ± 0.29
2236.2+0601	22 36 16.5 +06 01 06	0.038 ± 0.012	380.0	+0.52 ± 0.29
2237.0+0416	22 37 02.4 +04 16 54	0.053 ± 0.016	294.5	+0.98 ± 0.36
2239.3+0325	22 39 18.1 +03 25 21	0.054 ± 0.016	297.5	+0.33 ± 0.31
2240.7+1326	22 40 46.2 +13 26 12	0.097 ± 0.016	430.3	+0.71 ± 0.15
2240.8+1433	22 40 52.3 +14 33 07	0.039 ± 0.011	445.0	−0.72 ± 0.21
2241.9+1431	22 41 58.2 +14 31 04	0.083 ± 0.015	439.4	+0.10 ± 0.18
2242.0+0946	22 42 01.1 +09 46 00	0.098 ± 0.017	416.0	−0.18 ± 0.17

106

Table E.1 – continued.

Spect. type	Catal. Name	m_v	(B/V)	$\Delta\alpha$	$\Delta\delta$	observed			
(6)	(7)	(8)	(9)	(10)	(11)	Li	Ca	He	Ph.
F5		9.27	+0.65	+8	−13	no	no	no	no
K4e		11.50		−5	+6	no	no	no	no
F0		8.77	+1.16	+3	−7	no	no	no	no
K0	HD 160538	6.55	+1.05	+4	+9	no	no	no	no
F0		9.03	+0.72	−22	−23	no	no	no	no
K0		7.75	+0.96	−2	+24	no	no	no	no
K0	HD 207902	8.20	+1.20	+44	+9	no	no	no	no
F5	SAO 107496	9.05		+13	−1	no	no	no	no
K2		11.05	+0.94	−3	+5	no	no	no	no
G8	SAO 127215	9.70	+0.90	−10	+7	no	no	no	no
K7e		14.30	+1.05	+10	−2	no	no	no	no
K5e		13.45	+1.01	−21	−4	no	no	no	no
G8	SAO 127298	10.00	+0.10	−15	−16	no	no	no	no
G8		11.10	+0.80	+13	+8	no	no	no	no
G5	HD 210750	8.70	+0.66	+7	−7	no	no	no	no
F8	HD 210985	8.20	+0.20	+51	−10	no	no	no	no
G0		14.99	+0.81	+19	−20	no	no	no	no
K1e		13.52	+0.80	−8	−2	no	no	no	no
G5		13.77	+0.74	+25	+27	no	no	no	no
K5		13.69	+1.02	−13	+15	no	no	no	no
G3						no	no	no	no
K1		10.58	+0.81	−5	−4	no	no	no	no
G5		10.89		+8	+3	no	no	no	no
K2		11.89	+1.03	+8	−18	no	no	no	no
K2		11.10	+0.99	−37	+0	no	no	no	no
F8		10.01	+0.80	+11	+2	no	no	no	no
M1		16.90		−19	+18	no	no	no	no
K2e		13.30		−9	+2	no	no	no	no
G8		10.70	+0.76	+16	+14	no	no	no	no
K8		17.15	+1.38	+17	+30	no	no	no	no
F9		12.87	+0.46	+11	+8	no	no	no	no
G8		13.80	+0.60	−4	+0	no	no	no	no
G4	HD 214850	5.71	+0.72	+9	+17	no	no	no	no
K0	HD 214995	5.90	+1.11	+18	+4	no	no	no	no
K8e		12.56	+1.38	−7	−9	no	no	no	no

Aknowldegements

I would like now to thank all the persons that have helped me realize this thesis work.